

OPEN OCEAN POLYNYAS AND ANTARCTIC SLOPE CURRENT IN HIGH-
RESOLUTION EARTH SYSTEM MODEL SIMULATIONS

A Dissertation

by

XILIANG DIAO

Submitted to the Office of Graduate and Professional Studies of
Texas A&M University
in partial fulfillment of the requirements for the degree of

DOCTOR OF PHILOSOPHY

Chair of Committee,	Achim Stössel
Committee Members,	Ping Chang
	Alejandro Orsi
	Robert Korty
	Xueen Chen
Head of Department,	Shari Yvon Lewis

August 2022

Major Subject: Oceanography

Copyright 2022 Xiliang Diao

ABSTRACT

The first part of my dissertation focusses on the intermittent occurrence of Open Ocean Polynyas (OOPs) in a 500-year-long High-Resolution Pre-Industrial (HR-PI) Community Earth System Model 1.3 simulation (Chapter 3). During the winter season, the near-surface salinity stratification is found to be a key condition for the intermittent occurrence of the OOPs. Increased/decreased stratification, resulting from strong/weak freshwater fluxes at the surface will hamper/favor the formation of polynyas. The surface freshwater flux varies with a regional Southern Annular Mode (SAM)-like index (measured over a longitudinal section instead of circumpolar) and the associated meridional shift of the precipitation-rich westerly winds. Based on this HR-PI simulation, I detected a new possible regional ocean-atmosphere coupled mechanism that explains both the intermittent occurrence of OOPs and the simultaneous change of the regional SAM index. When large Weddell Sea Polynya (WSP) emerge, they affect the regional atmospheric sea-level pressure, thereby feeding back onto the regional SAM index. The initiation of polynya events is controlled by changes in surface properties while the location of initiation is determined by bathymetric features.

The second part of my dissertation deals with the anthropogenic impact on the formation of WSPs and open ocean deep convection in an accompanying 250-year HR historical and future Transient (HR-TN) simulation (Chapter 4). In HR-PI, the (regional) SAM index does not have a clear trend, and only oscillates around its mean value. This provides a suitable environment for studying the intermittent occurrence of OOPs. In HR-TN, the anthropogenic impact forces the (regional) SAM index to become more

positive. The associated poleward movement of the precipitation-rich Southern Hemisphere westerlies brings more freshwater and heat to the Weddell Sea region. At the same time, less sea ice forms due to the higher air temperature. These changes increase the stratification in the Weddell Sea, which in turn suppresses open ocean deep convection and the return of WSPs. However, shallow convection continues to occur intermittently over and around the Maud Rise seamount, even though this region turns ice-free in winter. Another noticeable feature is that the zonal asymmetry of the poleward movement of the westerlies leads to a drastic reduction of the winter ice cover in the Weddell Sea, but not in the Ross Sea. Corresponding Low-Resolution (LR) simulations do not produce any OOPs, and the anthropogenic forcing leads to an overall reduction of ice extent, but not to quasi-ice-free winters in the Weddell Sea as in HR-TN.

For the third part of my dissertation, I investigated the anthropogenic impact on the Antarctic Slope Current (ASC) and the Dense Shelf Water (DSW) overflow in both HR and LR simulations (Chapter 5). In HR-PI and LR-PI, the generation of AABW from DSW overflow is partly captured on both the continental shelf and slope of the Ross Sea and the Weddell Sea. However, due to excessive convective entrainment, the bottom water potential density in the Ross Sea is lower than in observations in both HR-PI and LR-PI. Due to HR-PI regularly simulating open-ocean deep convection in the Weddell Sea, the bottom water potential density there matches better with the observations than in LR-PI. In HR-TN and LR-TN, the generation of AABW from DSW overflow ceases as the shelf water becomes more buoyant. The latter is mostly attributed

to a reduction of sea ice formation along the coast. ASC confines most freshwater input tightly along the Antarctic coast and increases the sea surface height (SSH) there. This, in turn, leads to an increased meridional SSH gradient, which then feeds back to further strengthen the ASC. This positive feedback isolates the Antarctic shelf waters, and eventually turns the three present-day characteristic shelf water regimes all into “Fresh Shelf” regimes.

DEDICATION

To my parents, thanks for their unwavering support.

ACKNOWLEDGEMENTS

I would like to start by thanking my advisor Dr. Achim Stössel for his continuous support of my PhD study. I am grateful to have an advisor who are always patient, and always challenging and encouraging me to think some new scientific questions independently, in hundreds of research meeting discussions. I am also very appreciating it for your helping in my academic writing and academic presentations through many rounds of feedbacks. Also thank you for always encouraging me to attend many academic conferences, discuss with many experts in this field, and figure out my future path.

I would also like to thank my unofficial co-advisor Dr. Ping Chang for playing a pivotal role in my academic, too. Your kindness I will always remember. And thanks for your always insightful and enlightening questions, which bring many new understanding and new ideas to me.

I would like to thank my committee members Dr. Alejandro Orsi, Dr. Robert Korty, and Dr. Xueen Chen for their very inspiring courses, guidance, and comments throughout my PhD study. I also would like to thank many of my co-workers: Dr. Gokhan Danabasoglu and Dr. Stephen G. Yeager from NCAR for their incredible feedbacks on my manuscripts; Dr. Shaoqing Zhang, Dr. Hong Wang, and Dr. Abishek Gopal for their hard working on running the simulations and managing the datasets; also, thanks for Dr. Prajvala Kurtakoti and Dr. Sanjiv Ramachanderan for many suggestions and help at the initial stage of this research.

CONTRIBUTORS AND FUNDING SOURCES

I would also like to thank the Department of Oceanography at Texas A&M University for supporting my graduate study through many Scholarships. I would also like to acknowledge the finance support from China Scholarship Council (CSC) and international Laboratory for High Resolution Earth System Prediction (iHESP).

NOMENCLATURE

AABW	Antarctic Bottom Water
ACC	Antarctic Circumpolar Current
ARP	Astrid Ridge Polynyas
ASC	Antarctic Slope Current
CAM5	Community Atmosphere Model version 5
CDW	Circumpolar Deep Water
CESM1.1	Community Earth System Model version 1.1
CESM1.3	Community Earth System Model version 1.3
CICE4	Community Ice Code version 4
CLM4	Community Land Model version 4
CMIP5	Coupled Model Intercomparison Project 5
ESM	Earth System Model
HR	High Resolution
HR-PI	High-Resolution Preindustrial Control Simulation
HR-TN	High-Resolution Historical and Future Transient Simulation
LR	Low Resolution
LR-PI	Low-Resolution Preindustrial Control Simulation
LR-TN	Low-Resolution Historical and Future Transient Simulation
MOC	Meridional Overturning Circulation
MRP	Maud Rise Polynya
OOP	Open Ocean Polynya

POP2	Parallel Ocean Program version 2
SAM	Southern Annular Mode
WDW	Weddell Deep Water
WSP	Weddell Sea Polynya

TABLE OF CONTENTS

	Page
ABSTRACT	II
DEDICATION	V
ACKNOWLEDGEMENTS	VI
CONTRIBUTORS AND FUNDING SOURCES.....	VII
NOMENCLATURE.....	VIII
TABLE OF CONTENTS	X
LIST OF FIGURES.....	XII
LIST OF TABLES	XVIII
CHAPTER I INTRODUCTION	1
1.1. The Southern Ocean's role in the global earth system.....	1
1.2. Overview of polynyas and the associated deep convection	4
1.3. Overview of Antarctic Slope Current.....	9
1.4. Research motivation and questions	12
CHAPTER II MODEL CONFIGURATIONS AND SIMULATIONS	14
2.1. Community Earth System Model version 1.3	14
2.2. High-Resolution Preindustrial Control Simulation (HR-PI).....	15
2.3. High-Resolution Transient Climate Simulation (HR-TN)	16
2.4 Corresponding Low-Resolution (LR) Simulations	16
2.5 The advantages and disadvantages of the described simulations.....	17
CHAPTER III THE INTEMITTENT OCCURRENCE OF OPEN-OCEAN POLYNYAS IN HR-PI.....	21
3.1. Background information	21
3.2. Data and methodology	27
3.3. Variability of Polynya Occurrence and Its Relation to Upper-Ocean Salinity	29
3.4. Transition from no-polynya to polynya phase	36
3.5. Variables correlating with polynyas and possible polynya feedbacks.....	39
3.6. The role of topographic preconditioning the polynya formation	52
3.7. On the role of the deep heat reservoir	56
3.8. Summary and conclusions.....	60

CHAPTER IV ANTHROPOGENIC IMPACT ON WEDDELL SEA POLYNYA AND OPEN OCEAN DEEP CONVECTION IN HR-TN.....	64
4.1 Background information	64
4.2 Impact of anthropogenic forcing on polynya occurrence.....	67
4.3 Impact of anthropogenic forcing on ocean salinity and temperature	69
4.4 Impact of anthropogenic forcing on upper-ocean temperature and salinity.....	73
4.5 Changes of SAM index due to anthropogenic forcing	77
4.6 Trends of ice concentration, air temperature, and precipitation.....	85
4.7 Summary and conclusions.....	92
CHAPTER V ANTHROPOGENIC IMPACT ON ANTARCTIC SLOPE CURRENT AND DENSE SHELF WATER OVERFLOW.....	95
5.1 Background information	95
5.2 Bottom topography and potential vorticity conservation.....	97
5.3 Anthropogenic forcing influence on DSW overflow in HR and LR.....	99
5.4 Change of characteristic property regimes.....	113
5.4.1. Dense Shelf regime	114
5.4.2. Fresh Shelf regime.....	120
5.4.3. Warm Shelf regime	122
5.5 Reasons for the salinity decrease on the Antarctic shelves	127
5.6 Summary and conclusion	131
CHAPTER VI CONCLUSIONS AND FUTURE WORKS.....	135
6.1 Conclusions	135
6.2 Future works.....	137
REFERENCES.....	140

LIST OF FIGURES

	Page
Figure 3.1. (a) Simulated September sea-ice concentration showing different polynya types in the Weddell Sea. (a) Maud Rise Polynya (MRP). (b) Astrid Ridge Polynya. (c) Weddell Sea Polynya (WSP). The Prime Meridian (black line) has been used to distinguish MRPs from WSPs.....	23
Figure 3.2. Bathymetry of the Weddell Sea below 2,000 m. Selected regions referenced in text: the WSP region (20° – 10° W, between orange lines), the MRP region (0° – 10° E, between green lines), the ARP region (10° – 20° E, between red lines). Yellow box (between 63° – 68° S and 40° W– 20° E) used for analysis of specific variables, for example, Hovmöller diagrams in Figure 3.3.....	28
Figure 3.3. Time-longitude plots of simulated September (a) sea ice concentration, (b) upper-ocean (top 10 m) salinity, and (c) mixed-layer depth averaged between 63° S and 68° S. The three regions bounded by different colors correspond to those in Figure 3.2.	30
Figure 3.4. (a) Time series of sea ice concentration (September) averaged over the respective boxes shown in Fig. 2. (b) Same as (a), but for upper-ocean salinity. The shadings indicate ice concentration less than 70% in the respective box areas defined to be representative of polynya periods.....	33
Figure 3.5. (a) Simulated monthly-mean upper-ocean salinity (top 10m) at the model grid point where the MRP of simulation year 300 is triggered. The dashed blue line represents the critical salinity value for triggering the MRP. The grey shaded area indicates the time of MRP occurrence. (b) Simulated September-mean Sea ice concentration indicating the location of the MRP of simulation year 300.	35
Figure 3.6. Wavelet spectrum of sea ice concentration time series in MRP region. The yellow lines represent the 95% significance contour (Mabel Costa, personal communication., 2021). The shaded area is the cone-of-influence; anything in the shaded area is not trustworthy.	36
Figure 3.7. (a) T-S diagram of monthly-mean upper-ocean properties averaged over the MRP region showing seasonal and interannual changes during the transition from no-polynya to MRP mode in simulation years 292 to 310. The dots denote September properties. (b) Same as (a), but for September data only. See text for a more detailed explanation. The MRP is triggered in year 300.	38

Figure 3.8. (a) Total precipitation from atmosphere (rain + snow). (b) Total evaporation over both ocean and sea ice cover. Graphics represent September-mean values of model year 270.....	42
Figure 3.9. (a) 5-year running mean timeseries of total precipitation averaged over the black box area in Fig.2. The shading reflects MRP years (light grey), and WSP years (dark grey), matching with Fig. 4. (b) Eight-year- mean total precipitation difference of typical polynya years (years 482-489 mean, between the red lines in (a) when precipitation in chosen polynya period is maximum) minus typical no-polynya years (years 470-477 mean, between the purple lines in (a) when precipitation in chosen no-polynya period is minimum).	43
Figure 3.10. (a) 5-year running mean timeseries of annual net sea-ice growth and melt induced freshwater flux in central Weddell Sea (yellow box). (b) Annual net sea-ice induced freshwater flux in polynya period (year 430-439 mean, between purple lines in (a) when freshwater flux in chosen polynya period is maximum). (c) Same as (b) but in no-polynya period (year 460-469 mean, between red lines in (a) when freshwater flux in chosen no-polynya period is minimum).....	44
Figure 3.11. Timeseries of 5-year running means of (a) Standardized sea-level pressure at 65°S in the region of 40°W-30°E. (b)The Regional Meridional Pressure Difference (RMPD) index, a SAM-like index, but only calculated in the region of 40°W-30°E. (c) Wind stress curl anomaly averaged over the wider Weddell Sea region (40°W-30°E, 70°S-55°S). (d) Net precipitation averaged over black box in Fig.2. (e) Weddell gyre strength (measured as the westward transport across the prime meridian). (f) Upper ocean salinity (top 10m) averaged over black box in Fig.2.....	47
Figure 3.12. Conceptual circuit of sequence of processes involved in our proposed coupled ocean-atmosphere mechanism.	51
Figure 3.13. (a) September temperature at 305 m depth of simulation year 299. (b) Same as (a) but for salinity. (c) Same as (a) but for mixed-layer depth. Black contours indicate depth.....	54
Figure 3.14. (a) September sea ice vorticity field in simulation year 299, black contours indicate depth contours. (b) zonal velocity across section 3°E (the yellow line in (a)).....	55
Figure 3.15. (a) Enlargement of Fig.10c with focus and bathymetry around the Maud Rise seamount and the Astrid Ridge. (b) Year 460-469 mean September sea-ice concentration. Black contours stand for depth. Yellow line represents the section that cross the top of Maud Rise seamount.....	56

Figure 3.16. Time series of depth profiles of (a) temperature, (b) salinity, (c) water age, (d) water density at upper ocean (red) and at 250m (green), and (e) upper-ocean salinity, all averaged over the central Weddell Sea (61.3°S - 70°S, 40°W - 10°W). Grey areas represent the WSP periods	59
Figure 4.1. Timeseries of September sea-ice concentration (a) for model years 250-500 of HR-PI and (b) for years 1850-2100 of HR-TN, both averaged over the region 63°S - 68°S. The black line in (b) represents year 2006, when the climate forcing is changed from historical forcing to the CMIP5 RCP8.5 forcing in HR-TN, while the black dashed line in (a) (simulation year 406) has been added for comparison purposes. The red lines in (b) represent the observed polynya events of years 1974-1976 and 2016-2017. Selected regions referenced in text: the WSP region (30°W - 0°, between yellow lines), the MRP region (0°- 10°E, between green lines).	67
Figure 4.2. (a) Time series of September mixed-layer depth for PI-CTRL simulation. (b) Same as (a) but for HF-TNST simulation. The period ranges from the maroon lines in Fig.1 to the end of each simulation.....	68
Figure 4.3. Timeseries of vertical monthly-mean salinity profiles from (a) HR-PI and (b) HR-TN. All averaged over the WSP region in Figure 4.1.....	71
Figure 4.4. Same as in Figure 4.3, but for temperature.....	72
Figure 4.5. (a) September upper-ocean (upper 10m) salinity of last 250 years of PI-CTRL simulation. (b) Same as (a) but of HF-TNST simulation. Averaged over the region 63°S - 68°S, 40°W-20°E.	73
Figure 4.6. Same as Fig.4.5, but for temperature.....	74
Figure 4.7. Timeseries of September water potential density from (a) HR-PI and (b) HR-TN. The respective dark-green lines represent water density at 250-m depth, while the respective dark-red lines represent the upper-ocean (10 m) density. All values are averaged over the same region as in Figure 3 and Figure 4. The black lines denote year 406/2006 in HR-PI/HR-TN. The potential density is referenced to the surface.....	76
Figure 4.8. (a) Timeseries of simulated (a) Southern Annular Mode (SAM) index and (b) Regional Meridional Pressure Difference (RMPD) index (see text for definition). The grey and purple lines represent HR-PI and HR-TN, respectively. The dashed black lines represent the year when the climate forcing has been changed from historical forcing to the CMIP5 RCP8.5 forcing in HR-TN. Note that color of time axis labels correspond to respective experiments (grey: HR-PI, purple: HR-TN).....	77

Figure 4.9. Climatology of the maximum zonal wind-stress position around Antarctica. Blue and red lines represent the time-mean positions for 1850-1900 and 2050-2100, respectively, from HR-TN.....	79
Figure 4.10. (a) Simulated RMPD index from (a) HR-PI and (b) HR-TN. Orange lines repeat the RMPD index shown in Figure. 4.8b. Red and green lines show the standardized sea-level pressure at 65°S (times minus one) and 40°S, respectively. Red dash line (=0) is mean value in (a), while the black solid line is the linear trend of RMPD in (b), the slope is 0.0072. Otherwise as Figure 4.8.....	81
Figure 4.11. Simulated RMPD index (orange) from (a) LR-PI and (b) LR-TN. Red and green lines are the standardized sea-level pressure at 65°S (with a minus sign) and 40°S, respectively. Red dash line (=0) is mean value in (a), while the black dash line is the linear trend of RMPD in (b), the slope is 0.0073.	82
Figure 4.12. (a) The latitudinal position of the maximum zonal-mean westerly wind stress. (b) The magnitude of the maximum zonal-mean wind stress. Purple and grey lines represent HR-TN and HR-PI, respectively. Zonal mean is over the same longitudinal extent as the RMDP index. The vertical black line is year 2006 (same as in Figure. 4.1), while the lateral red line is the mean value of the HR-PI time series (grey line).	84
Figure 4.13. The latitudinal position of the maximum zonal-mean westerly wind stress. (b) The magnitude of the maximum zonal-mean wind stress. Purple and grey lines represent LR-TN and LR-PI, respectively. Zonal mean is over the same longitudinal extent as the RMDP index. The vertical black line is year 2006 (same as in Figure 4.12), while the lateral red line is the mean value of the LR-PI time series (grey line).....	85
Figure 4.14. (a) Timeseries of annual-mean total precipitation (light blue line). (b) Timeseries of 5-year running mean of monthly near-surface air temperature (dark blue line). The maroon lines in both (a) and (b) show the timeseries of September (inverted) ice concentration. All timeseries are from HR-TN and averaged over 63°S - 68°S, 40°W-20°E. The vertical black line is year 2006 (same as in Figure 4.1).....	86
Figure 4.15. Spatial distribution of the total precipitation difference between the last decade (2090-2100) and the first decade (1850-1860) of HR-TN.	87
Figure 4.16. September sea ice concentration around Antarctica averaged over the first 10 years and the last 10 years of HR-TN.	90

Figure 4.17. September sea ice concentration around Antarctica averaged over (a) for the first 10 years and (b) for the last 10 years of LR-TN. Red box (between 63°S - 68°S and 40°W - 20°E) used for analysis of specific variables.	91
Figure 5.1. Model bathymetry around Antarctica, (a) high-resolution (HR), (b) low-resolution (LR).....	98
Figure 5.2. September mixed-layer depth over the Antarctic continental shelf. (a) Year 450-500 of HR-PI, (b) year 2050-2100 of HR-TN. (c) Year 450-500 of LR-PI, (d) year 2050-2100 of LR-TN. The characteristic Dense Shelf regime is normally found across the shelf break within the purple boxes, while that of the Warm Shelf regime within the red box. The shelf regions outside the boxes are mostly Fresh Shelf regimes.....	101
Figure 5.3. September sea ice thickness (with thin ice along the coast indicating coastal polynyas). Otherwise as Fig.5.2.	102
Figure 5.4. The September meridional components of wind stress, positive northward. Otherwise as Fig.5.2.	103
Figure 5.5. Annual thermodynamic ice growth (only showing values > 5 mm/day). Otherwise as Fig.5.2.	104
Figure 5.6. September-mean salinity of the bottom ocean model layer. Otherwise as Fig.5.2.	106
Figure 5.7. September potential temperature of deepest ocean model layer. Otherwise as Fig.5.2.....	108
Figure 5.8. September potential density of deepest ocean model layer (calculated from potential temperature and salinity). Otherwise as Fig.5.2. The two yellow lines mark the sections being shown in Fig 5.11 and Fig.5.12.....	110
Figure 5.9. September water age of deepest ocean model layer. (a) Year 450-500 of HR-PI, (b) year 450-500 of LR-PI.....	111
Figure 5.10. Timeseries of September-mean water-column average salinity of HR-PI (black) and HR-TN (red), averaged over (a) the Weddell Sea shelf region, (b) the Ross Sea shelf region.	112
Figure 5.11. September potential temperature (upper panels), salinity (lower panels), and potential density (yellow contour lines) in the Ross Sea Dense Shelf section (172°E). Otherwise as Fig.5.2.	117
Figure 5.12. Weddell Sea Dense Shelf section (67.5°S). Otherwise as Fig.5.11.....	119

Figure 5.13. Fresh Shelf section (15°W). Otherwise as Fig. 5.11.....	121
Figure 5.14. Warm Shelf section (88°W). Otherwise as Fig.5.11.....	123
Figure 5.15. September sea-surface height (SSH). Otherwise as Fig.5.2.	125
Figure 5.16. September zonal speed of Antarctic Slope Current. Otherwise as Fig.5.2.	126
Figure 5.17. September zonal velocity vertical section along 113.3°E. (a) Year 450- 500 of HR-PI, (b) year 2050-2100 of HR-TN.	127
Figure 5.18. Annual thermodynamic ice production difference between (a) HR-TN and HR-PI, (b) between LR-TN and LR-PI. (Fig. 5.5 right panel minus left panel). Annual mean meridional wind stress difference between (c) HR-TN and HR-PI, (d) between LR-TN and LR-PI. (Fig. 5.4 right panel minus left panel).	129
Figure 5.19. (a) Annual Antarctic freshwater runoff difference between HR-TN and HR-PI. (b) Annual precipitation difference between HR-TN and HR-PI.	130

LIST OF TABLES

Page

Table 1, Pearson linear coefficients (r) in Fig.11 (after linear detrending).....	48
---	----

CHAPTER I

INTRODUCTION

1.1. The Southern Ocean's role in the global earth system

To understand how planet Earth works, we study it increasingly as a holistic system that includes all the complex coupling effects between the ocean, the atmosphere, the sea ice, and the ice shelf (Turner et al., 2009). The earth system is principally driven by solar radiation; its variation with latitude leads to more heat accumulating annually in the equatorial zones than in the polar regions. The atmosphere and ocean circulations then respond to, or are driven by, the associated meridional temperature gradient (Trenberth and Caron, 2001).

The atmosphere is mainly heat driven from beneath (ocean surface and land surface) in the tropical region. A combination of tropical heating, poleward moving air aloft, and the Coriolis force leads to the development of the Hadley Cell, an atmospheric circulation in which air rises near the equator, creating the tropical belt of low pressure, and descends in the subtropics, forming the subtropical high-pressure belt (Persson et al., 2006). At higher latitudes (60° - 65°), the air ascends again (Turner et al., 2009), creating another low-pressure zone. The pressure gradient at the Earth's surface between the high pressure in the subtropics and the low pressure at 60° - 65° forces air to move eastwards under the influence of the Coriolis force, creating the mid-latitude westerlies. Especially in the Southern Hemisphere, due to the lack of land barriers, the strong westerly winds lead to the strongest ocean current on Earth, the Antarctic Circumpolar Current (ACC, Smith et al., 2013). Here, the meridional gradient of the air pressure at sea level (also

called sea-level pressure or SLP) is subject to remarkable variability in both its intensity and its location (Swart and Fyfe, 2012). The Southern Annular Mode (SAM) index is defined as the difference of the standardized zonal-mean SLP between 40°S and 65°S ($SAM = P_{40}^* - P_{65}^*$, where P^* represents the standardized SLP; Gong and Wang, 1999), and describes the dominant mode of variability over the Southern Ocean and Antarctica (Marshall, 2003). The ascending air at 60°- 65° S moves poleward at upper levels and sinks over the South Pole, thus forming a high-pressure system over the Antarctic continent (Turner et al., 2009). The pressure gradient between the low pressure at 60°- 65°S and the high pressure over the South Pole gives rise to pronounced easterly winds, driving the westward-directed Antarctic Slope Current (ASC, Jacobs 1991; Thompson et al., 2018). In between the predominantly zonal ACC and ASC circulation systems are regional cyclonic gyres, principally the Weddell Gyre and the Ross Gyre (Klatt et al., 2005; McCartney and Donohue, 2007). Finally, the regions with ascending air (tropical and 60°- 65° region) are generally associated with more precipitation, while the regions with descending air are generally low-precipitation areas (subtropics and polar regions; see also Turner et al., 2009).

While the upper ocean is mainly driven by the wind, the deep ocean circulation, also referred to as the global Meridional Overturning Circulation (MOC) is mainly driven by the sea water density differences (Orsi et al., 1999). At a few sites in the polar regions (e.g., Antarctic continental margins, and Labrador Sea), the upper layer waters can become very dense due to strong cooling from the atmosphere and salinification from evaporation or sea-ice formation. This high-density water can sink to the deep or

even bottom ocean, thus contributing to driving the global MOC (Vreugdenhil & Gayen, 2021). Under such circumstances, one can speak of a global thermohaline circulation that is driven by a cold and salty upper ocean in the polar regions.

In numerical simulations, these patterns of the global atmosphere circulation and the global ocean circulation and their interaction can only be represented in global Earth System Models (ESMs).

In this study, one of the main areas that I focus on is the Weddell Sea region. It is therefore necessary to describe in detail the circulation and water masses of the Weddell Sea. The northern boundary of the Weddell Gyre reaches to about 56°S, coinciding with the winter maximum sea-ice extent (Gordon & Huber, 1984). The eastern boundary is located at about 30°E, where due to topographic constraints, a strong mesoscale eddy field is produced between 15°E and 30°E. In the eddies, relatively warm and saline Lower Circumpolar Deep Water (Seabrooke et al., 1971) mixes with the “Weddell cold regime” and forms the “Weddell warm regime” (Schröder and Fahrbach, 1999). These relatively warm waters are advected southward and westward by the large-scale cyclonic Weddell Gyre, and on their way impinge on the Maud Rise seamount (Fahrbach et al., 1994). Observations show that this warm westward return flow transport is about 16 Sv (1 Sv = 10^6 m³/s) along the northern flank of Maud Rise and is about 8 Sv along its southern flank (Schröder and Fahrbach, 1999; Ryan et al., 2016). In winter, there are 4 characteristic layers of water masses in the Weddell Sea. The near-surface winter mixed layer is on average about 100 m thick with a standard deviation of 33 m (Gordon and Huber, 1990). The typical temperature of the winter mixed layer is around the freezing

point at -1.8°C and the typical salinity is about 34.4 psu (Gordon 1998). Just below the relatively thin mixed-layer cap is the Weddell Deep Water or Warm Deep Water (WDW) layer (Fahrbach et al., 2011). The depth of the WDW layer ranges from 200 m to 1500 m. The typical potential temperature is between 0 and 0.8°C, and the typical salinity is between 34.64 and 34.72 psu (Gordon and Huber, 1984, 1990). The WDW layer is the main heat reservoir, and it is sustained by the Weddell Gyre through its westward flowing warm southern branch as described earlier in this paragraph (Fahrbach et al, 1994). In the normal state, a relatively strong salinity-controlled stratification between the top two layers prevents the WDW from rising into the mixed layer (Gordon et al., 2014; Dufour et al., 2017). Occasionally, the salinity-controlled stratification weakens, and the entrainment of the warm WDW into the cold surface mixed layer provides a heat source for open ocean polynya formation. The third layer from above is the Weddell Sea Deep Water (WSDW) with a typical potential temperature between -0.6 and 0°C and salinity between 34.63 and 34.70 psu (Orsi et al., 1993). The bottom layer consists of the Weddell Sea Bottom Water (WSBW) with a typical temperature of lower than -0.6°C (Orsi et al., 1993).

1.2. Overview of polynyas and the associated deep convection

A polynya is an area of open water surrounded by sea ice or surrounded by sea ice and a coastline (Morales Maqueda et al., 2004). There are two main types of polynyas: coastal polynyas and open-ocean polynyas.

Coastal polynyas, which can be found frequently along both the Antarctic and Arctic coasts, are created by strong seaward blowing winds that push newly formed sea

ice away from the coast (Stringer and Groves., 1991; Stössel et al., 2011). They are highly sensitive to the direction and strength of the coastal winds, which in turn is largely determined by local orographic effects; if to be captured in numerical climate model simulations, coastal polynyas are thus highly sensitive to model resolution (Stössel et al., 2011; Zhang et al., 2015). Around Antarctica, the high new-ice production rates within coastal polynyas leads to a large amount of brine rejection, which locally increases the salinity (Tamura et al., 2008; Tamura et al., 2016); at the same time, the open-water is no longer protected by an insulating layer of sea ice, thus being exposed to strong cooling from the atmosphere ($\sim -30^{\circ}\text{C}$, Turner et al., 2009). These two processes are the primary cause of Dense Shelf Water (DSW) formation on the Antarctic continental shelf; after filling the deeper parts of the shelf and reaching the sill depth, DSW starts spilling off the shelf. While cascading down the continental slope, DSW mixes with warmer ambient water (mostly Circumpolar Deep Water; CDW), to finally form Antarctic Bottom Water (AABW; Orsi et al., 1999). AABW, in turn, fills the abyssal layers of the global ocean and plays an important role in the global MOC (see Section 1.1; Gordon et al., 2014; Orsi et al., 1999). During the past four decades, DSW formed in coastal polynyas and the related DSW overflows were the main source of AABW. Coastal polynyas are often short-lived, remaining open for just a few days to a few weeks (Markus et al., 1998); thus, although they may exist in climate model simulations, the typical monthly-mean model output cannot represent them very well and they generally only show up as lower ice thickness (Kurtakoti et al., 2018).

Open ocean polynyas (OOPs) form far away from the coast and mostly in the Weddell Sea (e.g., Morales Maqueda et al., 2004). There, OOPs form sporadically at distinct locations that are preconditioned by weak stratification (Gordon et al., 2014; de Lavergne et al., 2014; Stössel et al., 2015). Based on their formation location, small open-ocean polynyas that occur over and around the Maud Rise seamount have been termed “Maud Rise Polynyas” (MRPs), while the term “Weddell Sea Polynya” (WSP) has been used to describe the large open-ocean polynya that develop into the central Weddell Sea (Kurtakoti et al., 2018; Gordon and Huber, 1990; Gordon et al.; 2014). A WSP was first observed in September 1974 (when the first satellite passive-microwave data became available); and it reoccurred over three consecutive winters (1974-1976) (Carsey, 1980; Zwally et al., 1983). From 1977 to 2021, such large polynyas have not been observed; trends towards a fresher, more stratified Weddell Sea may have suppressed the occurrence of WSPs (de Lavergne et al., 2014; Gordon, 2014). However, smaller MRPs recurred more frequently, with the largest MRPs occurred in 2016 and 2017 (Jena et al., 2019; Campbell et al., 2019).

Both modeling and observations-based studies have shown that a weak ocean stratification is key to the occurrence of the OOPs (de Lavergne et al. 2014; Stössel et al. 2015; Campbell et al., 2019). Increased stratification due to enhanced freshwater fluxes at the surface was found to hamper the formation of polynyas (de Lavergne et al. 2014; Stössel et al. 2015; Kjellsson et al. 2015). In contrast, decreased stratification, resulting from the buildup of high salinity water at the surface, was found to favor the occurrence of polynyas (Kjellsson et al. 2015; Heuzé et al. 2015). By eliminating the sea ice barrier,

OOPs expose the ocean surface water directly to the frigid atmosphere. This will make the warmer than freezing point water denser to eventually become dense enough to sink, which will be replaced by the more buoyant WDW from below, thereby sustaining the deep convection (Dufour et al., 2017). This process transports a huge amount of heat from the WDW layer to the surface, maintaining the ice-free conditions (Gordon, 1978; Gordon et al., 2014). The deep convection inside the OOPs can reach as deep as 3000m (Gordon et al., 2014), and thus can rapidly modify the ocean interior water, and provide a second source for the production of AABW (in addition to the DSW overflow discussed earlier; Gordon et al., 2014), thereby also contributing to driving the global thermohaline circulation (Martin et al., 2013; Cheon et al., 2014). Furthermore, in this process, a huge amount of heat is released from the deep heat reservoir to the atmosphere, which is expected to affect the regional atmospheric conditions, such as the SLP, the precipitation, and wind conditions (Moore et al., 2002; Maqueda et al., 2004; Weijer et al., 2017). Some recent numerical studies point out that the OOPs may have global impacts through atmospheric teleconnections (Chang et al., 2020).

OOPs first emerging near the Maud Rise seamount is not a coincidence (Gordon et al; 2014; Kurtakoti et al., 2018; Cambell et al., 2019). Both observational and modeling studies have shown that the Taylor column effect above the Maud Rise seamount prompt this region with both a crescent of lower sea ice concentration (Lindsay et al., 2004) and lower ocean stratification, which preconditions this area for deep convection (Kurtakoti et al., 2018). However, the intermittent opening of OOPs is mostly attributed to large-scale climate fluctuations, such as a change of the SAM index

(Gordon et al., 2014) and associated changes in precipitation, wind stress curl, and winter storm frequency (Gordon et al; 2014; Kurtakoti et al., 2018; Cambell et al., 2019). Gordon et al. (2014) suggests a possible link between the SAM index and OOPs occurrence: when the cold, dry polar air from the Antarctic continent spreads seawards, the ocean's surface layer receives less fresh water and a saltier, denser surface layer ensues (negative SAM). If the polar air remains confined over the Antarctic ice sheet, the westerly wind belt spreads more poleward, and the surface water becomes fresher and less dense (positive SAM). If a negative SAM persists over a few years, and the surface layer becomes salty enough, OOPs start developing. De Lavergne et al. (2014), based on observation results, further suggest that the anthropogenic forcing in recent decades induces a positive trend of the SAM index, which forces the precipitation-rich westerlies more poleward, thereby significantly freshening the surface water of the high-latitude Southern Ocean, finally suppressing the return of WSPs. Campbell et al. (2019) also agree with the point that the polynya is induced by changes of the SAM index, but they provide a different explanation: relatively high mixed layer salinity is induced by a strong negative wind stress curl (positive SAM), while turbulent mixing during more intense winter storms triggers more vertical overturning (positive SAM). Campbell et al. (2019) also notice that the mid-depth water temperature did not change much before the 2016 MRP event, suggesting that the deep heat reservoir was not the immediate cause for its initiation.

To summarize, three main processes have been identified to be important for the intermittency of the occurrence of OOPs: (1) the heat reservoir of the WDW layer,

which provides the heat source to maintaining ice-free conditions (Martin et al., 2013; Dufour et al., 2017); (2) the Maud Rise seamount, which induces the Taylor column effect and makes the stratification locally weaker, and preconditions this region for OOPs to first occur there (Kurtakoti et al., 2018; Lindsay et al. 2004); (3) the SAM index change, which induces an increase of the surface salinity, and eventually destabilizes the upper ocean and eventually triggers deep convection (Gordon 2014; de Lavergne et al., 2014; Cheon et al., 2014; Campbell et al., 2019).

1.3. Overview of Antarctic Slope Current

The Antarctic Slope Current (ASC) is a near-circumpolar, westward flowing current that tracks the Antarctic continental shelf break and slope (Jacobs 1991; Thompson et al., 2018). Observations show that the typical velocity of the ASC is about 10–30 cm/s (Jacobs 1991; Thompson et al., 2018). Yet it remains remarkably understudied due to the harsh environment. A portion of the ASC is associated with the Antarctic Slope Front (ASF), a subsurface front that separates the offshore mid-depth warm and salty Circumpolar Deep Water (CDW) from the typically cold and fresh waters on the continental shelf (Whitworth et al., 1998). The ASC and ASF therefore mediate exchanges of waters between the open ocean and the continental shelf (Orsi et al., 1999; Gordon et al., 2004; Jacobs et al., 2002). According to Thompson et al. (2018), the ASC/ASF can be classified into three types based on the hydrographic properties over the continental shelves: (1) “fresh shelf”, (2) “dense shelf”, and (3) “warm shelf”: (1) Over large parts of East Antarctica and the eastern Ross Sea, persistent and strong easterly winds are located over the continental shelf (see section 1.1). This

induces a strong westward flowing ASC, furthermore, the Coriolis force causes the westward blowing winds along the Antarctic coast to produce an onshore Ekman transport (Chavanne et al., 2010). This, in turn, causes coastal downwelling (Chavanne et al., 2010), which makes the shelf water relatively cold and fresh (Thompson et al., 2018). The “fresh shelf” is thus characterized by density surfaces that tilt down from the surface toward the Antarctic continental slope (Orsi and Whitworth, 2005; Chavanne et al., 2010). In contrast to the other ASC regimes, the “fresh shelf” density front is sufficiently strong and is an effective barrier, as it interrupts the pathway for a direct transport of warm CDW waters onto the continental shelf (Dong et al., 2016).

(2) The Dense Shelf Water (DSW) forms in four major sites around the Antarctic margins: the western Ross Sea (Whitworth & Orsi, 2006; Gordon et al., 2009), the Weddell Sea (Gordon et al., 1993; Nicholls et al., 2009), the Adélie coast (Williams et al., 2010), and Cape Darnley (Ohshima et al., 2013). The DSW formation process is closely related to the existence of coastal polynyas (see section 1.2). DSW overflow leads to water mass transport across the continental shelf break, which has a significant impact on the ASC and ASF (Foster & Carmack, 1976). Most notably, these “dense shelf” regions tend to be associated with a distinct “V-shape” frontal structure (Whitworth, 1998): over the outer side of the continental slope, the density surfaces also tilt down (like in the fresh shelf case); however, the density surfaces start tilting up as they approach the shelf break, thus forming the “V-shaped” distribution of isopycnals. The upward tilt of isopycnals at the shelf break allows the heavier DSW to be carried out across the shelf break in a dense outflow layer (Baines and Condie, 1998; Gill, 1973;

Ou, 2007), and water masses with a relatively large range of density classes to directly access the continental shelf (Thompson et al., 2018). The DSW can sink to more than 2000 m, thereby mixing with ambient CDW to eventually attain the properties of AABW (Gordon 2001; Orsi et al., 2001), which further controls the global overturning circulation over millennial time scales (Ferrari et al., 2014; Burke et al., 2015). Finally, it should be noted that, in these “dense shelf” regimes, the numerical models need a very high resolution of up to about 1 km to capture these important processes, including mesoscale eddies and the width of DSW overflow plumes (St-Laurent et al., 2013; Stewart et al., 2019).

(3) The ASC is not an entirely circumpolar feature (Thompson et al., 2018); due to the blocking effect of the Antarctic Peninsula, it is not observed along the West Antarctic Peninsula and emerges only very weakly along West Antarctica (Turner et al., 2013). The “warm shelf” regime forms where the warm CDW has nearly unlimited access onto the shelf (Jenkins and Jacobs, 2008). Furthermore, the weaker easterly or even westerly winds induce an upward-tilting CDW in the “warm shelf” region, which further enhance the CDW onshore intrusion (Schmidtko et al., 2014). On this type of continental shelf, the typical water temperature exceeds 0°C, being about 2-3°C warmer than the freezing point. Thus, the warm shelf environment is also the site where Antarctic ice shelves are thinning rapidly (from basal melt) in recent decades (Pritchard et al., 2012). Of particular interest in recent years is the potential collapse of the Thwaites Glacier iceshelf in this “warm shelf” regime (Gramling, 2021).

1.4. Research motivation and questions

For my dissertation I took advantage of an unprecedented 500-year-long high-resolution CESM1.3 simulation that has been run with preindustrial (year 1850) radiative boundary conditions (HR-PI). It provides a unique opportunity to study the mechanisms responsible for the intermittent occurrence of OOPs. Furthermore, an accompanying 250-year-long high-resolution CESM1.3 transient simulation run under historical and future radiative conditions from year 1850 to year 2100 (HR-TN) helps identify the possible anthropogenic forcing effects on the occurrence of WSPs and the associated open ocean deep convection. Furthermore, by running corresponding low-resolution simulations (LR-PI and LR-TN) with overflow parameterization, provides the opportunity to study the effect of model resolution and overflow parameterization on the representation of the ASC and DSW overflow process. This dissertation primarily addresses the following questions:

- 1) What is the mechanism that controls the intermittent occurrence of OOPs in HR-PI?
- 2) What effect does the anthropogenic forcing have on the intermittent formation of OOPs and the associated open ocean deep convection?
- 3) How does the model resolution and the overflow parameterization influence the representation of the ASC and the associated DSW overflow process?
And what effect does the anthropogenic forcing on them?

This dissertation is organized as follows: the CESM1.3 model, and the HR-PI, HR-TN, LR-PI, and LR-TN simulations are described in Chapter 2. Chapter 3 describes

the mechanisms that control the intermittent occurrence of OOPs in HR-PI. Chapter 4 focusses on the anthropogenic forcing effect on the intermittent formation of OOPs and the associated open ocean deep convection. Chapter 5 discusses the anthropogenic impact on the ASC and the DSW overflow process. Finally, Chapter 6 summarizes the main findings of this dissertation. The specific analysis methods will be described in detail in each chapter, respectively.

CHAPTER II

MODEL CONFIGURATIONS AND SIMULATIONS¹

2.1. Community Earth System Model version 1.3

My dissertation research findings are based primarily on simulations conducted with the Community Earth System Model version 1.3 (CESM1.3) developed by the National Center for Atmospheric Research (NCAR) in collaboration with the broader climate modeling community (Meehl et al., 2019; Chang et al., 2020). The CESM1.3 component models are the Community Atmosphere Model version 5 (CAM5; Neale et al., 2012), the Parallel Ocean Program version 2 (POP2; Danabasoglu et al., 2012; Smith et al., 2010), the Community Ice Code version 4 (CICE4; Hunke and Lipscomb, 2008), and the Community Land Model version 4 (CLM4; Lawrence et al., 2011). As summarized by Meehl et al. (2019) and by Chang et al. (2020), the most significant improvements from CESM1.1 to CESM1.3 were made in the CAM5 component with moving from a Eulerian to a Lagrangian vertical advection scheme within the spectral element dynamical core. These improvements made CESM1.3 have a better representation of the Southern Hemisphere jets and clouds (Meehl et al., 2019). In the simulations analyzed in this study, CAM5 has a horizontal resolution of either 1° (LR) or 0.25° (HR) and the standard 30 levels in the vertical, with a model top at 3 hPa (Small et al., 2014; Chang et al., 2020). The POP2 model has a nominal grid spacing of either 1° (LR) or 0.1° (HR). The 0.1° ocean model uses a partial grid cell topography (Maier-

¹ Partly published in Journal of Advances in Modeling Earth System as one co-author (Chang et al., 2020)

Reimer et al., 1993; Adcroft et al., 1997) with a maximum depth of 6,000 m and 62 levels, while the 1° ocean model uses a full cell topography with a maximum depth of 5,500 m and 60 levels. Compared to lower vertical resolution simulations with 42 levels (e.g., Kirtman et al., 2012; Kurtakoti et al., 2018), more levels have been added in the main thermocline to better represent the upper-ocean stratification (Small et al., 2014). The land model is run at the same resolution as the atmosphere model, while the sea ice model is run at the same resolution and grid as the ocean model, respectively. CESM1.3 neither resolves ice shelf cavities nor is it coupled to a dynamic ice sheet model. Instead, the contribution from “glacial meltwater” is crudely represented as an instantaneous freshwater runoff from the Antarctic continent (Danabasoglu et al., 2012; Goddard et al., 2017). No mesoscale and sub-mesoscale eddy transport parameterization is used in the 0.1° POP2 version; furthermore, overflow processes are also not being parameterized in the 0.1° version (Chang et al., 2020; Danabasoglu et al., 2010). In contrast, the POP2 version of the one order of magnitude lower resolution simulations (1°) includes both mesoscale and sub-mesoscale eddy parameterizations (Gent & McWilliams, 1990), and the overflow parameterization (Danabasoglu et al., 2010). Tides are not considered in any of these CESM1.3 simulations in this study (Meehl et al., 2019; Chang et al., 2020).

2.2. High-Resolution Preindustrial Control Simulation (HR-PI)

The experimental design of the high-resolution (0.1° version POP2 and CICE4; 0.25° version CAM5 and CLM4) preindustrial simulation (HR-PI) follows the protocol of the Coupled Model Intercomparison Project phase 5 (CMIP5) experiments (Eyring et

al., 2016). The HR-PI ocean component was initialized with the January-mean climatological potential temperature and salinity from the World Ocean Atlas (WOA; Locarnini et al., 2013; Zweng et al., 2013) and from a state of rest. The other model components were initialized from restart files of previous simulations (Chang et al., 2020). The climate forcing was set to year 1850 conditions and kept constant throughout the entire 500-year simulation.

2.3. High-Resolution Transient Climate Simulation (HR-TN)

The high-resolution historical and future transient climate simulation (HR-TN) was branched from the year 250 of the HR-PI simulation. It uses historical forcing from year 1850 to 2005, and Representative Concentration Pathway 8.5 (RCP8.5) forcing from year 2006 to 2100 (Lamarque et al., 2010, 2011; Meinshausen et al., 2011) in accordance with the CMIP5 experimental protocol. Stratospheric ozone concentrations were calculated using a high-top coupled chemistry-climate model with specified ozone depleting substances (Marsh et al., 2013; Chang et al., 2020).

2.4 Corresponding Low-Resolution (LR) Simulations

To address some key scientific questions concerning the impact and benefit of increasing model horizontal resolution in climate simulations, and to arrive at a relatively rigorous comparison between HR and LR simulations, an identical set of LR (1° version POP2 and CICE4; 1° version CAM5 and CLM4) CESM1.3 simulations were also conducted (Chang et al., 2020) for reference. To achieve an acceptable top-of-

atmosphere radiation balance, some model parameters were reset in the LR simulations (see more details in Chang et al., 2020). The corresponding LR preindustrial control simulation (LR-PI) and LR historical and future transient climate simulation (LR-TN) use the same climate forcing as their counterparts in HR simulations. Note here again, the LR (1°) POP2 includes both mesoscale and sub-mesoscale eddy parameterizations, as well as an overflow parameterization, which help the LR simulations to have a better representation of these corresponding sub-grid scale processes.

2.5 The advantages and disadvantages of the described simulations

As I discussed in Section 1.1, the patterns of the global atmosphere circulation and the global ocean circulation (and their interaction) can only be represented in global coupled climate models or ESMs. However, with the currently available computing power, the standard IPCC-class global climate models are restricted to grid spacings of around 1° (Small et al., 2014). Although these standard models adequately resolve large scale modes of climate variability (such as El-Niño Southern Oscillation (ENSO) and SAM), they cannot capture smaller-scale features, such as tropical cyclones, mesoscale ocean eddies and fronts, and MRPs (Small et al., 2014; Chang et al., 2020; Kurtakoti et al., 2018). However, these smaller-scale features have important local impacts and may exert feedbacks on the large-scale climate modes (Small et al., 2014; Chang et al., 2020). There are several different numerical approaches to deal with the smaller-scale features in a global climate model: (1) “regional downscaling” is a straightforward and efficient method to calculating the effect of large scales on smaller scales, however, it lacks the

feedback of the smaller scales on the larger scales (Small et al., 2014); (2) “mesh refinable global grids” offer promise to refine the numerical mesh locally in the area of interest, and at the same time include all scale interactions (e.g., the newly developed Models for Prediction Across Scales (MPAS) in E3SM; Ringler et al., 2013); this approach, however, faces new numerical challenges, e.g., how to make parameterizations act across the different scales; (3) finally, globally HR models include all the advantages of methods (1) and (2), and none of their disadvantages, with the important pragmatic exception that they need a huge amount of computing resources and data storage space (Small et al., 2014).

Several earlier relatively short-term HR ESM simulations revealed processes not seen in their LR counterparts, for example: a better representation of the Southern Hemisphere storm tracks (Meehl et al., 2019); the occurrence of MRPs (Kurtakoti et al., 2018); and a better representation of the air-sea interaction over ocean frontal zones (e.g., Small et al., 2014; Roberts et al., 2020). However, these previous simulations were limited to relatively short integration times (less than 200 years, e.g., Small et al., 2014; Kurtakoti et al., 2018; Roberts et al., 2020). Compared to these earlier studies, the set of HR ESM simulations used in this study have several advantages as summarized below:

(1) The HR-PI integration analyzed in this study is unprecedentedly long (500 years; Chang et al., 2020) for the given horizontal resolutions of the individual model components. This provides a better opportunity for a thorough study of, e.g., the intermittent occurrence of OOPs that do not even emerge in LR-PI.

(2) The HR ESM used in this study captures the dominant planetary-scale climate modes of variability and the small-scale regional weather features simultaneously, which is suitable for studying the climate interactions across these scales (Small et al., 2014).

(3) HR-TN, branched from year 250 of HR-PI, and continuing from historic forcing to RCP8.5 anthropogenic forcing (including human impact on atmospheric carbon dioxide and stratospheric ozone concentration), provide us with the opportunity of a comprehensive study of the anthropogenic impact on remote regions around Antarctica.

(4) In contrast to the LR simulations, the HR simulations do not include any parameterizations of the mesoscale and sub-mesoscale eddy transport and DSW overflow, as the associated processes are expected to be partly resolved by the governing equations of the HR ocean model. This provides us with the opportunity to study not only the effects of the difference in model resolution, but also the effect of added parameterizations in the LR ocean model component of CESM1.3. The ASC and the DSW overflow are good case processes to study the influence of the parameterizations together with different model resolutions.

However, there are also several inevitable problems with basing conclusions on the output of the described ESM simulations:

(1) On the Antarctic continent shelf, the horizontal ocean grid size needs to reach to about 1 km to resolve the full mesoscale eddy field (Hallberg, 2013; Goddard et al., 2017; Meehl et al., 2019). Thus, even the HR CESM1.3 is underrepresenting the

mesoscale eddy activity near Antarctica, which may limit the model representation of the ASC (Thompson et al., 2018) and the DSW overflow process (Dufour et al., 2017).

(2) When comparing HR with LR simulation results it is hard to distinguish between the effects of model resolution and that of the sub-grid scale parameterizations, especially that of the DSW overflow.

(3) I will continue to elaborate on the limitations of these simulations later in Chapters 3, 4, 5, and 6, after I analyzed the comprehensive model output in detail (e.g., the deep ocean climate drift and unresolved first-order processes such as convection).

CHAPTER III

THE INTEMITTENT OCCURRENCE OF OPEN-OCEAN POLNYAS IN HR-PI²

3.1. Background information

An open-ocean polynya is a large area of open water surrounded by sea ice that forms far away from the coast (e.g., Morales Maqueda et al., 2004). In the Weddell Sea, open-ocean polynyas form usually at distinct locations that are preconditioned by weak stratification and are thus prone to deep convection. Based on the results from HR-PI, and previous work by Kurtakoti et al. (2018, 2021), we distinguish the following open-ocean polynyas: Maud Rise Polynya (MRP, Figure 3.1a), Astrid Ridge Polynya (ARP, Figure 3.1b), and Weddell Sea Polynya (WSP, Figure 3.1c). While somewhat arbitrary, we follow Kurtakoti et al. (2018) in defining MRPs and ARPs as relatively small open-ocean polynyas that occur over and around the Maud Rise seamount and the Astrid Ridge, while considering WSPs to be large open-ocean polynyas that reach into the central Weddell Sea. The Prime Meridian (black line in Figure 3.1) has been used to distinguish MRPs from WSPs, or rather to determine when a MRP has grown into a WSP. A WSP was first observed in September 1974 (when the first satellite passive-microwave data became available) and lasted over multiple winters (1974–1976) (Carsey, 1980; Zwally, 1983). From 1977 to 2020, such large polynyas have not been observed. Trends toward a fresher, more stratified Weddell Sea may have suppressed the occurrence of WSPs (de Lavergne et al., 2014; Gordon, 2014). However, more recently,

² Reprinted from “On the Intermittent Occurrence of Open-Ocean Polynyas in a Multi-Century High-Resolution Preindustrial Earth System Model Simulation” by Diao et al., 2022, Journal of Geophysical Research: Oceans. DOI: 10.1029/2021JC017672. Copyright [2022] by © American Geophysical Union. Used with permission.

the largest and most prolonged MRP was observed in the austral winter of 2016–2017 (Jena et al., 2019; also called WSP in; Francis et al., 2020). The first comprehensive observations of it were presented by Campbell et al. (2019). More specifically, Campbell et al. (2019) reveal that relatively high mixed layer salinity induced by strong negative wind stress curl preceded the formation of the MRP, while turbulent mixing during intense winter storms triggered overturning. They also noted that the mid-depth water temperature did not change much before the 2016 MRP event, suggesting that the deep heat reservoir was not the cause for its initiation.

This recent MRP drew the ocean and climate research community's attention again by raising questions such as: How often do polynyas re-emerge? Is there an inherent periodicity of about 40–50 years (from 1974 to 2016)? What are the mechanisms that control the formation of polynyas? Although these observations provide us with many intriguing facts and clues, two major polynya events in about 50 years of observational history are not enough to give a full picture of the mechanisms behind this phenomenon.

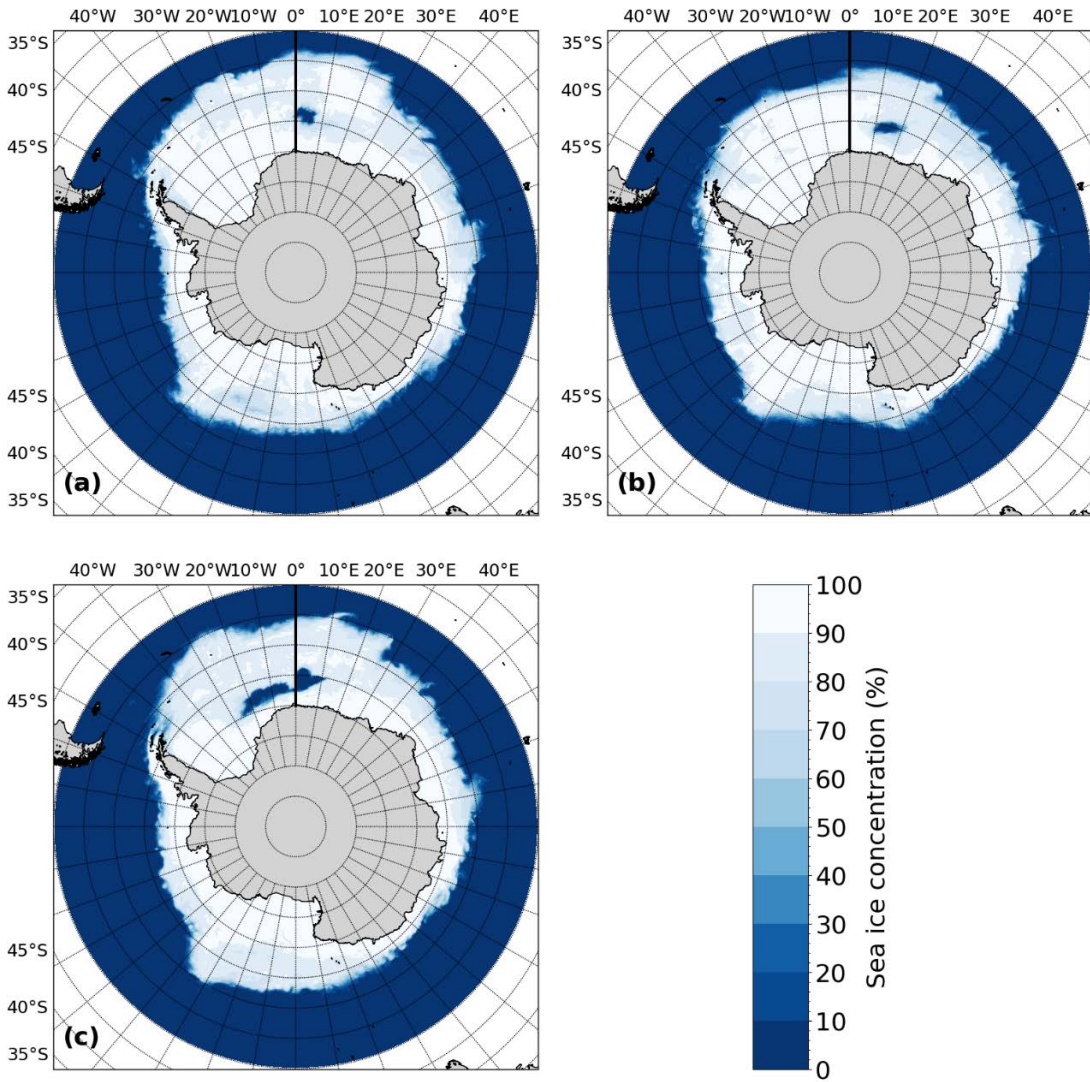


Figure 3.1. (a) Simulated September sea-ice concentration showing different polynya types in the Weddell Sea. (a) Maud Rise Polynya (MRP). (b) Astrid Ridge Polynya. (c) Weddell Sea Polynya (WSP). The Prime Meridian (black line) has been used to distinguish MRPs from WSPs.

Polynyas open a window between the frigid atmosphere and relatively warm ocean waters, which induces intense deep convection (especially in the case of WSPs). Deep-penetrating convection makes warm and salty Weddell Deep Water (WDW) rise, thus releasing a large amount of heat and moisture to the atmosphere, while sustaining

convection as the salty water gets denser as it cools at the surface (Gordon & Huber, 1990; Martinson et al., 1981). The emergence of a polynya therefore has a substantial influence on not only the ocean, but also on the atmosphere (e.g., Weijer et al., 2017). On the other hand, the atmosphere apparently plays a decisive role in modulating the physical conditions that generate polynyas. Cheon et al. (2014, 2015, 2018), for example, find that a negative wind stress curl anomaly in association with a positive SAM index is the main driver that initiates WSPs in forced low-resolution ocean model simulations. The precipitation within the belt of the westerlies is high (Montade et al., 2019). Changes in the meridional gradient of surface air pressure causes changes in the strength and position of the westerlies, and thus the location of maximum precipitation (Montade et al., 2019). Gordon et al. (2007) proposed a link between SAM and WSPs based on the observational record, but primarily for the 1974–1976 WSP event.

Based on a 500-year-long high-resolution CESM simulation, Chang et al. (2020) reported on a strong link between WSP events and the Interdecadal Pacific Oscillation, which suggests that the atmospheric signals induced by polynyas could reach as far as the western equatorial Pacific region. In the ocean, the switch from periods of deep convection and associated WSPs to periods of recovery when there is no WSP leads to Antarctic Bottom Water (AABW) anomalies. Based on low-resolution forced sea-ice-ocean model experiments, Stössel and Kim (2001) found that AABW anomalies propagate along the deep western boundary to the Argentine Basin and beyond, where they appear to have a significant impact on the Atlantic Meridional Overturning Circulation by modifying the southward flow of the North Atlantic Deep Water across

30°S. This behavior has also been detected in more recent modeling experiments with low-resolution models (e.g., Hirabara et al., 2012; Martin et al., 2015, 2013; Patara & Böning, 2014; Zanowski & Hallberg, 2017). Finally, many low-resolution long-term (more than 1,000 years) model experiments simulate WSPs as a recurring feature. Martin et al. (2013), for example, find a periodic occurrence of polynyas in their coupled Kiel Climate Model simulations. Jüling et al. (2018) report a periodic occurrence of deep convection in forced high-resolution (0.1°) ocean model simulations.

Modeling studies involving high-resolution ESMs have shown that the overall representation of stratification is key to the occurrence of polynyas in the Weddell Sea (e.g., Dufour et al., 2017; Lockwood et al., 2021; Stoessel et al., 2015). A critical variable for stratification is the upper-ocean salinity, which is controlled by the freshwater flux due to precipitation and evaporation (Gordon et al., 2007), by upwelling that varies with the magnitude of the cyclonic wind stress curl (Campbell et al., 2019), by lateral advection (Kurtakoti et al., 2018), and/or by the freshwater flux due to sea-ice growth and decay (Haumann et al., 2016). Saltier surface waters can potentially decrease the static stability of marginally stably preconditioned regions affected by the Taylor cap effect to the point that deep-penetrating convection and polynya formation occur (e.g., Kurtakoti et al., 2018).

The most recent state-of-the-art high-resolution ESMs provide us with new opportunities to study polynyas (e.g., Chang et al., 2020; Kurtakoti et al., 2021, 2018; van Westen & Dijkstra, 2020). In addition to being fully coupled and global, they are particularly useful for the purpose of studying polynyas as their high-resolution

bathymetry allows for a realistic representation of the flow around extreme ocean floor reliefs such as the Maud Rise seamount and the Astrid Ridge that ultimately precondition this region for polynya formation. On the other hand, some ESMs produce open-ocean polynyas also at low resolution (e.g., de Lavergne et al., 2014; Gutjahr et al., 2019; Martin et al., 2013), from which it can be concluded that their production of polynyas most likely occurs for the wrong physical reasons (e.g., Kurtakoti et al., 2018). The new multi-century (500 years) high-resolution ESM simulation introduced and described by Chang et al. (2020) produces open-ocean polynyas only in its high-resolution configuration. The unprecedented length of this high-resolution simulation has the additional benefit of allowing for a thorough study of the variability and trend of polynya occurrence. Long simulations can overcome the limitations of the relatively short observational record, in particular as far as the occurrence of WSPs is concerned (e.g., Gordon, 2012).

In this Chapter, which is based on the 500-year-long HR-PI simulation, we address the following main questions. First, what are the mechanisms that drive the quasi-periodic formation of open-ocean polynyas? Second, what determines the location and size of open-ocean polynyas in the Weddell Sea? Third, how well do the simulated polynya processes match with the observed polynya events? Fourth, what needs to be improved in the model to capture polynyas more realistically? Finally, what controls the 40-50-year periodicity of open-ocean polynya occurrence in the model? Our study builds on previous studies on this topic (Campbell et al., 2019; Cheon et al., 2018, 2014; Cheon

& Gordon, 2019; Gordon et al., 2007; Gordon, 2014; Kurtakoti et al., 2021, 2018; van Westen & Dijkstra, 2020).

3.2. Data and methodology

The dataset used in this Chapter is the 500-year high-resolution HR-PI simulation that have been described in detail in Chapter 2.

Our study focuses on the region that extends in longitude from upstream of the Astrid Ridge region to the slope region of the Antarctic Peninsula, and in latitude from the northern boundary of the Maud Rise seamount to the northern boundary of the Antarctic Slope Current (63°S – 68°S , 20°E – 40°W ; yellow box in Figure 3.2). According to the topography and the location where the polynyas form, we further divide this region into three smaller regions (see Figure 3.2). To identify the periodicity of the polynya events and its change over time, we used a common wavelet analysis tool (Python waipy package based on Torrence and Compo [1998], and Maraun and Kurths [2004]). To emphasize differences between WSP years and no-WSP years, we conducted composite analyses of specific variables. By projecting the upper-ocean temperature and salinity in a T-S diagram, we examine the factors that determine the critical surface density that eventually triggers convective overturning. After averaging over the three regions displayed in Figure 3.2, we use 70% sea ice concentration as the threshold for periods with polynyas (<70%) and periods with no polynyas (>70%). The mixed-layer depth is defined as the shallowest depth where the local buoyancy gradient equals the largest buoyancy gradient of the total water column (Chang et al., 2020; Large et al., 1997). In the literature one finds terms like “mixed-layer salinity,” or “sea-surface

salinity,” or “upper-ocean salinity.” Here we use “upper-ocean salinity” as an approximate estimate of mixed-layer salinity that does not depend on the mixed-layer depth, with the understanding that it represents the mean salinity of the upper-most ocean model layer that, in this model, has a thickness of 10 m. For the latter reason we also avoid using the term “sea-surface salinity” (or SSS). Finally, we estimated the Weddell Gyre strength from the westward (zonal) transport across the meridional section along 0°E, extending from 60°S to the coast.

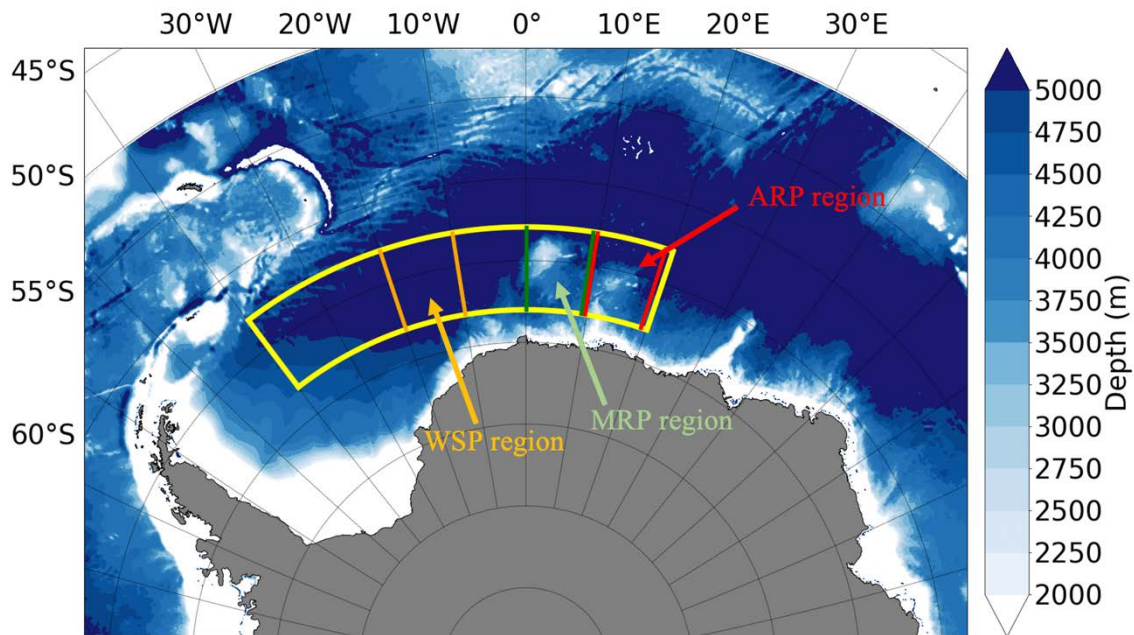


Figure 3.2. Bathymetry of the Weddell Sea below 2,000 m. Selected regions referenced in text: the WSP region (20° – 10° W, between orange lines), the MRP region (0° – 10° E, between green lines), the ARP region (10° – 20° E, between red lines). Yellow box (between 63° – 68° S and 40° W– 20° E) used for analysis of specific variables, for example, Hovmöller diagrams in Figure 3.3.

3.3. Variability of Polynya Occurrence and Its Relation to Upper-Ocean Salinity

The time-space evolution of the simulated polynyas is illustrated in Figure 3.3a in the form of a time-longitude diagram of September sea-ice concentration averaged over the latitudinal band of 63°S–68°S (yellow box in Figure 3.2), September being the month with the seasonal maximum of sea ice area. The polynyas are predominantly initiated in the longitudinal band of Maud Rise seamount (between green lines) and, to a lesser degree, in the longitudinal band of Astrid Ridge (between red lines). Some MRPs grow into WSPs, as can be detected by the shorter pulses of low ice concentration in the longitudinal band of the central Weddell Sea (between yellow lines). The corresponding evolution of the simulated September upper-ocean salinity and mixed-layer depth are illustrated in Figure 3.3b and Figure 3.3c, respectively. High upper-ocean salinity (in excess of 34.65 psu) coincides with deep mixed layers (Figure 3.3c) and the existence of polynyas (Figure 3.3a) in the MRP and ARP regions. Deep convection brings warm and salty WDW to the surface; this leads to the formation of MRPs and ARPs and renders the upper-ocean saltier. The upper-ocean salinity remains relatively high in the WSP region for many years, even after the WSPs have already closed. Since the center of action in terms of polynya formation is the MRP (and ARP) region throughout this simulation, and WSPs spawn occasionally from this region, we propose that vigorous convection associated with MRPs always precedes WSPs.

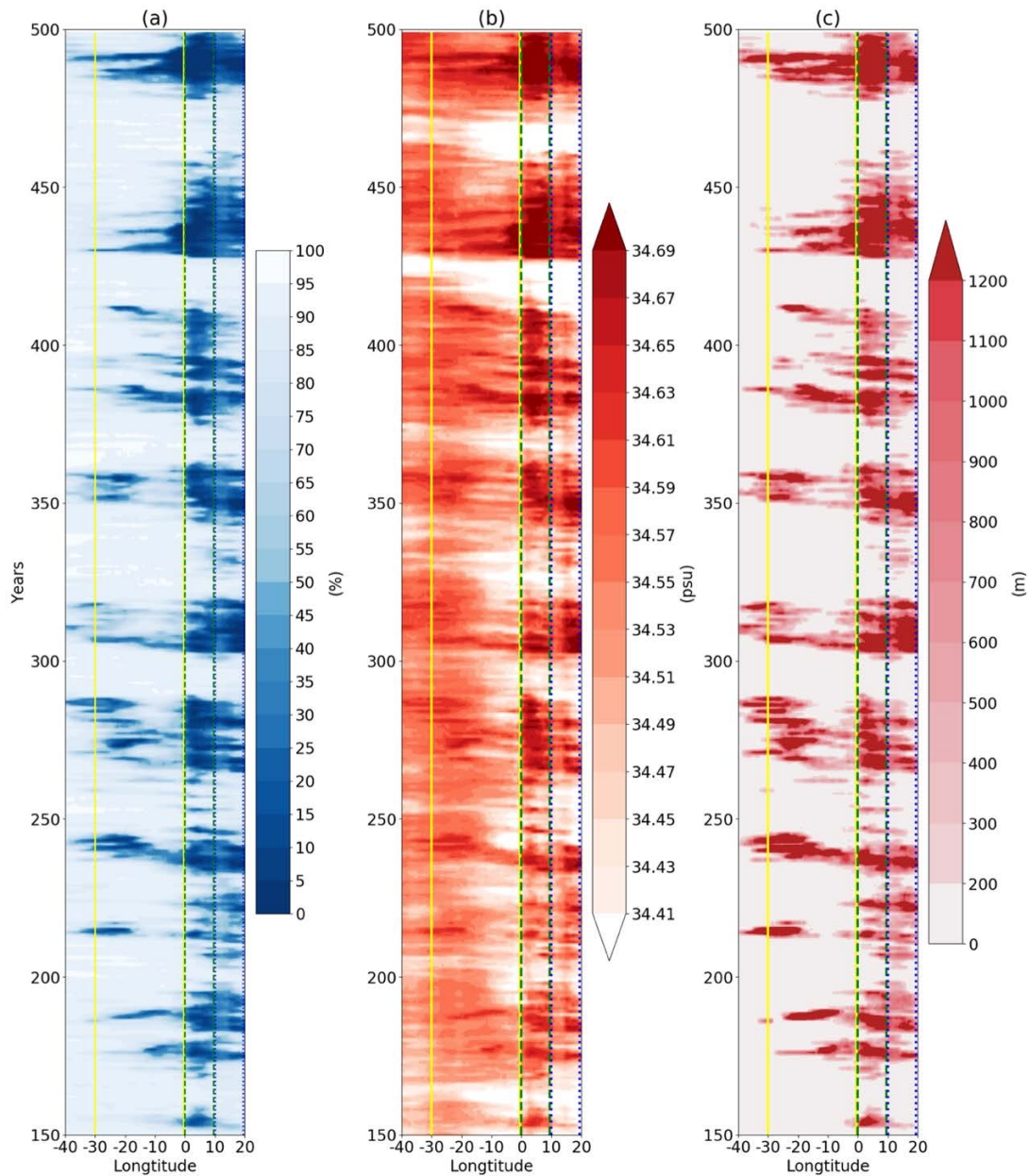


Figure 3.3. Time-longitude plots of simulated September (a) sea ice concentration, (b) upper-ocean (top 10 m) salinity, and (c) mixed-layer depth averaged between 63°S and 68°S. The three regions bounded by different colors correspond to those in Figure 3.2.

To further understand the co-variability in different regions, Figure 3.4 shows the sea ice concentration and upper-ocean salinity time series averaged over the three regions displayed in Figure 3.2. The 70% ice concentration threshold for polynya

occurrence (Figure 3.4a; gray shadings), while arbitrary, reasonably reflects the patterns in Figure 3.3a in the respective polynya regions, with MRPs and ARPs clearly occurring more frequently than WSPs. Figure 3.4b shows the corresponding variability of September upper-ocean salinity. The negative correlation between the upper-ocean salinity and the sea ice concentration of the respective regions reaches its highest value when there is no lag between the two variables ($r = -0.91$ for the ARP region, $r = -0.92$ for the MRP region, and $r = -0.69$ for the WSP region). This reflects that deep convection dominates the upper-ocean salinity change. The negative correlation being highest in the MRP region indicates that deep convection is most pronounced above and around the Maud Rise seamount. While instantaneous local deep convection in the WSP region still contributes to the upper-ocean salinity change, the lower correlation is mainly due to the fact that WSPs occur less frequently, and that during the relatively long (multi-decadal) no-WSP phases the upper-ocean salinity changes due to other processes, such as changes of the surface freshwater flux (see Section 3.4).

Referring to Figure 3.4b, in order to study the polynya trigger process, we separate the upper-ocean salinity increase into two phases: (a) the polynya phase, during which the upper-ocean salinity increase is mainly induced by deep convection; (b) the no-polynya and polynya initiation phase, during which the upper-ocean salinity increases slowly, and eventually triggers a polynya, upon which the upper-ocean salinity increases abruptly due to initiation of convection. The second phase has been explained in the observation-based work on the 2016 and 2017 MRP events by Campbell et al. (2019). They measured upper-ocean salinity that exceeded the climatological mean value before

both MRP events. Additionally, the observed upper-ocean salinity shows a clear seasonal fluctuation, with high values in September and low values in February (their Figure 2b). Ultimately, it is the seasonal maximum of upper-ocean salinity superimposed on the higher-than-climatological value that triggered the MRP. In order to compare with this observation, we chose a simulated polynya that was initially triggered in September of model year 300 (Figure 3.5b; compared to Extended Data Figure 2 of Campbell et al., 2019). Consistent with the results of Campbell et al. (2019), the simulated upper-ocean salinity shows a clear seasonal fluctuation. In this simulation, there is also a multi-year increasing trend during years 297–301 (Figure 3.5a) that at some point exceeds the climatological value. The seasonal upper-ocean salinity fluctuation is associated with brine rejection when sea ice forms in the model. Combined with the multi-year increase, the seasonal salinity increases due to brine rejection ultimately exceed a critical threshold value for instability to trigger deep-penetrating convection and a polynya (the gray shaded area in Figure 3.5a, and the sea ice minimum in Figure 3.5b).

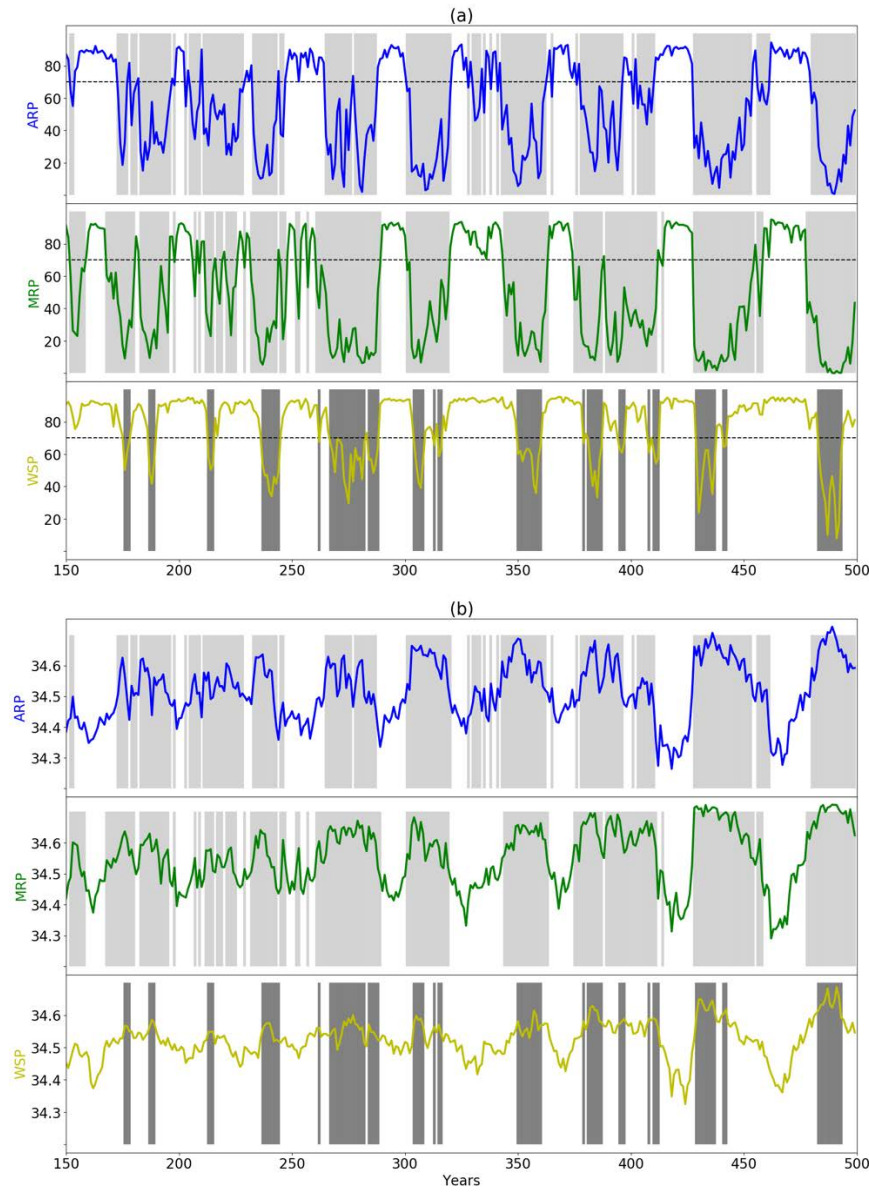


Figure 3.4. (a) Time series of sea ice concentration (September) averaged over the respective boxes shown in Fig. 2. **(b)** Same as (a), but for upper-ocean salinity. The shadings indicate ice concentration less than 70% in the respective box areas defined to be representative of polynya periods.

To identify the periodicity of polynya occurrence, we applied a wavelet analysis to the MRP region-averaged sea ice concentration time series shown in Figure 3.4a. The strongest signal in the MRP region has a period of about 40–50 years (Figure 3.6), and is

most pronounced between years 250 and 370, after which the period increases to about 50 years, possibly due to model drift. The wavelet for the WSP region is similar to that of the MRP region (not shown). Chang et al. (2020) conducted a preliminary analysis of the global signals of the same simulation discussed here and identified a ~40-year period in the global-average SST timeseries that is seemingly linked to the WSP occurrences.

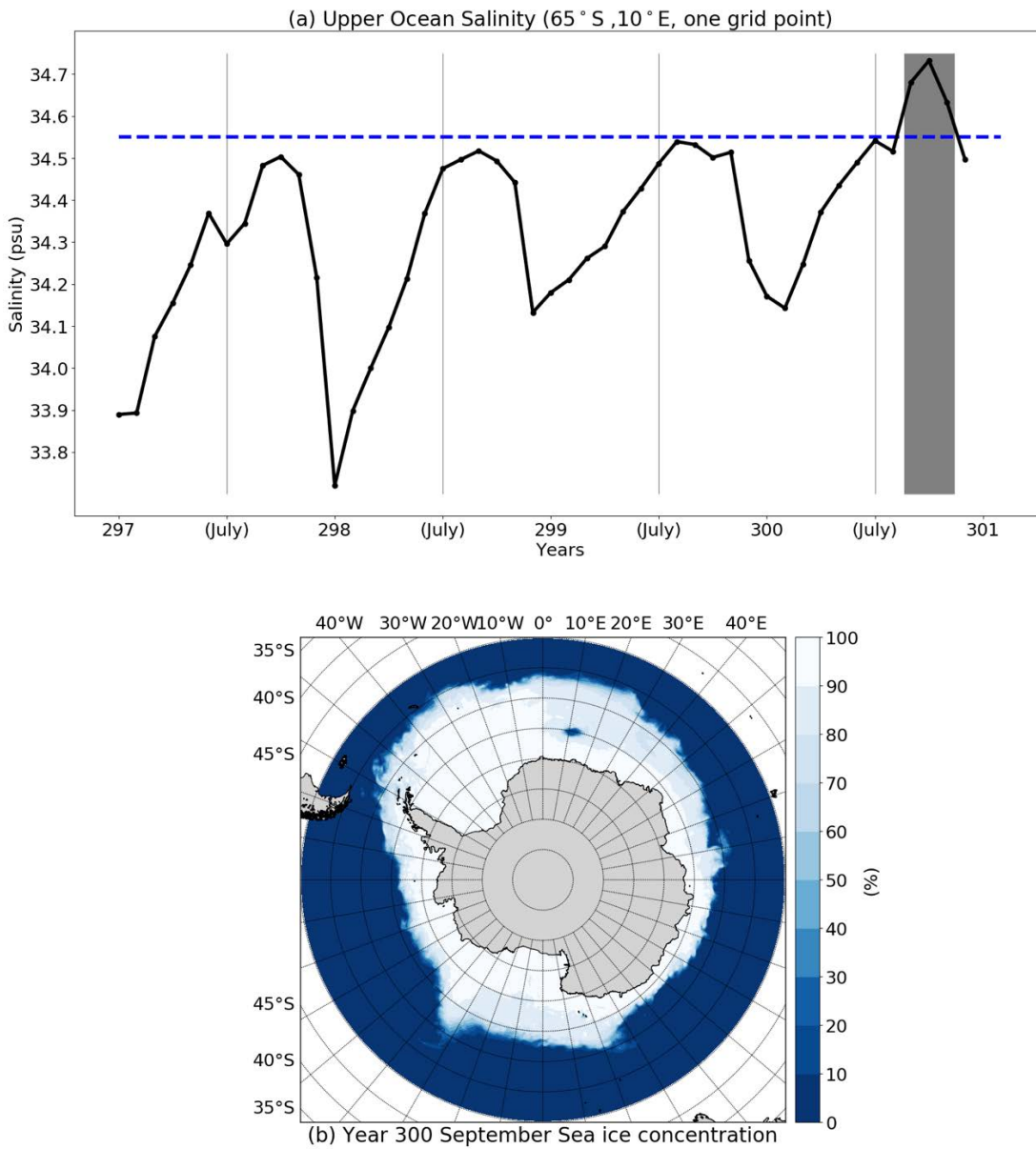


Figure 3.5. (a) Simulated monthly-mean upper-ocean salinity (top 10m) at the model grid point where the MRP of simulation year 300 is triggered. The dashed blue line represents the critical salinity value for triggering the MRP. The grey shaded area indicates the time of MRP occurrence. (b) Simulated September-mean Sea ice concentration indicating the location of the MRP of simulation year 300.

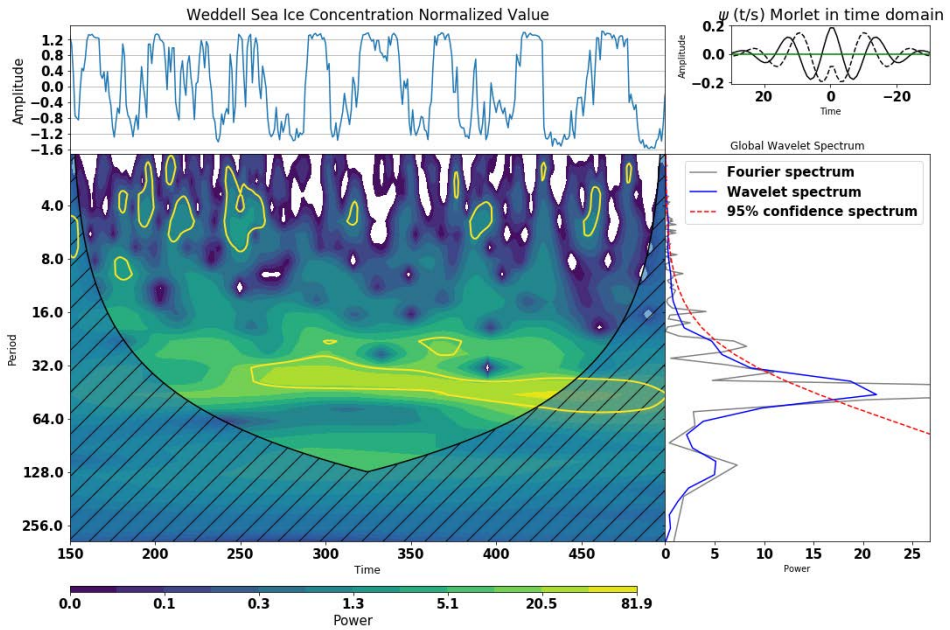


Figure 3.6. Wavelet spectrum of sea ice concentration time series in MRP region. The yellow lines represent the 95% significance contour (Mabel Costa, personal communication., 2021). The shaded area is the cone-of-influence; anything in the shaded area is not trustworthy.

3.4. Transition from no-polynya to polynya phase

It is ultimately the vertical density distribution that determines convective instability, which in turn controls the occurrence of polynyas. By plotting upper-ocean temperature and upper-ocean salinity in a T-S diagram (following Martin et al., 2013), we can examine which variable is more important in determining the upper-ocean density. Here, we pursue this for the seasonal and interannual change of upper-ocean temperature and salinity in the MRP region following the transition from a no-polynya to a polynya phase during model years 292–310 (Figure 3.7a). Each “year” starts in September, and the individual years are distinguished by different colors as indicated in the inset. The first 8 years represent the no-polynya phase (from September of model

year 292 to August of model year 299), and the 8-year average of each month is displayed by the dashed line marked with filled triangles, black for the first 4 months (September through December), and purple for the last 8 months (January through August). Year 300–302 is the transition period. The last 8 years represent the polynya phase, with the average being represented the same way as the no-polynya phase but marked with filled squares. During the no-polynya phase, the seasonal density change is dominated by salinity rather than temperature change, indicating that this phase is mostly associated with freezing and melting of sea ice (as discussed in Section 3.1). During the polynya phase, the seasonal density change is dominated by temperature changes, which indicates that freezing and melting are hardly involved. Furthermore, the winter (September) upper-ocean temperature (filled circles) is above the freezing point (denoted by the purple dashed line in the figure) during the polynya phase, which supports the notion that convection renders the upper ocean too warm for sea ice to form. Figure 3.7b shows only the sequence of the September points. From year 292–299, the salinity is increasing slowly while the temperature remains near the freezing point. In September of year 299, upper-ocean density reaches the highest value before convection commences in year 300. Thus, the change of density due to salinity plays a more dominant role in the polynya triggering process than that due to temperature, as expected in upper-ocean seawater that is near its freezing point.

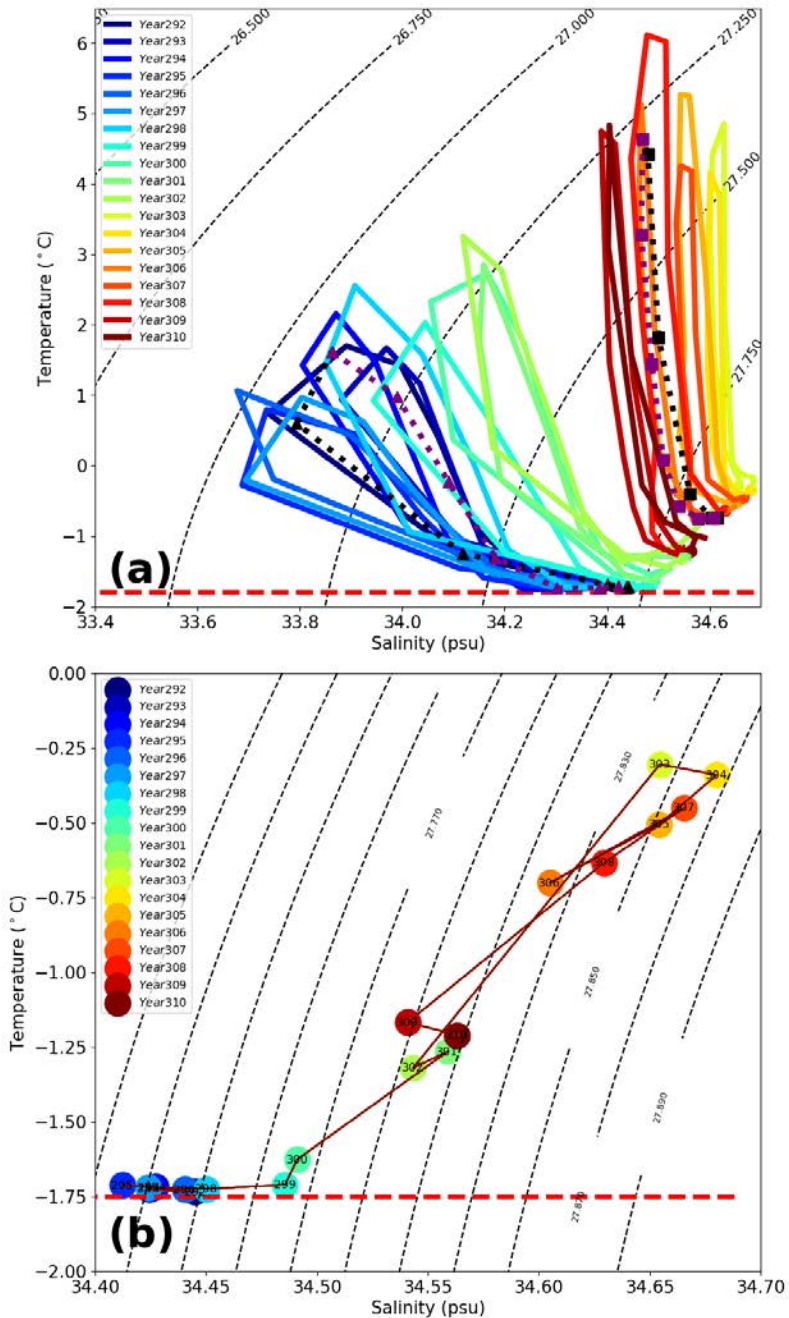


Figure 3.7. (a) T-S diagram of monthly-mean upper-ocean properties averaged over the MRP region showing seasonal and interannual changes during the transition from no-polynya to MRP mode in simulation years 292 to 310. The dots denote September properties. (b) Same as (a), but for September data only. See text for a more detailed explanation. The MRP is triggered in year 300.

3.5. Variables correlating with polynyas and possible polynya feedbacks

The next question is why the upper-ocean salinity slowly increases many years before a polynya is triggered (Figure 3.5a). Gordon et al. (2007) proposed a possible link between the SAM and WSP formation based on historical observation datasets: during a positive SAM phase, the upper-ocean salinity in the Weddell Sea decreases due to an increase of precipitation, leading to a more stable surface layer, while during a negative SAM phase, the surface layer gets saltier due to overall drier conditions, making the ocean more susceptible to vertical exchange and polynya formation. The observations referred to in de Lavergne et al. (2014) show that surface freshening of the polar Southern Ocean has enhanced its stratification due to a more positive SAM phase in recent decades. Martin et al. (2013) pointed out that precipitation plays a dominant role in the polynya closing process in their 5,000-year-long low-resolution coupled Kiel Climate Model simulations, though they find the deep heat reservoir is more important to the polynya triggering process in that model. Besides changes of the freshwater flux due to precipitation, thermodynamic sea-ice growth and decay can also lead to long-term changes of the upper-ocean salinity due to the net brine rejection effect (Haumann et al., 2016). Based on these previous works, we will next explore how these freshwater fluxes may influence the upper-ocean salinity, ultimately determining the polynya phases in the 500-year-long high-resolution CESM simulation analyzed in this study. Before moving on we note that, in nature, the observed long-term change toward a more positive SAM index is mostly due to stratospheric ozone depletion and atmospheric carbon dioxide concentration increase (Banerjee et al., 2020). In our preindustrial control simulation,

these two factors are fixed at year 1850 conditions. The periodic change of the SAM index in our simulation (and to a certain degree in modern observations) thus involves other dynamical processes.

When comparing evaporation over the open ocean with that over sea ice (Figure 3.8b), an obvious and well-known feature is that the evaporation over the polynya region is much larger compared to that over the ice-covered region (Figure 3.8c). When polynyas occur, a vast amount of heat and moisture is released into the atmosphere; large polynyas thus exert a considerable influence on the atmosphere, for example, on sea level pressure and precipitation (see also Weijer et al., 2017). To investigate Gordon et al.'s (2007) hypothesis on the possible role of a meridional shift of the precipitation-rich westerlies (Figure 3.8a), we analyzed 5-year running mean timeseries of the total precipitation (rain and snow, Figure 3.9a) averaged over the yellow box area shown in Figure 3.2. Figure 3.9b is based on a composite analysis showing the spatial difference of precipitation between WSP-phases (dark gray in Figure 3.9a) and no-WSP-phases (white in Figure 3.9a). During WSP phases, there is clearly more precipitation over the polar Southern Ocean near Antarctica (red), and less precipitation further north (blue). Though superimposed by the effect of polynyas on precipitation, this provides some evidence for a meridional shift of the precipitation-rich westerlies. While the numbers outside the immediate effect of polynyas in Figure 3.9b reveal that the precipitation changes in this preindustrial control simulation are small (about 0.3 mm/day or 9 mm/month), they are apparently in the range of observed precipitation changes in association with the SAM index (below 10 mm/month according to Spensberger et al.,

2020). More pronounced shifts and clearer functional relationships with SAM occur in a transient anthropogenic climate change simulation with the same CESM as used in this study; these will be discussed in a separate paper.

As mentioned above, besides precipitation, another factor that contributes to long-term changes of the upper-ocean salinity is the freshwater flux due to sea ice growth and melt. The timeseries in Figure 3.10a shows the net value of the contribution of negative freshwater flux from brine rejection during ice freezing, and of positive freshwater flux from ice melting in the wider WSP region (black box). In polynya years, there is more melting than freezing, thus adding freshwater to the ocean surface, while in no-polynya years, the negative freshwater flux due to brine rejection mostly exceeds that due to melt, leading to an increase of upper-ocean salinity. The spatial distribution of this cumulative effect is shown for the composite of WSP years (Figure 3.10b) and the composite of no-WSP years (Figure 3.10c). During WSP years, the freshwater flux reveals net melting in the central Weddell Sea region (Figure 3.10b), which would make the upper ocean gradually fresher over time. During the no-WSP years, the effect of net brine rejection dominates (Figure 3.10c), thus rendering the upper ocean saltier. Thus, sea ice will not only induce seasonal fluctuations of upper-ocean salinity, but can also induce interannual trends of upper-ocean salinity as shown in Figure 3.5a. Although the effect of the shift of the high precipitation westerlies and that of net brine rejection due to sea ice change/drift are roughly in phase and thus superimposed in time, their regions of influence may not coincide, as seen in Figures 3.9b and 3.10b.

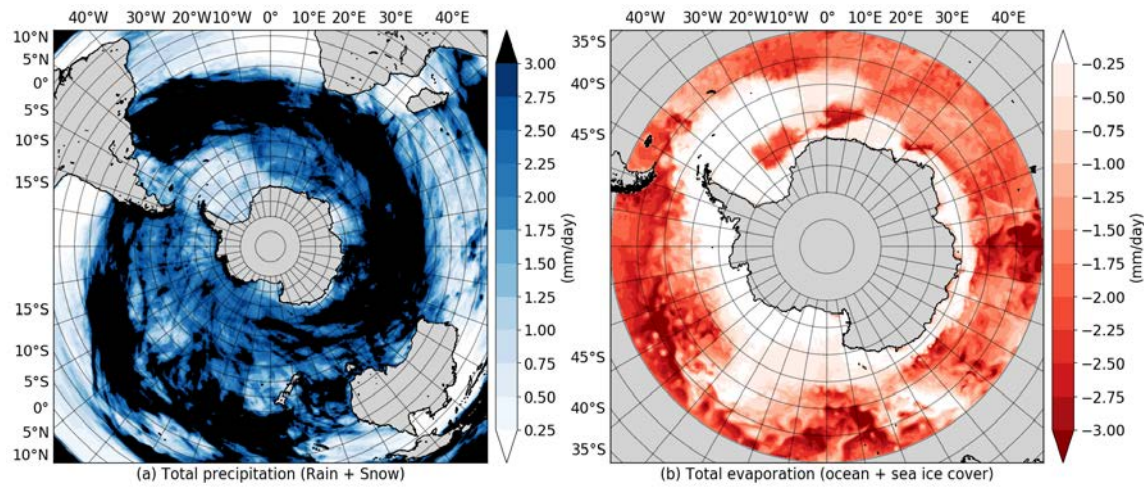


Figure 3.8. (a) Total precipitation from atmosphere (rain + snow). (b) Total evaporation over both ocean and sea ice cover. Graphics represent September-mean values of model year 270.

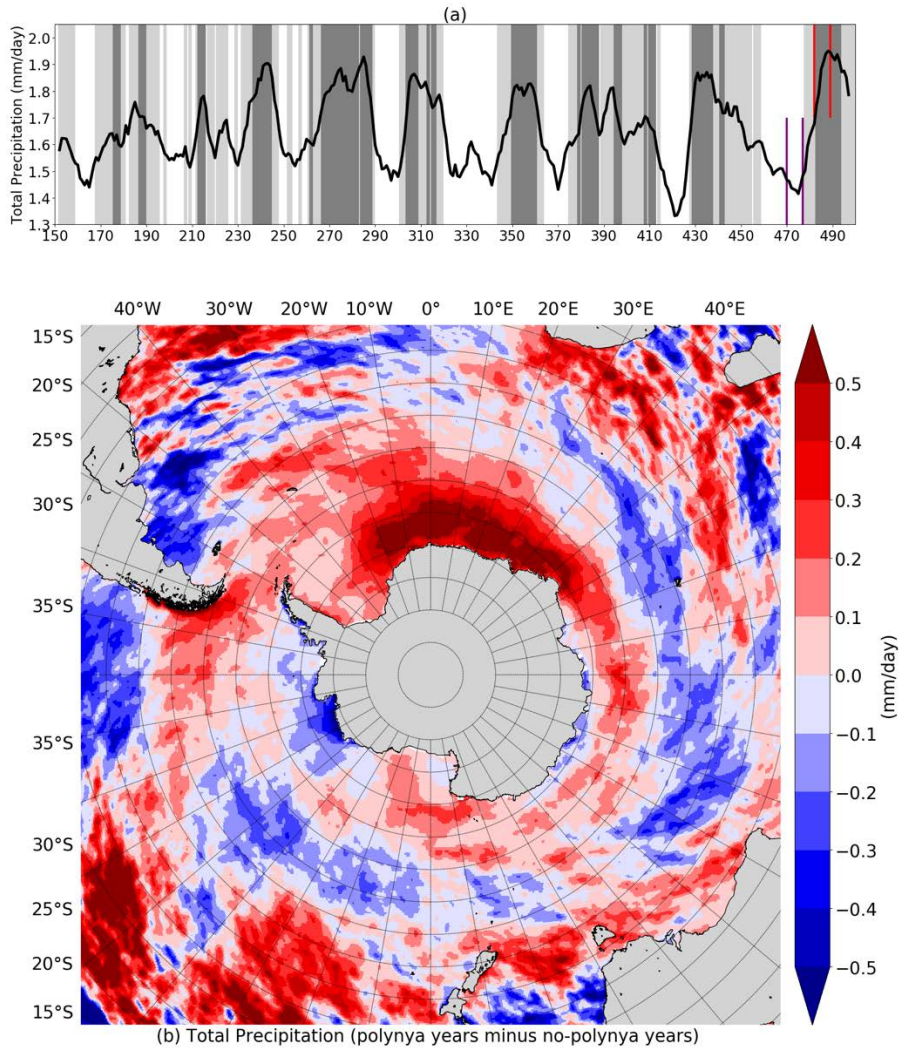


Figure 3.9. (a) 5-year running mean timeseries of total precipitation averaged over the black box area in Fig.2. The shading reflects MRP years (light grey), and WSP years (dark grey), matching with Fig. 4. **(b)** Eight-year- mean total precipitation difference of typical polynya years (years 482-489 mean, between the red lines in (a) when precipitation in chosen polynya period is maximum) minus typical no-polynya years (years 470-477 mean, between the purple lines in (a) when precipitation in chosen no-polynya period is minimum).

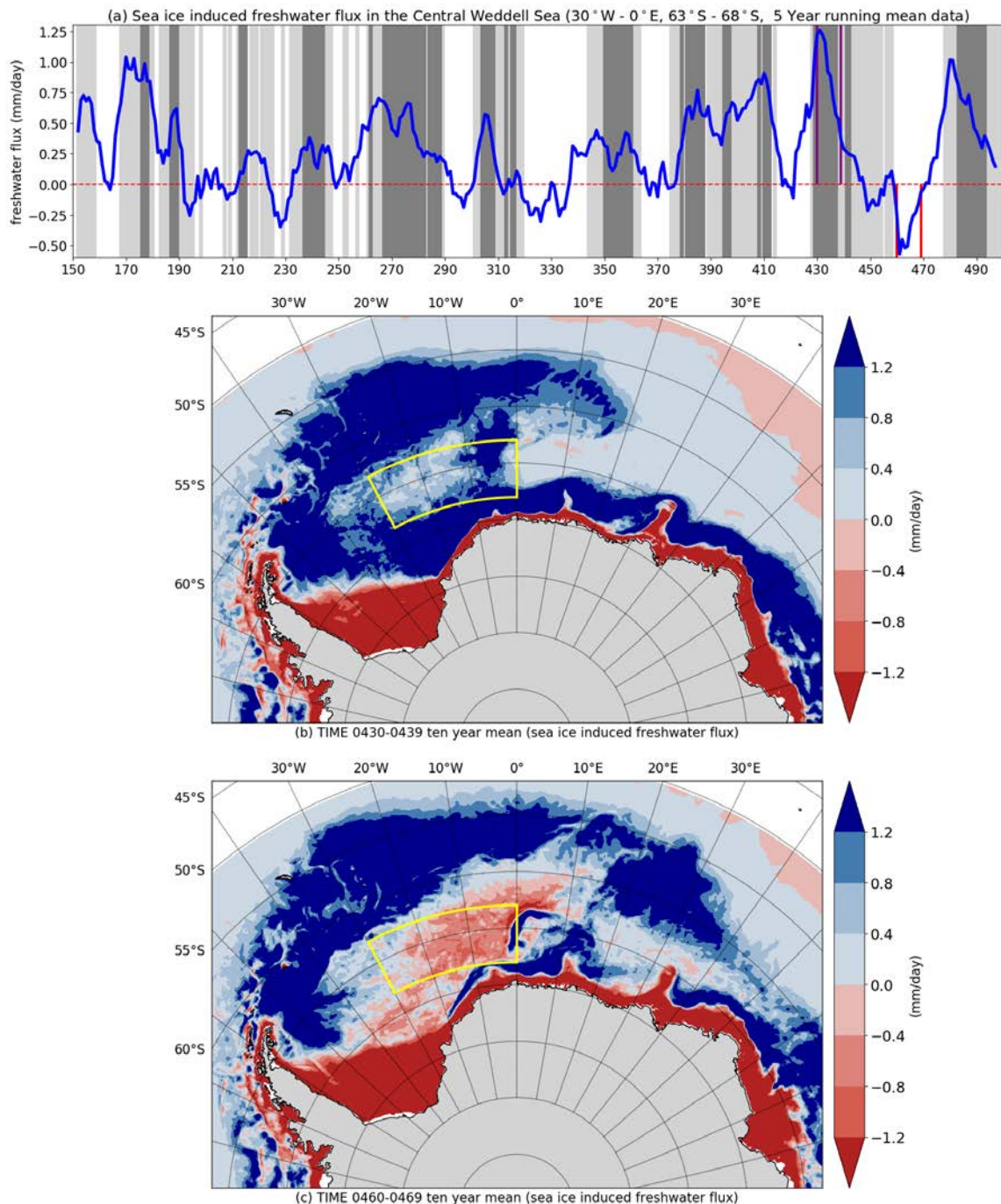


Figure 3.10. (a) 5-year running mean timeseries of annual net sea-ice growth and melt induced freshwater flux in central Weddell Sea (yellow box). (b) Annual net sea-ice induced freshwater flux in polynya period (year 430-439 mean, between purple lines in (a) when freshwater flux in chosen polynya period is maximum). (c) Same as (b) but in no-polynya period (year 460-469 mean, between red lines in (a) when freshwater flux in chosen no-polynya period is minimum).

Recalling that the occurrence of polynyas is often attributed to the change of the SAM index (Campbell et al., 2019; Cheon et al., 2014; Gordon et al., 2007), and to emphasize the role WSPs play in modifying the atmospheric circulation, we introduce a regional SAM-like index that only spans the longitudinal band of the Weddell Sea region. This index is similar to the SAM index, except that it is based on the standardized sea-level pressure difference between 40°S and 65°S over the region 40°W–30°E; it is here referred to as the Regional Meridional Pressure Difference index ($\text{RMPD} = P_{40}^* - P_{65}^*$, where P^* represents the standardized sea-level pressure). To determine the main reasons for the variation of the RMPD index in our simulation, we first checked the standardized sea-level pressure at 40°S and 65°S, respectively. The results show that the latter dominates the variation of the RMDP index, with a high negative correlation (Figure 3.11a vs. Figure 3.11b, $r = -0.88$). At the same time, sea-level pressure at 65°S varies predominantly with the occurrence of WSPs (dark gray shadings in Figure 3.11). This indicates a direct impact of WSPs on the local sea-level pressure, and thus the RMPD index, which in turn is a measure of the state of the larger scale atmospheric circulation. The RMPD index, in turn, is negatively correlated with the wind stress curl anomaly averaged over the wider Weddell Sea region (40°W–30°E, 70°–55°S; Figure 3.11c; $r = -0.73$). The variations of the wind stress curl seem to be associated with a meridional shift of the precipitation-rich westerlies, as indicated by corresponding variations of total precipitation over the yellow box region in Figure 3.2 (Figure 3.11d; $r = -0.70$). Note, however, that because more evaporation over polynyas leads to more precipitation, the variation of precipitation over the polynya regions is

dominated by polynya occurrence. There is nevertheless weak evidence that the latitude of the core of the westerlies varies accordingly. Figure 3.11e shows that the Weddell Gyre circulation varies largely in concert with the wind stress curl ($r = -0.48$). Finally, the variability of the upper-ocean salinity is well correlated with precipitation and the Weddell Gyre strength (Figure 3.11f; $r = +0.85$ and $r = +0.63$, respectively). In addition to the respective correlations, Table 1 also shows at what lead/lag the correlations are highest. Accordingly, upper-ocean salinity leads precipitation by 1 year. While a positive correlation between precipitation and upper-ocean salinity is counterintuitive, this lag in precipitation indicates that the increase/decrease in precipitation is driven by the opening/closing of polynyas (due to more evaporation over polynyas as explained earlier), recalling that the occurrence of polynyas is always associated with high upper-ocean salinity (due to convection).

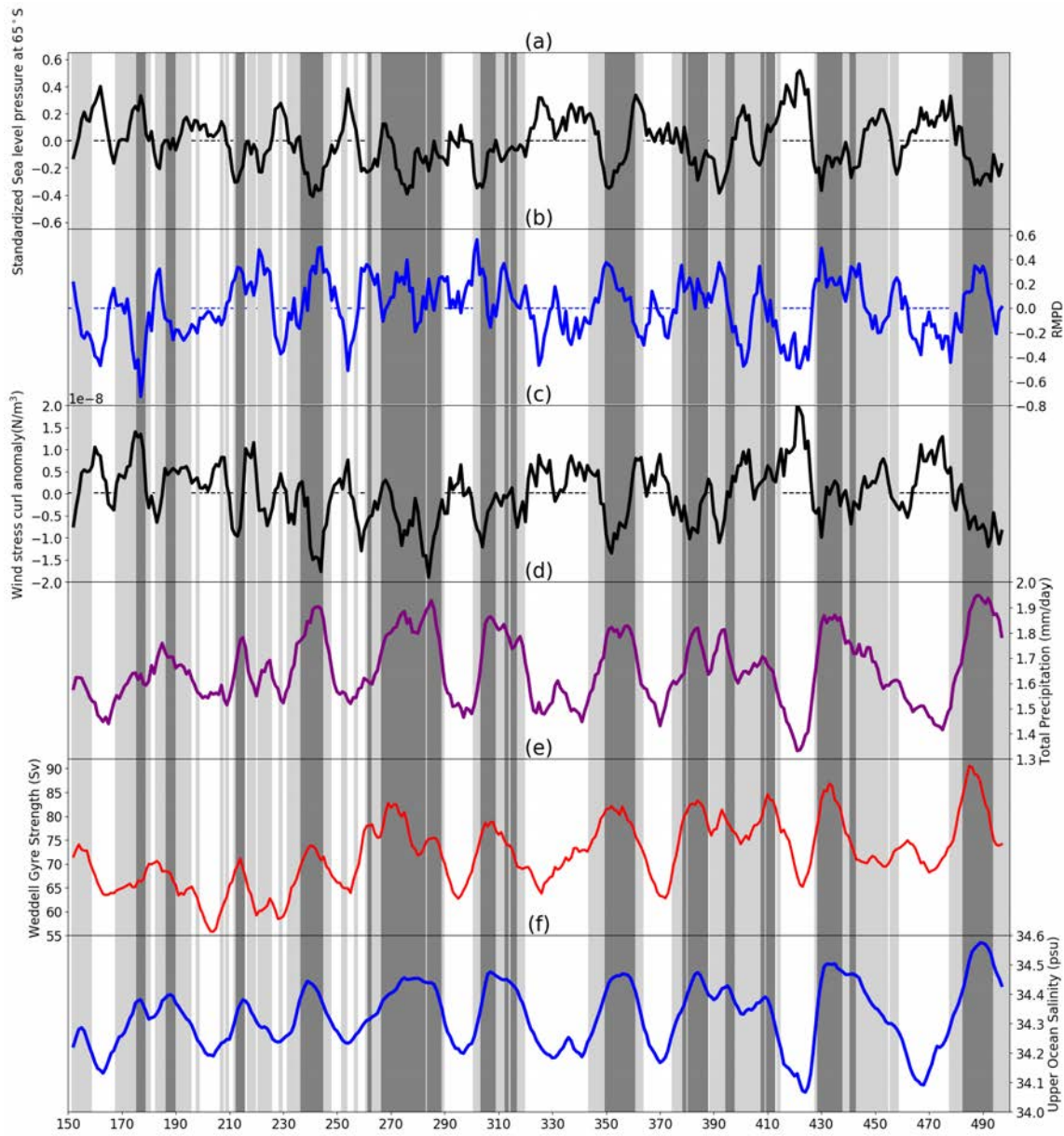


Figure 3.11. Timeseries of 5-year running means of (a) Standardized sea-level pressure at 65°S in the region of 40°W-30°E. (b) The Regional Meridional Pressure Difference (RMPD) index, a SAM-like index, but only calculated in the region of 40°W-30°E. (c) Wind stress curl anomaly averaged over the wider Weddell Sea region (40°W-30°E, 70°S-55°S). (d) Net precipitation averaged over black box in Fig.2. (e) Weddell gyre strength (measured as the westward transport across the prime meridian). (f) Upper ocean salinity (top 10m) averaged over black box in Fig.2.

Table 1, Pearson linear coefficients (r) in Fig.11 (after linear detrending).

	1	2	3	4	5	6
1 SLP at 65°S	1.00	-0.88 (0)	0.83 (0)	-0.72 (-1)	-0.49 (0)	0.61 (-1)
2 RMPD		1.00	-0.73 (0)	0.57 (-1)	0.41 (0)	0.51 (-1)
3 Wind stress curl			1.00	-0.70 (-1)	-0.48 (-1)	-0.50 (-1)
4 Total precipitation				1.00	0.68 (+1)	0.85 (+1)
5 Weddell gyre strength					1.00	0.63 (0)
6 Upper ocean salinity						1.00

*The listed values are within ± 5 years lag at which the absolute value of the correlation is maximal (shown in brackets). Positive values indicate that the index on the top axis leads, while the index on the vertical axis lags.

Based on the above results, we propose a possible coupled ocean-atmosphere mechanism to explain how periodic RMPD index changes influence the periodic occurrence of WSPs, and vice versa (see schematic in Figure 3.12). The sequence of events is summarized in the following: when there are no WSPs, the sea level pressure at 65°S is relatively high (positive anomaly) so that the RMPD index is negative; this pressure difference is commensurate with a relatively northern position of the westerly wind belt and a more positive wind stress curl anomaly (less cyclonic). In this state, two effects tend to slowly increase the upper-ocean salinity, namely the overall drier

conditions (less precipitation) and the negative freshwater flux anomaly due to more freezing than melting (Figure 3.10c). After several years under these conditions, the cumulative effect of these 2 processes will make the upper ocean salty enough for the stratification to weaken to the point that deep convection is initiated. This will melt the winter ice pack, thus leading to the formation of a polynya. More specifically, when the upper-ocean salinity is high, convection will commence and be most vigorous in the topographically preconditioned region of the Maud Rise seamount. The associated entrainment of warm and salty WDW into the mixed layer will first produce an MRP and will further increase the upper-ocean salinity. If this convection-induced increase of upper-ocean salinity is particularly high, a WSP develops as an MRP expands westward. When a WSP emerges, the sea level pressure above the WSP will decrease (negative anomaly) because of the much warmer surface condition in the absence of sea ice. This initiates the opposite phase of the proposed circuit in Figure 3.12, that is, the RMDP index will become positive and the wind stress curl more cyclonic. As a result of this, the Weddell Gyre will strengthen and act as a positive feedback in that it leads to a more pronounced doming of isopycnals in its center. This reinforces deep convection in the central Weddell Sea which is necessary to sustain WSPs for several years until the deep heat and salt reservoir is exhausted; see also Cheon et al. (2014), Martin et al. (2013) and Dufour et al. (2017). After several years of WSP occurrence, the upper-ocean salinity in the Weddell Sea will gradually decrease, again for two reasons: first, because the precipitation-rich westerly wind belt moved southward (in concert with the more cyclonic wind stress curl), leading to more precipitation; and second, because of a higher

freshwater flux due to more melting than freezing in the central Weddell Sea region (Figure 3.10b). The combined effects will finally make the WSP disappear. This will increase the sea level pressure (positive anomaly) over the former WSP region again and closes the proposed coupled ocean-atmosphere “circle”.

While similar to what has been proposed in earlier studies on this topic (Campbell et al., 2019; Cheon et al., 2014; Kurtakoti et al., 2018), the decisive difference in our proposed sequence of events is that WSPs play an active role in modifying the regional atmospheric circulation eventually setting up conditions that lead to the closure of WSPs, and vice versa, at least in this simulation. Chang et al. (2020) showed that WSPs in this simulation seem to be leading remote teleconnections all the way to the tropical Pacific. Furthermore, Kaufman et al. (2020), using the Granger causality method (Granger, 1969), showed that polynyas have the capability to both drive and respond to the atmospheric variability over the Weddell Sea in high-resolution ESM simulations, which supports our proposed coupled ocean-atmosphere mechanism. Another recent study is that of Gnanadesikan et al. (2020), who propose a “coupled oscillator mechanism” to explain interdecadal variability of Southern Ocean convection with a rather complicated feedback loop (their Figure 3.11a). While pursuing a thorough principal oscillation pattern (Hasselmann, 1988) analysis, the spatial resolution of their underlying ESM simulation is about one order of magnitude lower in both principal horizontal directions than the ESM simulation analyzed here. While we do not question the validity of their analysis, their model is missing details that are critical for open-ocean polynya formation, in particular the formation of MRPs.

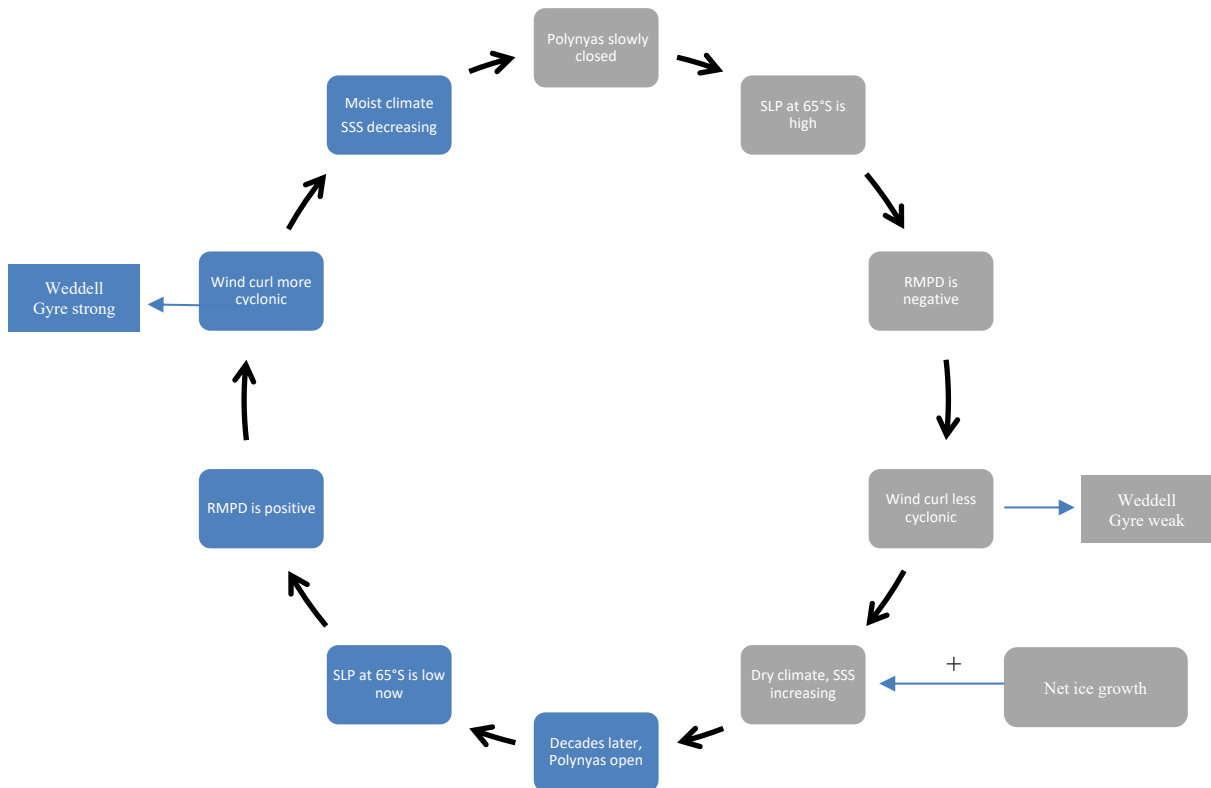


Figure 3.12. Conceptual circuit of sequence of processes involved in our proposed coupled ocean-atmosphere mechanism.

Due to very limited observations, the causes for the observed open-ocean polynyas are still unclear and under debate. Based on previous studies (de Lavergne et al., 2014; Gordon et al., 2007; Haumann et al., 2016), we provided two possible explanations for why the upper-ocean salinity increases before a WSP occurs, and decreases before it disappears, respectively. Cheon and Gordon (2019) pointed out that when the SAM index becomes more positive, the effect of the associated more cyclonic wind stress curl and the southward shift of the high-precipitation westerlies are

competing with each other when it comes to WSP formation. The prolonged negative SAM index phase has been hypothesized to lead to drier conditions, which could have preconditioned the WSP formation in 1974–1976 (Gordon et al., 2007). On the other hand, the 2016–2017 MRPs event seems to have been triggered by a more cyclonic wind stress curl (Campbell et al., 2019). More direct observations and future research are still needed to further test our proposed coupled ocean-atmosphere mechanism.

3.6. The role of topographic preconditioning the polynya formation

We next investigate the local mechanisms that result in the polynyas being triggered first in the Maud Rise and Astrid Ridge region. Maud Rise is a seamount with a 1,700 m peak near 65°S, 2°E. Astrid Ridge is a series of lower seamounts extending along about 66°S, and between about 11°E and 17°E (Figure 3.2 and Figure 3.13). A number of observational studies identified a crescent of low sea ice concentration along the north-western flank of Maud Rise (Comiso & Gordon, 1987; De Vaux et al., 1993; Lindsay et al., 2004). This crescent reflects the existence of a Taylor column circulation over the seamount or other topographically induced flow (Lindsay et al., 2004). Kurtakoti et al. (2018) showed that a high-resolution ESM can indeed simulate the Taylor column effect above Maud Rise realistically enough to precondition this region for MRPs to emerge. In our simulation, the permanent features of the Taylor column, in terms of mixed-layer depth and WDW-layer temperature and salinity (Figure 3.13) as well as the zonal flow and relative vorticity of sea ice velocity around Maud Rise and Astrid Ridge (Figure 3.14), are consistent with Kurtakoti et al. (2018), which enhances

the fidelity of our global ESM simulation through capturing critical local processes.

Overall, the stratification over and around Maud Rise is relatively weak, even in no-polynya years.

Figure 3.15b shows September sea-ice concentration averaged over a 10-year no-polynya period (model year 460–469). The crescent of slightly lower sea ice concentration along the northwestern flank of Maud Rise matches well with corresponding results derived from satellite remote sensing (Lindsay et al., 2004). The fact that the crescent of lower ice concentration coincides with that of a positive freshwater flux due to more local ice melt than freezing indicates a permanent upwelling of warmer water in this region (Akitomo, 2006). On the other hand, the narrow outer crescent of negative freshwater flux due to more freezing than melting (Figure 3.15a) suggests that this outer region is beyond the influence of the Taylor column circulation and is consistent with the narrow crescent of higher ice concentration (Figure 3.15b).

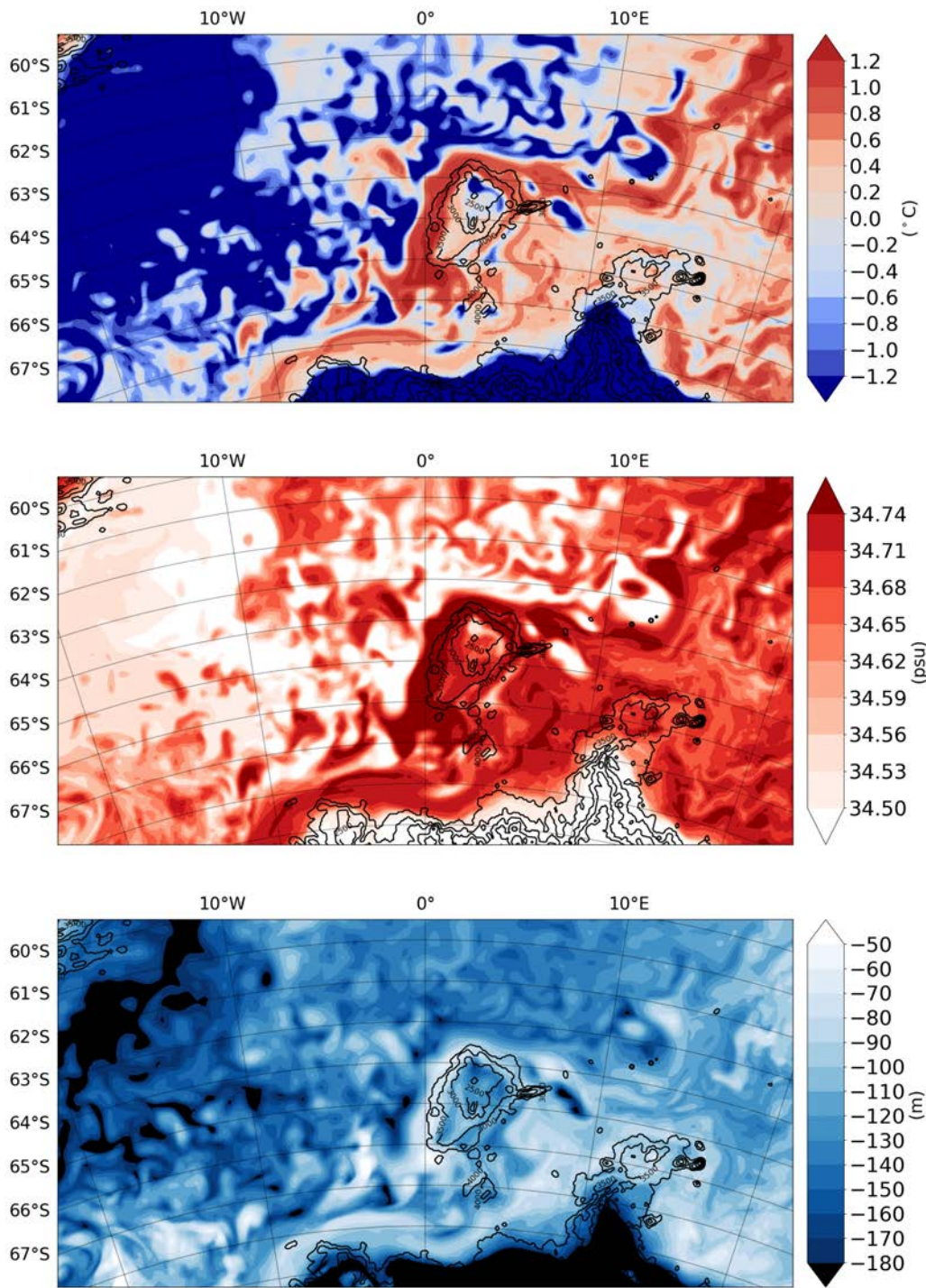


Figure 3.13. (a) September temperature at 305 m depth of simulation year 299. **(b)** Same as (a) but for salinity. **(c)** Same as (a) but for mixed-layer depth. Black contours indicate depth.

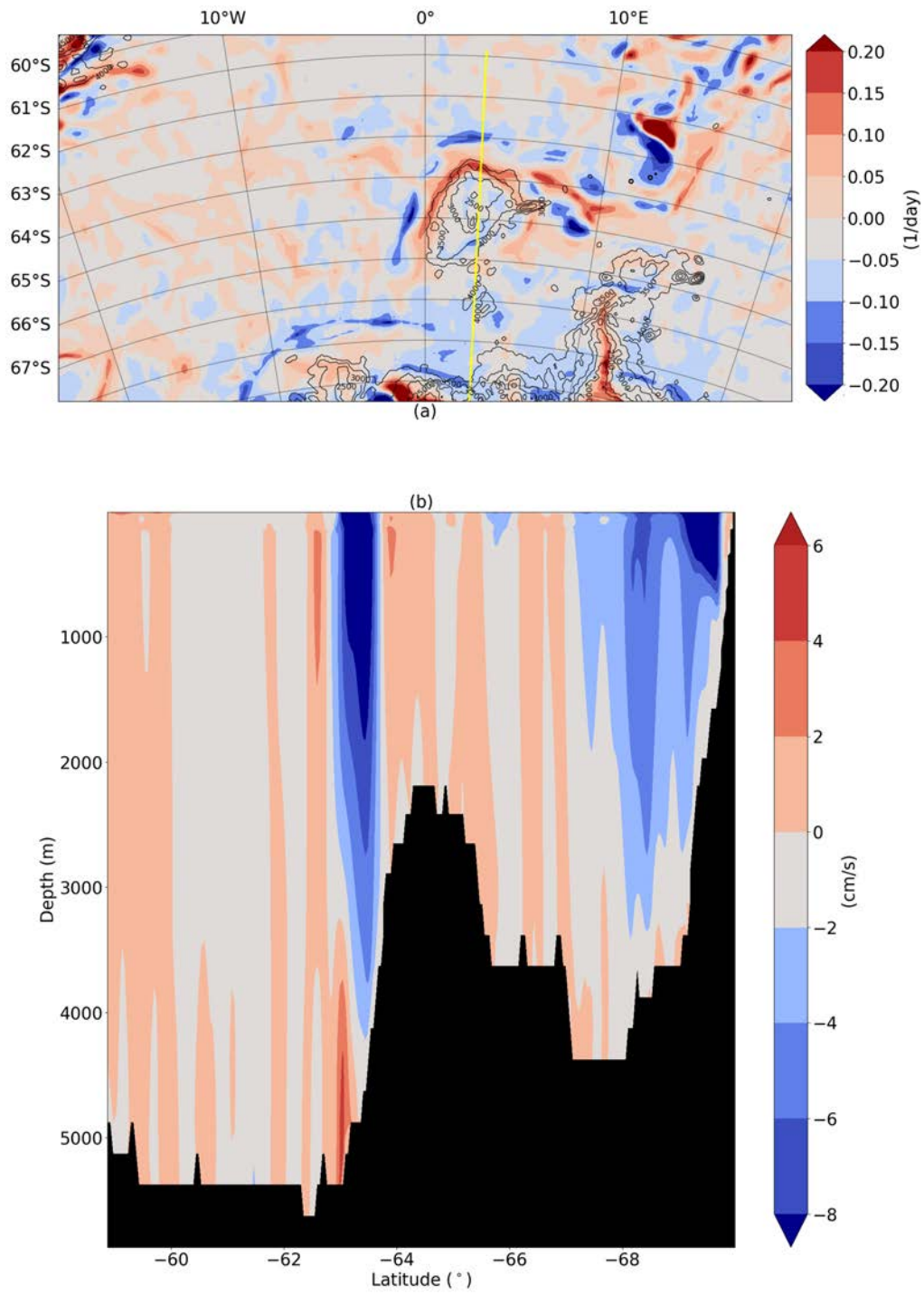


Figure 3.14. (a) September sea ice vorticity field in simulation year 299, black contours indicate depth contours. **(b)** zonal velocity across section 3°E (the yellow line in (a)).

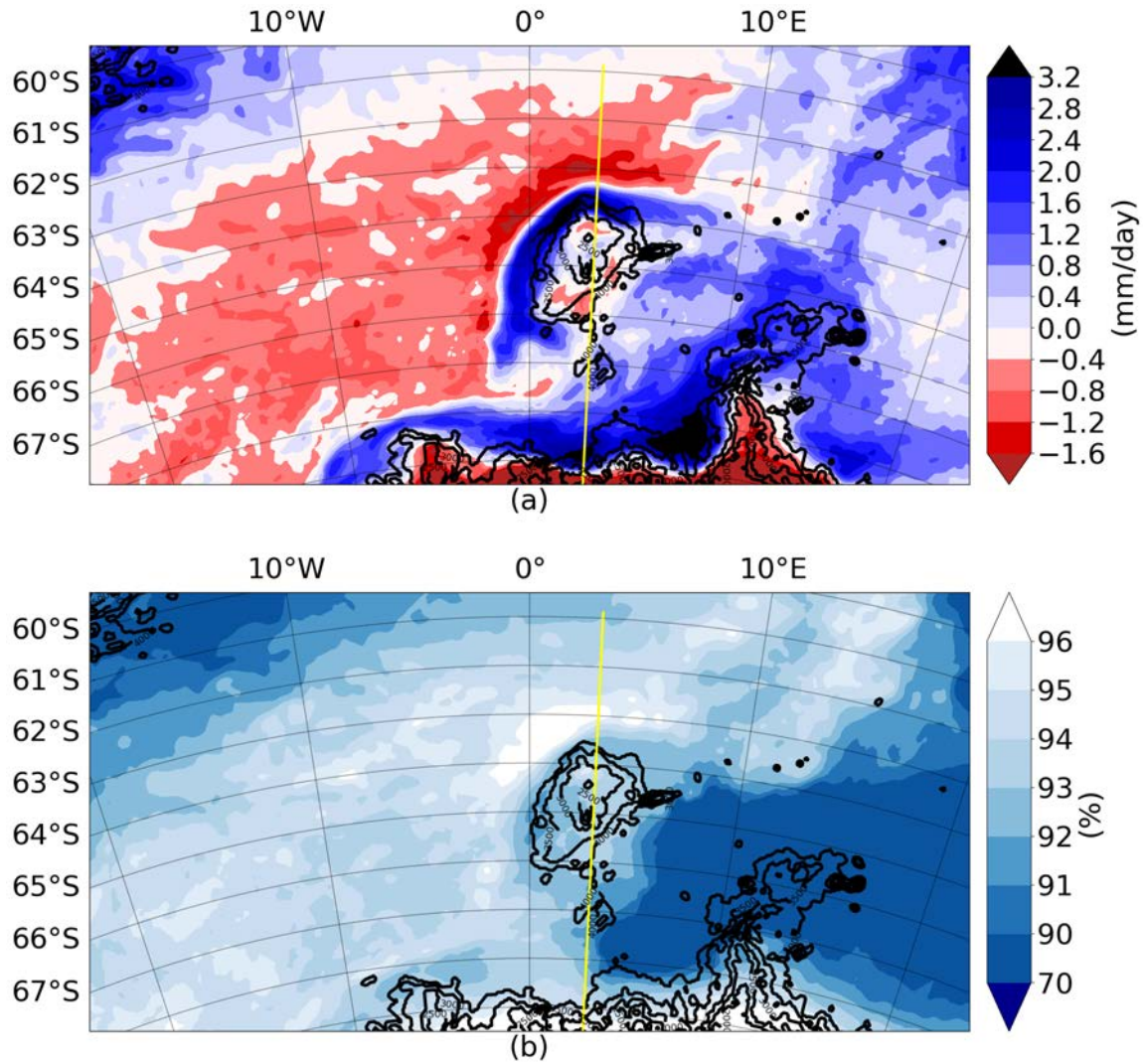


Figure 3.15. (a) Enlargement of Fig.10c with focus and bathymetry around the Maud Rise seamount and the Astrid Ridge. **(b)** Year 460–469 mean September sea-ice concentration. Black contours stand for depth. Yellow line represents the section that cross the top of Maud Rise seamount.

3.7. On the role of the deep heat reservoir

While some studies argue for the importance of the build-up of a heat reservoir at depth for triggering WSPs (e.g., Dufour et al., 2017; Martin et al., 2013), our results are more in line with the findings of Gordon et al. (2007), Kurtakoti et al. (2018) and

Campbell et al. (2019) in that the heat reservoir at depth is not the immediate cause for the occurrence of WSPs. However, once warmer and saltier water makes it to the surface as a result of convection, it plays an important role in maintaining deep-penetrating convection and polynyas. In our multi-century simulation, the large amount of heat and salt reaching the surface through convection often leads to much larger WSPs than those observed in the 1970s, in particular ice embayment, that is, large ice-free areas in winter that are not entirely surrounded by sea ice.

We demonstrate the development of heat and salt accumulation at depth through time series of September depth profiles of salinity, temperature, and water age (Figures 3.16a–3.16c). Consistent with the long-term upward trend of gyre strength (Figure 3.11e), there is also an upward trend of both salinity and temperature at the depth range of the WDW layer (300–700 m), only interrupted by colder and fresher periods during polynya years. The water age tracer (Figure 3.16c), which reveals the time that has passed since a water parcel has last been in contact with the atmosphere, shows rapid aging after polynya periods. This indicates that the warmer and saltier water is being advected into the region from further upstream rather than aging locally.

Model drift of deep ocean properties is a common phenomenon in ocean-only and coupled simulations; a similarly increasing trend of WDW has been reported by Zhang et al. (2021) based on a 3,000-year-long low-resolution ESM simulation. Note that Martin et al. (2013) discarded the first 800 years of their 3,000-year-long low-resolution ESM simulation to reduce the effects of model spin-up. Deep-ocean model drift is also to be expected in high-resolution ESM simulations, as also reported on by

van Westen and Dijkstra (2020). Considering the unprecedented length of our high-resolution simulation (Chang et al., 2020), this is in fact the first time that the effects of such model drift can be investigated in the framework of a high-resolution ESM. A notable feature here is that the model drift at depth does not noticeably affect the frequency of polynya formation events. Comparing the time series of upper-ocean density with that of potential density at a depth of 250 m (the upper extent of the WDW layer) in the central Weddell Sea (Figure 3.16d), we find that while the WDW undergoes large changes in temperature (T) and salinity (S) with polynya on and off phases (Figures 3.16a and 3.16b), the effects of T and of S on density in this layer seem to mostly compensate each other such that density fluctuations amount to only some 0.01 kg/m³ in that layer (consistent with Figure 2c in Gordon et al., 2007). In the upper ocean (red line in Figure 3.16d), however, density fluctuations are much larger (up to 0.2 kg/m³), and solely due to changes of salinity (Figure 3.16e). This reaffirms our point that the polynya events are mainly a surface-controlled phenomenon. On the other hand, the upper ocean stratification in the Weddell Sea exhibits substantially larger fluctuations after year 400 (Figure 3.16d) that are solely due to fluctuations of upper-ocean density (in particular salinity). This may eventually affect the frequency of polynya occurrence, as indicated in the wavelet spectrum in Figure 3.6 in that the period apparently increases after year 400.

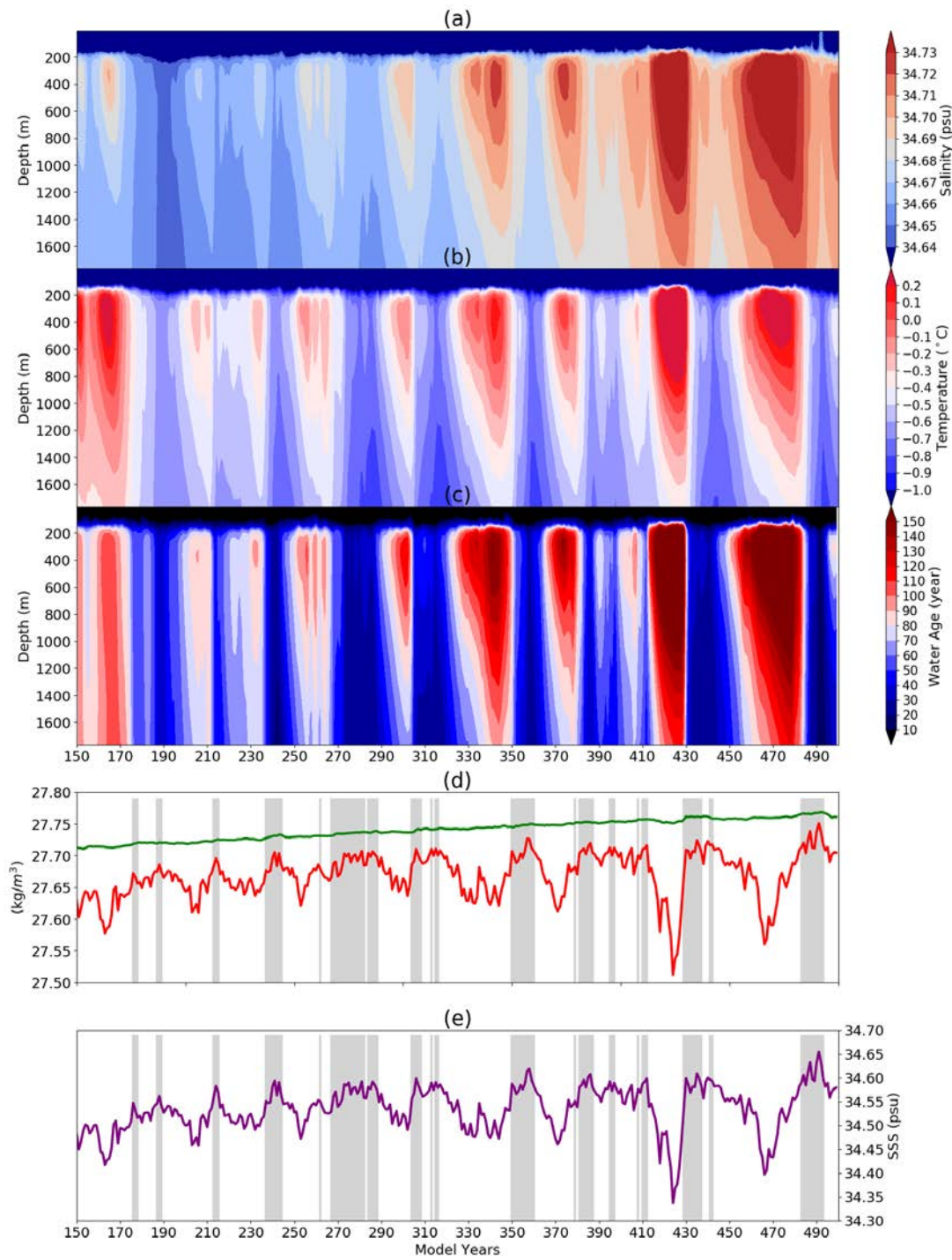


Figure 3.16. Time series of depth profiles of (a) temperature, (b) salinity, (c) water age, (d) water density at upper ocean (red) and at 250m (green), and (e) upper-ocean salinity, all averaged over the central Weddell Sea (61.3°S - 70°S , 40°W - 10°W). Grey areas represent the WSP periods.

3.8. Summary and conclusions

A new 500-year-long high-resolution simulation run under preindustrial radiative conditions produces polynyas in the Weddell Sea that recur periodically with a multidecadal time scale of 40–50 years. This comprehensive simulation resolves processes that are critical for polynya formation. Our study leads to the following conclusions:

- (1) The multi-decadal cumulative increase of upper-ocean salinity in the Weddell Sea, superimposed on the seasonal contribution due to brine rejection, is the main cause for the initiation of polynyas in this simulation.
- (2) Two possible factors may drive the periodic change of upper-ocean salinity: the periodic change of total precipitation over the Weddell Sea and the periodic change of the regional freshwater flux due to sea ice growth and decay.
- (3) We propose a new possible coupled ocean-atmosphere mechanism in which WSPs first reduce the surface air pressure, causing a regional SAM-like index to become more positive. This moves the precipitation-rich westerlies southward and leads to more sea ice melt in the central Weddell Sea, which in turn stabilizes the water column over time such that WSPs close again. As a result, the air pressure over the Weddell Sea increases, rendering the regional SAM-like index more negative. This forces the westerlies to move northward and stimulates thermodynamic ice growth in the central Weddell Sea. These two factors will gradually increase the upper-ocean salinity to the point that WSPs re-emerge.

(4) The persistent Taylor cap effect, which is well represented by the high-resolution topography of Maud Rise and Astrid Ridge, preconditions these regions with a weaker stratification; polynyas thus occur first at these two locations in the model.

(5) Density-compensated model drift in the WDW layer does not noticeably affect the frequency of polynya occurrence, which reaffirms that the polynya events are mainly a surface-controlled phenomenon.

While producing results that resemble the real world more so than comparable low-resolution ESM simulations, we stress a series of caveats that may affect the fidelity of the results presented here. For one, MRPs occur more frequently than in the real world (according to satellite observations over the last 50 years), and the modeled area of WSPs is generally larger than the only ones that have been observed in the 1970s. The simulated period of consecutive WSP events also appears to be longer than the observed 3-year WSP period of the 1970s (1974–1976; Zwally, 1983). Furthermore, convection in association with MRPs appears to be much more thorough and deeper than observed in 2016–2017 (Campbell et al., 2019). The simulation thus appears to overestimate convection when compared with the reality of the past 50 years. While this could have various reasons, it can partly be attributed to the fact that CESM1.3 does not account for the effects of ice shelves, which in turn may lead to a lack of glacial meltwater that would come from warmer CDW getting into contact with ice shelves and would contribute to enhancing the stratification of the Weddell Sea, and thereby hinder the formation of polynyas or reduce their extent (e.g., Kjellsson et al., 2015; Lockwood et al., 2021; Stoessel et al., 2015). There are also questions concerning the variability of

glacial melt water runoff as CESM1.3 uses a scheme in which more precipitation over land (or snowfall over an ice sheet) is instantaneously converted to more runoff into the ocean (see Paolo et al. (2018) and Adusumilli et al. (2020) on the possible impact of glacial runoff variability). Also, mesoscale ocean eddies are barely being resolved in these high latitude regions, which may underestimate the role of eddies in the sequence of MRPs developing into WSPs (e.g., Dufour et al., 2017). Another important process for the formation of polynyas is convection in general, and “thermobaric deep convection” (Akitomo, 2006) in particular, both of which are not resolved in this model by its governing equations, but instead crudely parameterized.

Finally, we emphasize that the basis of our study is a preindustrial control simulation, meaning that all external climate forcing is fixed at year 1850 (i.e., both the atmospheric carbon dioxide concentration and the stratospheric ozone concentration are fixed). In the real world, however, anthropogenic climate change has already altered the environmental conditions greatly in recent decades, especially the precipitation-evaporation balance in the polar Southern Ocean (e.g., de Lavergne et al., 2014). In view of this, comparisons of results from this simulation with recent polynya observations must be exercised with caution.

It is nevertheless encouraging to see the extent to which global CESM simulations can realistically capture distinct features and detailed processes in the high-latitude Southern Ocean, and that these can be maintained over several centuries of model integration, as shown for the first time with high resolution. The long model integration also allows for studying the effects of long-term deep-ocean climate drift,

which was hitherto prevented by high-resolution ESM simulations not extending for much longer than 200 years.

CHAPTER IV

ANTHROPOGENIC IMPACT ON WEDDELL SEA POLYNYA AND OPEN OCEAN DEEP CONVECTION IN HR-TN³

4.1 Background information

One of the great scientific challenges of our time is to understand human's impact on Earth's climate. Quantifying the human footprint on climate is not straightforward, because the observed record always contains both natural variability and anthropogenic signals (e.g., Fox-Kemper et al., 2021 [IPCC-AR6, Chapter 9]). For some variables, the natural variability signal is much stronger than the anthropogenic signals (e.g., Polvani & Smith, 2013). To better interpret the observed data, we need to understand both the sources of natural climate variability and the influence of anthropogenic climate change, and lastly their combined effect. During the recent decades, pronounced trends have been observed in the Southern Ocean (Latif et al., 2017), including a significant positive trend of the SAM index (e.g., Marshall, 2003; Campbell et al., 2019). This positive trend of the SAM index has resulted in a strengthening of the Southern Hemisphere circumpolar westerlies by ~15% (e.g., Marshall, 2002; Swart & Fyfe, 2012), a poleward shift of the core of these westerlies (e.g., Thompson et al., 2000; Swart & Fyfe, 2012), as well as a warming and increase of precipitation around Antarctica (Thompson & Solomon, 2002; Genthon et al., 2003; Bromwich et al., 2011). This trend is attributed both to the anthropogenic ozone depletion in the stratosphere, i.e., the “ozone hole” over Antarctica (Gillett et al., 2013;

³ Submitted to Journal of Advances in Modeling Earth Systems (Diao et al., 2022; under review)

Banerjee et al., 2020), and to the higher atmospheric CO₂ concentration due to anthropogenic emissions of greenhouse gases (e.g., Toggweiler & Russell, 2008; Gillett et al., 2013). Additional causes of the increasing SAM trend are still under debate which include the role of anthropogenic forcing versus natural variability.

Since the beginning of satellite passive-microwave remote sensing of sea-ice concentration, Weddell Sea Polynyas (WSPs) occurred only during 1974-1976 (Gordon et al., 2007). It has been hypothesized that the fresher and more stratified Weddell Sea may suppress the return of WSPs (e.g., Gordon et al., 2007; de Lavergne et al., 2014). More recently, the largest and most prolonged Maud Rise Polynya (MRP) on record occurred in the austral winter of 2016-2017 (Campbell et al., 2019). Furthermore, both observations (proxies) and numerical simulations indicate that WSPs (and the associated deep convection) were likely more common in the preindustrial period (e.g., Gordon et al., 2007; de Lavergne et al., 2014; Polvani & Smith, 2013); many models simulate WSPs as a periodically recurring phenomenon (e.g., Martin et al., 2013; Jüling et al., 2018; Kurtakoti et al., 2018, 2021; Chang et al., 2020; Diao et al., 2022). Ice core proxy data show a near-periodic oscillation of the SAM index before the instrumental period (Goodwin et al., 2004; Marshall, 2003). While observations since the 1950s show that surface freshening of the southern polar ocean has considerably enhanced the salinity stratification. It has been suggested that a persistent positive phase of the SAM index, brought on by both the stratospheric ozone depletion and the rising atmospheric CO₂ concentrations (Banerjee et al., 2020), may be delaying the return of a WSP by inhibiting the re-establishment of dry atmospheric conditions (de Lavergne et al., 2014).

In this Chapter, we investigate how the anthropogenic forcing affects the WSP formation and the associated open ocean deep convection. Our analysis uses two 250-year-long HR simulations: the first comprises the last 250 years of the 500-year-long HR-PI simulation, and the second is the corresponding HR-TN simulation from 1850 to 2100 (see Section 2). We compare HR-PI with HR-TN to distinguish the “natural” climate variability signals of polynya formation from those affected by anthropogenic climate change. We will show that interdecadal periodic deep convection in the Weddell Sea was apparently more active in the past and is weakening with anthropogenic forcing. Surface warming and freshening of the southern polar ocean after year 2040 of HR-TN considerably enhances the stratification and weakens deep convection in the central Weddell Sea, which prevents WSPs from forming. However, shallow convection continues to occur intermittently over and around the Maud Rise seamount, even though this region turns ice-free in winters. To study the impact of model resolution, we furthermore compare the HR simulations with corresponding LR simulations. We thus analyze 250 years of four simulations, respectively: HR-PI, HR-TN, LR-PI, and LR-TN. All LR simulations do not reveal any sign of WSP formation whatsoever.

4.2 Impact of anthropogenic forcing on polynya occurrence

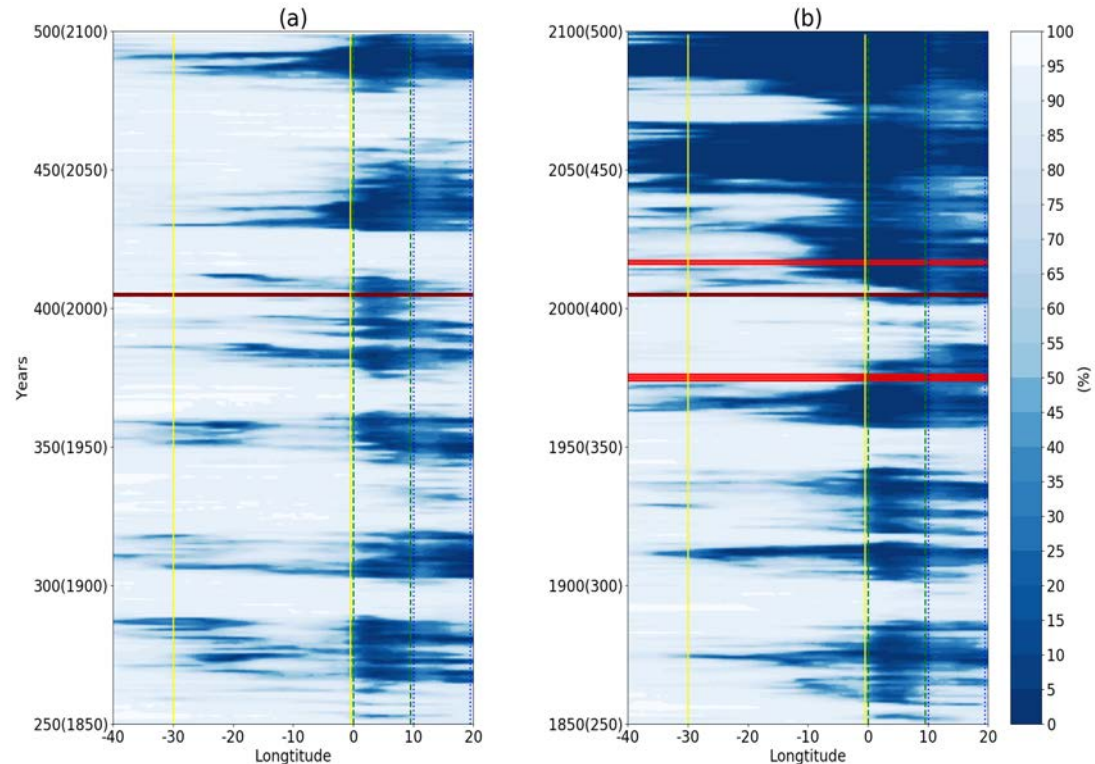


Figure 4.1. Timeseries of September sea-ice concentration (a) for model years 250-500 of HR-PI and (b) for years 1850-2100 of HR-TN, both averaged over the region 63°S - 68°S . The black line in (b) represents year 2006, when the climate forcing is changed from historical forcing to the CMIP5 RCP8.5 forcing in HR-TN, while the black dashed line in (a) (simulation year 406) has been added for comparison purposes. The red lines in (b) represent the observed polynya events of years 1974-1976 and 2016-2017. Selected regions referenced in text: the WSP region (30°W - 0° , between yellow lines), the MRP region (0° - 10°E , between green lines).

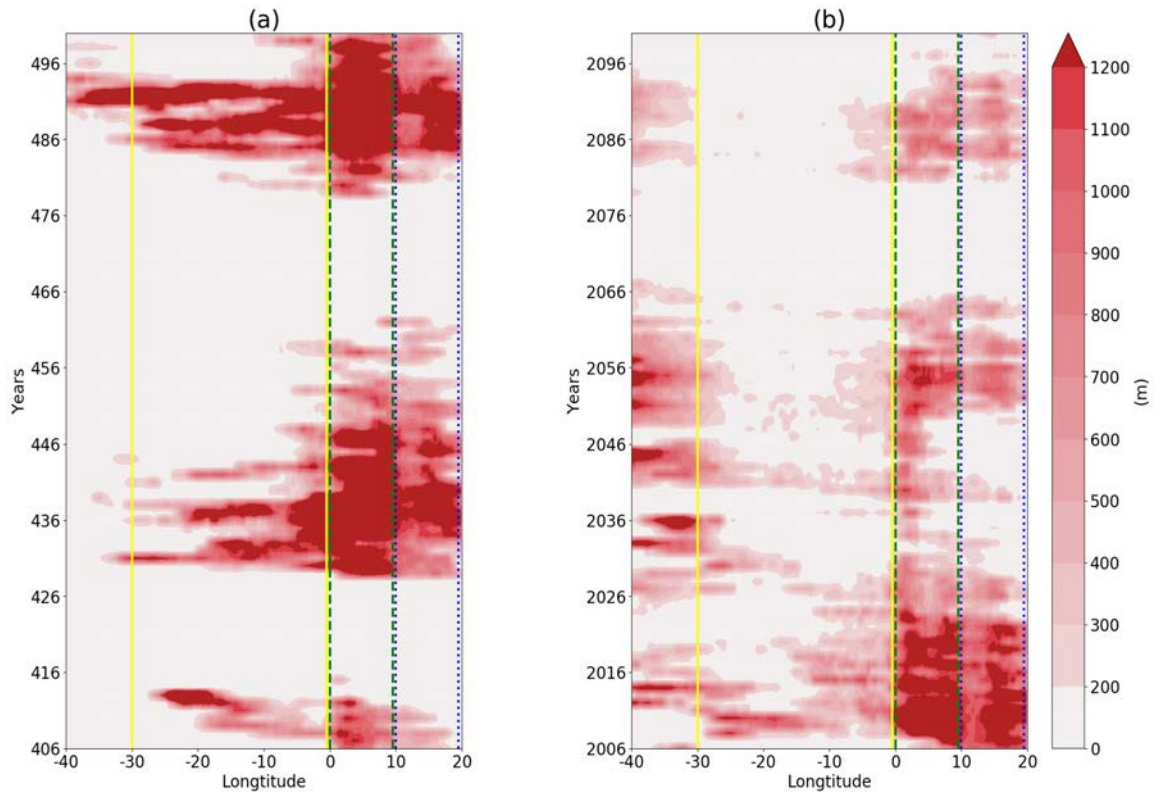


Figure 4.2. (a) Time series of September mixed-layer depth for PI-CTRL simulation. (b) Same as (a) but for HF-TNST simulation. The period ranges from the maroon lines in Fig.1 to the end of each simulation.

To explore the sensitivity of WSPs to anthropogenic climate change, we first compare the winter (September) sea ice concentration time series from HR-PI with that of HR-TN (Figure 4.1; between the yellow lines). In HR-PI, the WSPs occur intermittently with a period of about 40-50 years (Figure 4.1a; see also Chapter 3). Because both the atmospheric carbon dioxide (CO_2) and the stratospheric ozone (O_3) concentrations are fixed in HR-PI, the intermittent opening of polynyas can be regarded as natural climate variability in this simulation. HR-TN also produces WSPs intermittently (Figure 4.1b), indicating that the simulated natural climate variability is still prevailing, but superimposed on this there is a decreasing trend of winter sea ice

concentration toward the end of the simulation. The trend is slow under historical forcing (before year 2006, the black line in Figure 4.1b), while much more pronounced under the RCP8.5 forcing. After year 2040, winter conditions in the Weddell Sea become largely ice-free (Figure 4.1b). During the same time-period, the mixed-layer depth (defined as the shallowest depth where the local buoyancy gradient equals the largest buoyancy gradient of the total water column; Large et al., 1997; Chang et al., 2020) is becoming much shallower in the WSP region (Figure 4.2b), indicating a reduction of ocean deep convection. The largely ice-free conditions in HR-TN (Figure 4.1b) are thus not induced by oceanic vertical heat flux due to deep convection. In contrast, convection reaching depths of > 1200 m in HR-PI when WSPs occur (Figure 4.2a), indicates that the deep heat reservoir (mainly Weddell Deep Water or WDW; 0 ~ 0.8°C) is the main heat source for maintaining WSPs.

For reference, the LR simulations do not produce any polynyas in the Weddell Sea, and the mixed-layer depth remains shallow throughout the two LR simulations (not shown). Only the last years of LR-TN indicate a slight reduction of the September ice cover. A spatial analysis reveals that this is due to a reduction of the ice extent in the north-east corner of the box. This is consistent with the expectation that there is an overall decreasing trend of sea ice extent under anthropogenic forcing.

4.3 Impact of anthropogenic forcing on ocean salinity and temperature

To further investigate the impact of anthropogenic climate change on ocean deep convection, we present timeseries of salinity (Figure 4.3) and temperature (Figure 4.4) vertical profiles averaged over the central Weddell Sea from HR-PI (upper panels) and

HR-TN (lower panels), respectively. The impact of intermittent ocean deep convection (in concert with WSP occurrence) on temperature and salinity is similar in both simulations up until about year 2020. From then on, the WDW layer (core around 500 m) becomes noticeably saltier and warmer in HR-TN than in HR-PI (Figure 4.3b and Figure 4.4b). At the same time, the intermittent fresher and colder WDW episodes due to deep convection start diminishing. The associated shut-down of the ventilation of the deep ocean leads to salt and heat accumulation in the deep ocean, especially in the WDW layer. In HR-PI, the near-periodic deep convection events continue to occur over the entire simulation period, superimposed on a slow warming and salinification trend at depth due to model drift (Figure 4.3a and Figure 4.4a).

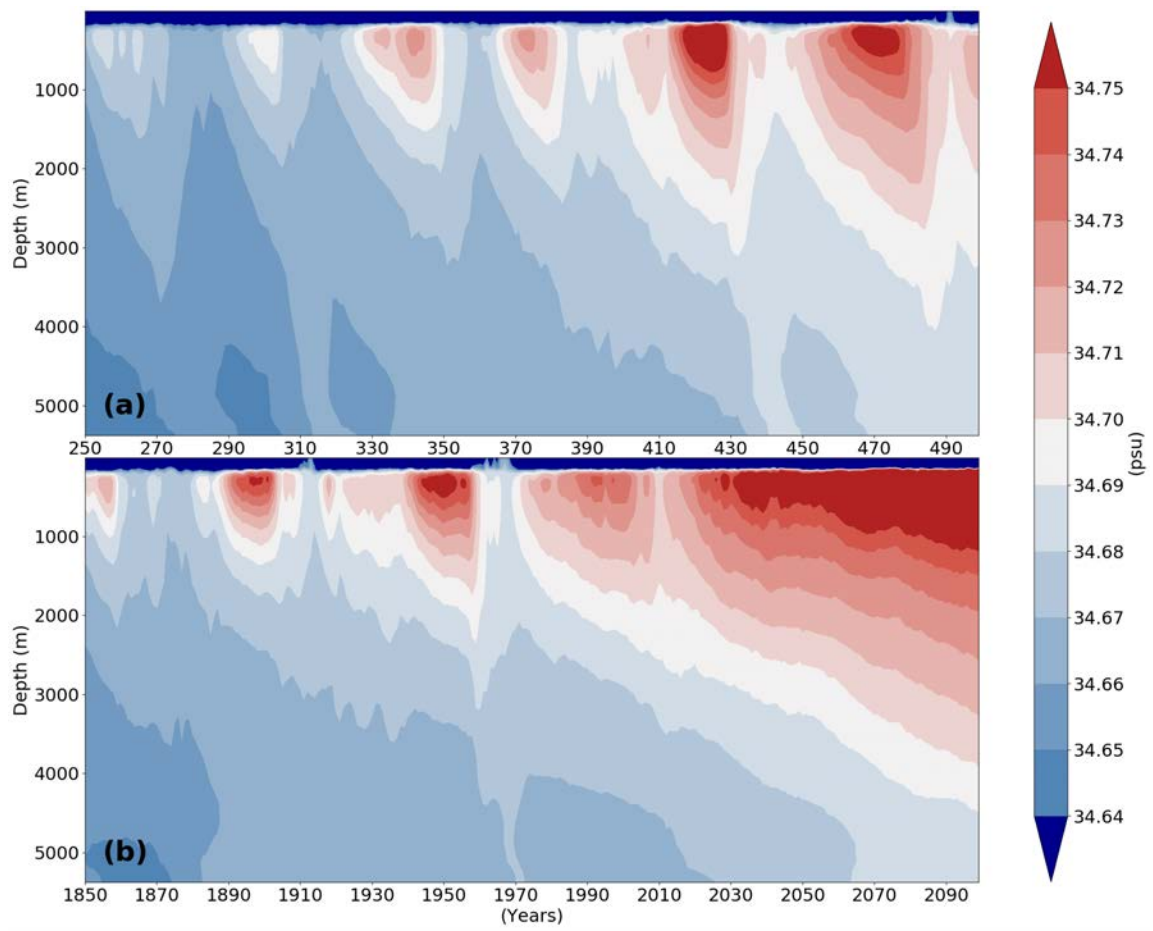


Figure 4.3. Timeseries of vertical monthly-mean salinity profiles from (a) HR-PI and (b) HR-TN. All averaged over the WSP region in Figure 4.1.

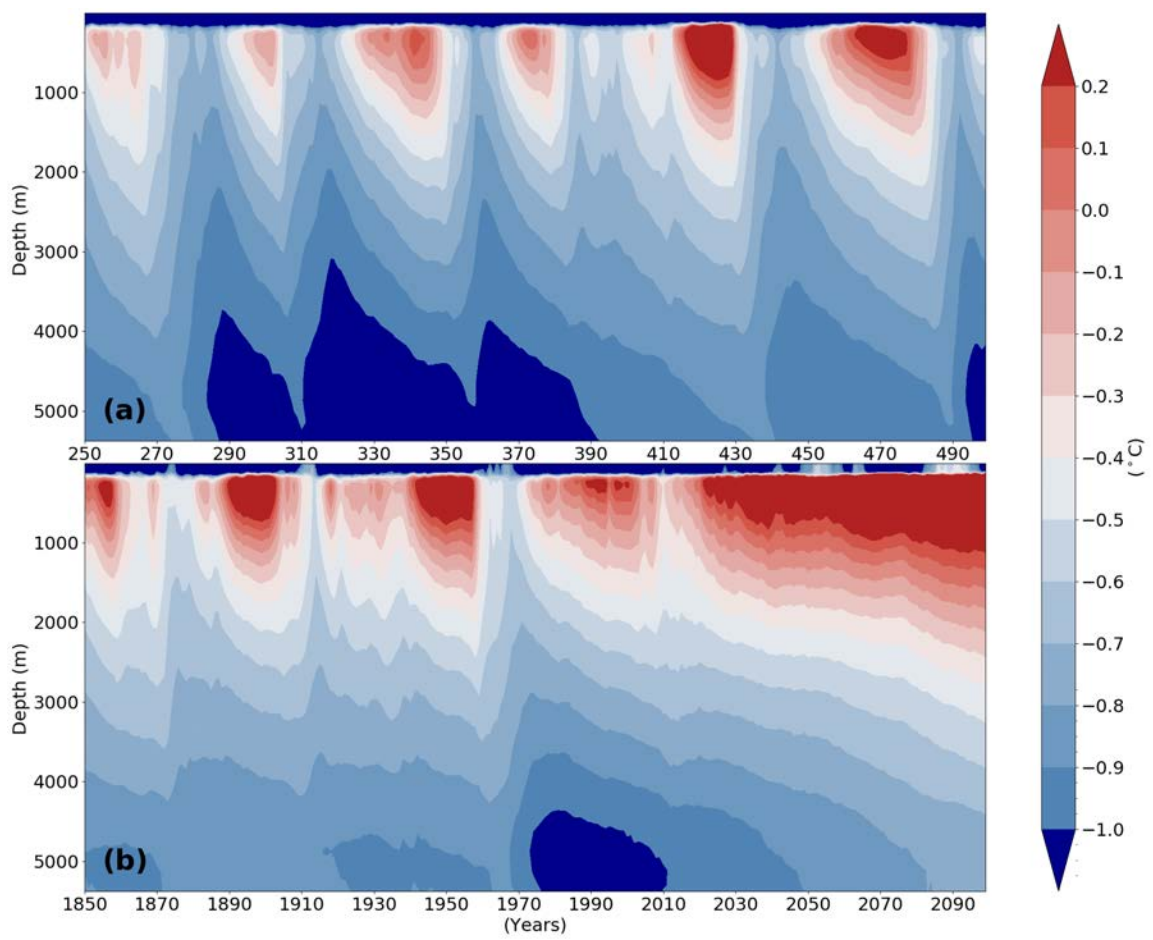


Figure 4.4. Same as in Figure 4.3, but for temperature.

4.4 Impact of anthropogenic forcing on upper-ocean temperature and salinity

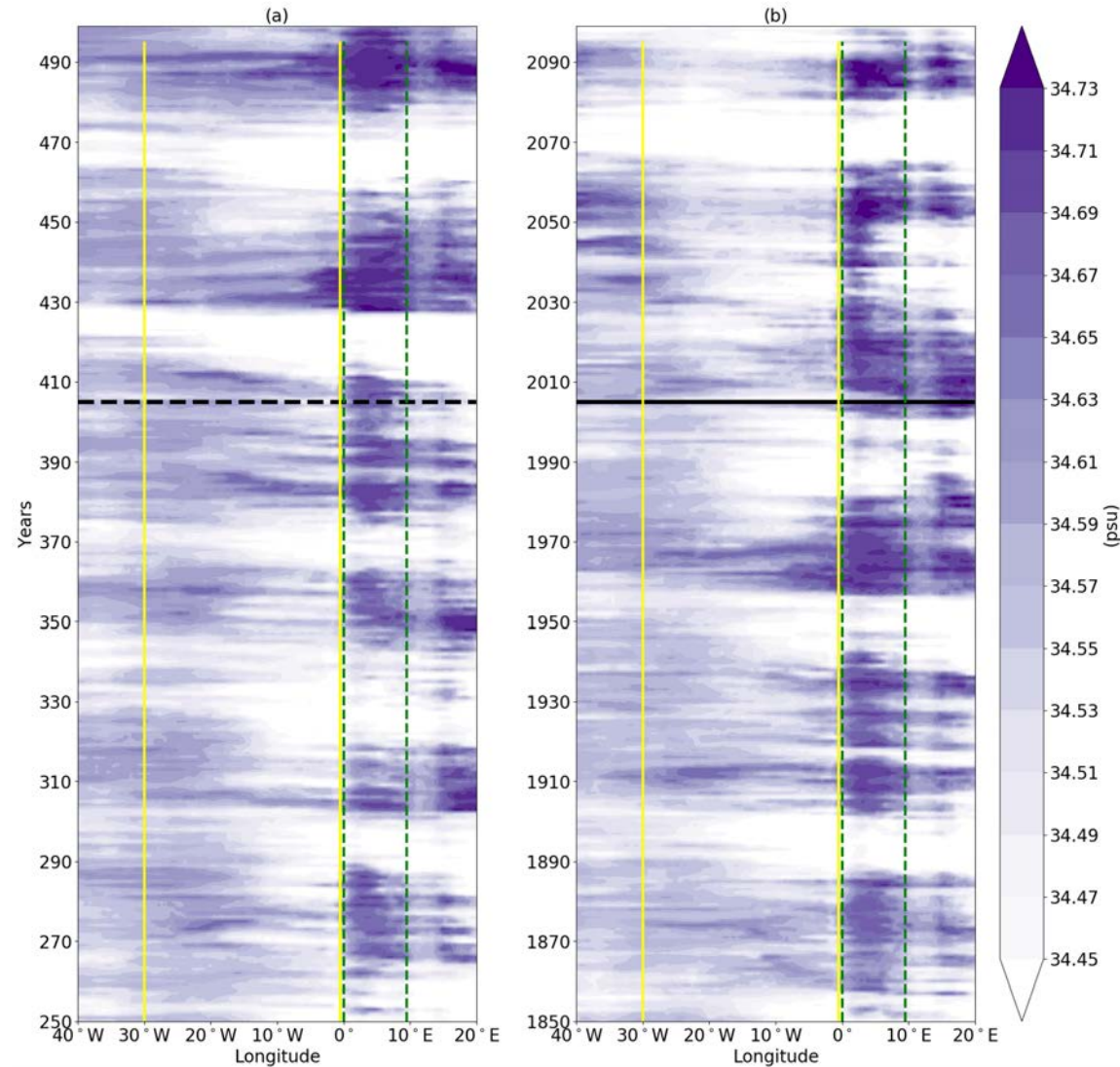


Figure 4.5. (a) September upper-ocean (upper 10m) salinity of last 250 years of PI-CTRL simulation. **(b)** Same as (a) but of HF-TNST simulation. Averaged over the region 63°S - 68°S , 40°W - 20°E .

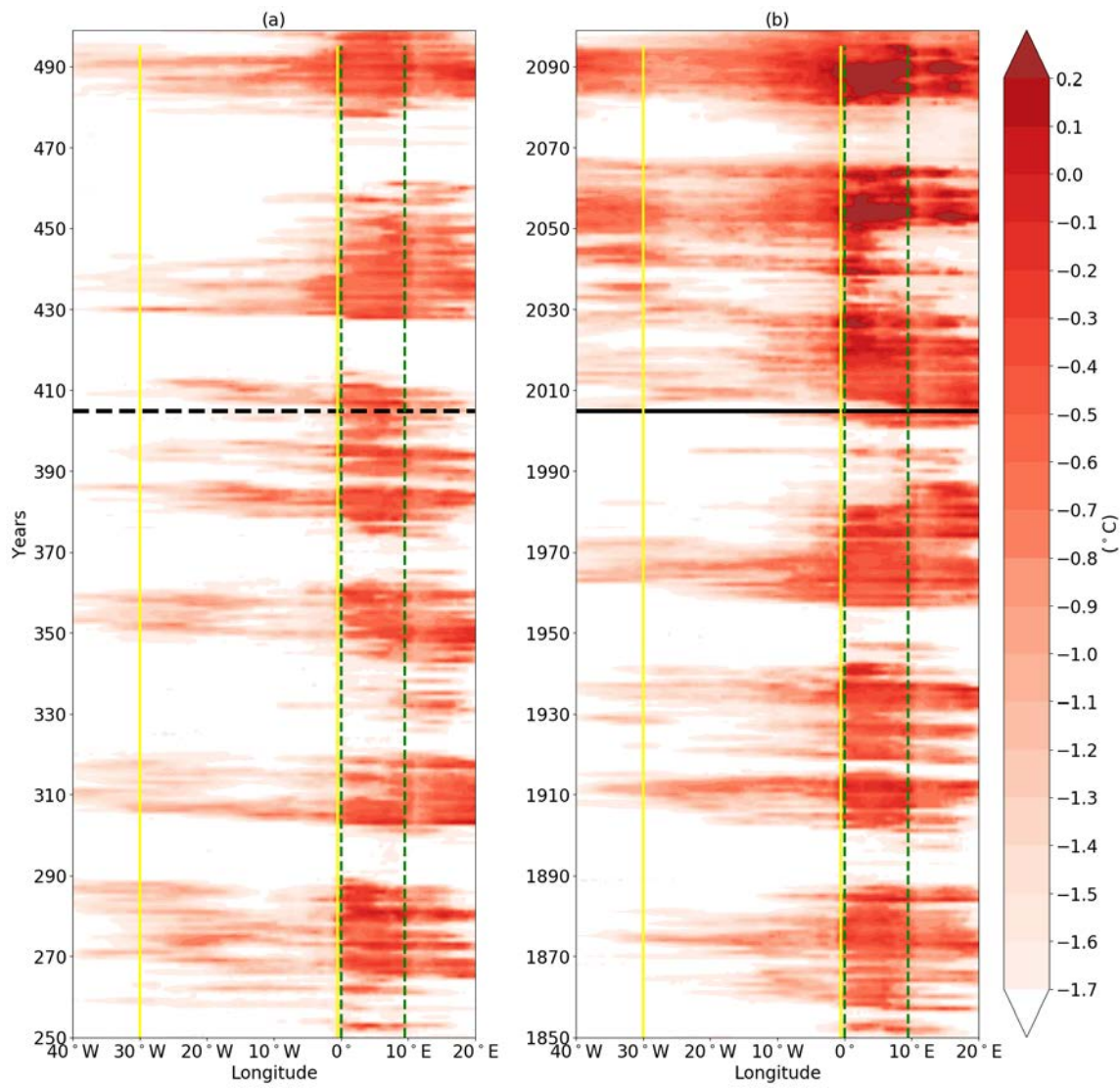


Figure 4.6. Same as Fig.4.5, but for temperature.

De Lavergne et al. (2014) and Gordon et al. (2014) showed that the upper-ocean salinity is critically linked to the build-up of upper-ocean stratification (at the prevailing near-freezing temperatures in winter), and then controls the periodicity of WSP occurrence (see also Kurtakoti et al., 2021 and Chapter 3). Here, we compare the upper-ocean salinity and temperature time series of HR-PI with those of HR-TN (Figure 4.5

and Figure 4.6, respectively). Both HR simulations reveal periodic changes of salinity and temperature that vary in concert with polynya occurrence (due to ocean deep convection). In HR-PI, the upper-ocean salinity exhibits a slow salinification trend in the central Weddell Sea region (Figure 4.5, between the two yellow lines). This is due to a slow model drift of the deep ocean salinity of the Weddell Sea (Figure 4.3a, and Zhang et al., 2021), and emerges at the surface because of deep convection during polynya events (Figure 4.2 and Figure 4.3a). In HR-TN, the upper-ocean salinity of the central Weddell Sea decreases from year 1970 onward. As will be shown later, this is due to the poleward movement of the precipitation rich westerly wind belt. In particular, the associated strengthening of stratification and reduction of ocean convection leads to positive feedback that makes the upper-ocean even fresher.

In terms of upper-ocean temperature, HR-TN shows a warming trend, especially after 2006 when the climate forcing is changed to follow the CMIP5-RCP8.5 scenario (Figure 4.6b). From 2020 onward, the upper-ocean temperature becomes increasingly dominated by surface heating rather than oceanic vertical heat flux due to convection, as also indicated by increasingly shallower winter mixed layers (Figure 4.2b). By comparison, HR-PI does not display any noticeable trends of upper-ocean temperature (Figure 4.6a). Thus, the increasing/decreasing trends of upper-ocean temperature/salinity in HR-TN both lead to a decrease of the upper-ocean density. As shown in Figure 4.7, this will eventually lead to a much stronger stratification toward the end of HR-TN integration and, in comparison to HR-PI, to a reduction in deep convection (Figure 4.3 and Figure 4.4).

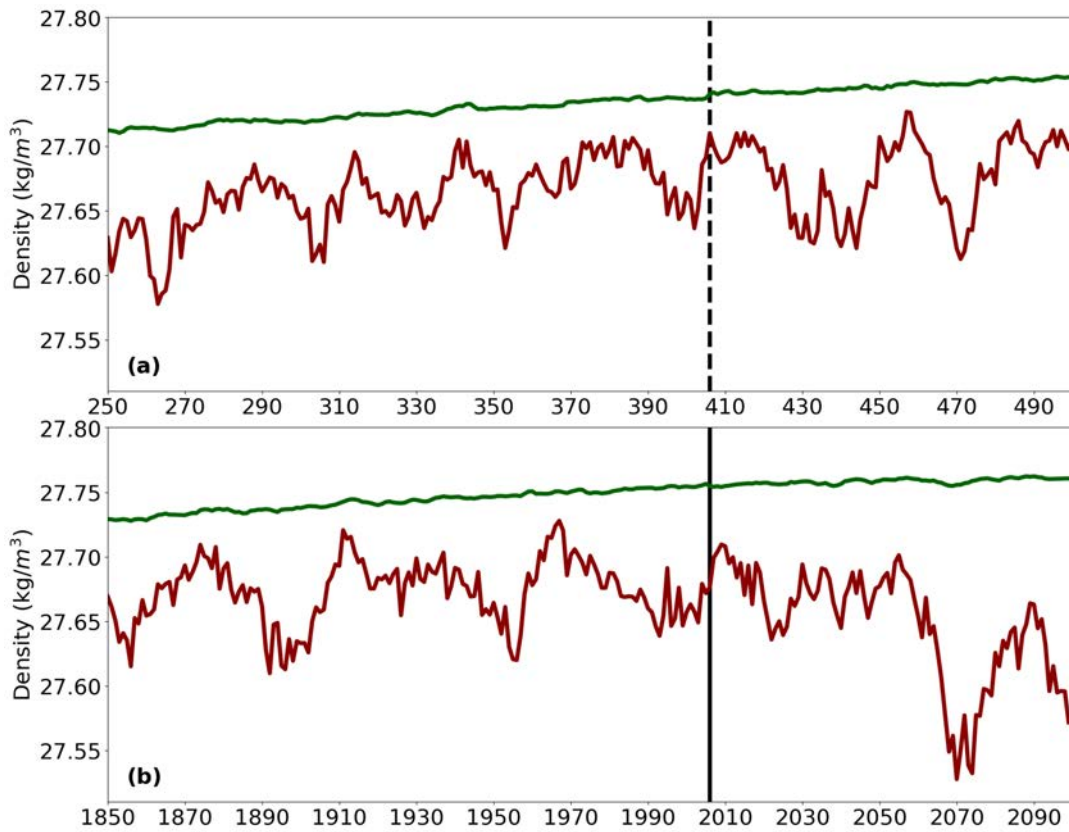


Figure 4.7. Timeseries of September water potential density from (a) HR-PI and (b) HR-TN. The respective dark-green lines represent water density at 250-m depth, while the respective dark-red lines represent the upper-ocean (10 m) density. All values are averaged over the same region as in Figure 3 and Figure 4. The black lines denote year 406/2006 in HR-PI/HR-TN. The potential density is referenced to the surface.

We should note that while winter convection ceases in the WSPs region toward the end of HR-TN integration, convection continues to occur intermittently over and around the Maud Rise seamount (between green lines in Figure 4.1), even though this region turns ice-free in winter (Figure 4.1b). Convection still transports high temperature and high salinity water to the surface, while the convection depth is gradually decreasing as indicated by a reduction of the mixed-layer depth (Figure 4.2b). The Taylor column

effect around the Maud Rise seamount (e.g., Kurtakoti et al., 2018) continues to provide the necessary conditions for shallow convection, thereby bringing warm and salty WDW to the surface in this region. This is to some extent in line with the observed occurrence of a distinct MRP in 2016 and 2017 that did not develop into a WSP.

4.5 Changes of SAM index due to anthropogenic forcing

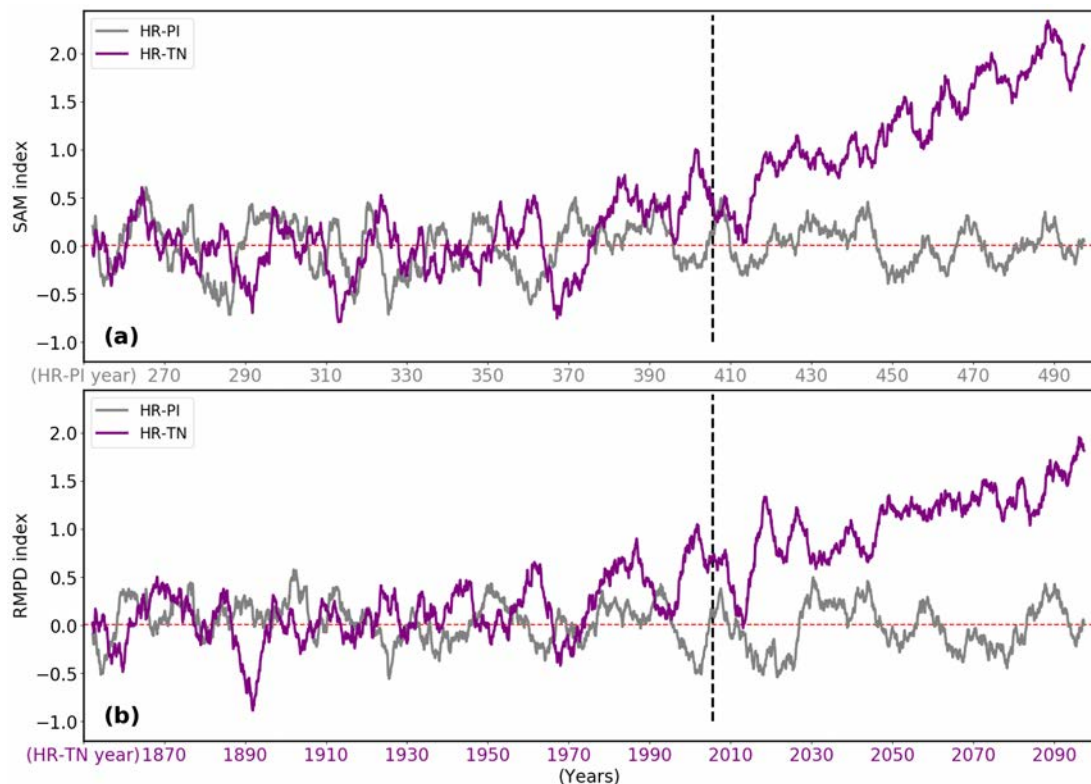


Figure 4.8. (a) Timeseries of simulated (a) Southern Annular Mode (SAM) index and (b) Regional Meridional Pressure Difference (RMPD) index (see text for definition). The grey and purple lines represent HR-PI and HR-TN, respectively. The dashed black lines represent the year when the climate forcing has been changed from historical forcing to the CMIP5 RCP8.5 forcing in HR-TN. Note that color of time axis labels correspond to respective experiments (grey: HR-PI, purple: HR-TN).

The SAM index is defined as the difference of the standardized zonal-mean sea level pressure between 40°S and 60°S ($\text{SAM} = P_{40}^* - P_{65}^*$, where P^* represents the standardized sea-level pressure; Gong and Wang, 1999). It constitutes the principal mode of the atmospheric variability in the Southern Hemisphere (Marshall, 2003). Reliable measurements of sea-level pressure in high southern latitudes have only been available since the 1970s; since then, the SAM index trended from negative to positive (Gordon et al., 2007; Campbell et al., 2019). This increasing trend of +1 from year 1972 to year 2019 (Campbell et al., 2019; their Fig. 5b) is apparently reproduced in the HF-TNST simulation (Fig. 4.8a).

However, the SAM index represents only a circumpolar zonal mean quantity. Swart and Fyfe (2012) showed that there are considerable zonal variations in the meridional position of zonal wind stress that are not being accounted for when using the SAM index. Following Fig. 2c of Swart and Fyfe (2012), we show the zonal variation of the meridional position of maximum zonal wind stress for 2 periods from HF-TN (Figure 4.9). As can readily be detected, some sectors around Antarctica (such as the Weddell Sea sector) experience a substantial meridional shift of the position of maximum zonal wind stress from the first 50 years to the last 50 years of HR-TN, while there are hardly any shifts in other sectors (such as the western Ross Sea sector). To focus on the regional impact on the Weddell Sea, we therefore define a regional SAM-like index, which is equivalent to the SAM index except that it is based on the difference of standardized sea-level pressure between 40°S and 65°S averaged over only the

longitudinal range between 40°W - 30°E ; we call it the Regional Meridional Pressure Difference (RMDP) index (see also in Chapter 3).

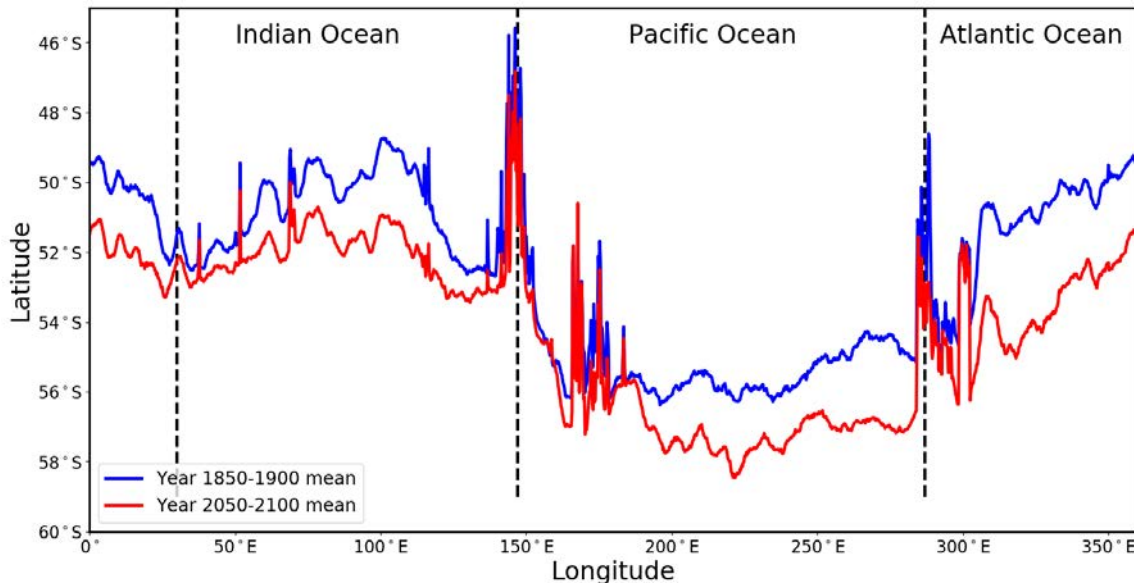


Figure 4.9. Climatology of the maximum zonal wind-stress position around Antarctica. Blue and red lines represent the time-mean positions for 1850-1900 and 2050-2100, respectively, from HR-TN.

Figure 4.8b shows the simulated RMPD index time series. For most of the time, the SAM and RMPD indices match relatively well, both in terms of trends and variability, which indicates that the changes of the SAM index are to a large extent controlled by sea level pressure (SLP) changes over the Weddell Sea, or vice versa. In contrast to the RMDP index of HR-PI, which shows no sign of a trend (grey line), that of HR-TN shows an increasing trend starting in the 1960s (purple line), which is consistent with the timing of the accelerated increase of the global-mean near-surface air temperature due to anthropogenic effects (e.g., IPCC-AR6, 2021).

To determine the main source of the variability of the RMPD index, we show the timeseries of P_{40}^* and $-P_{65}^*$ from HR-PI (Figure 4.10a) and HR-TN (Figure 4.10b) separately. In HR-PI, it is readily discernable that the SLP variability over the high-latitude Weddell Sea (P_{65}^*) explains most of the variability of the RMPD index ($r = 0.88$), while the contribution of the variability of P_{40}^* is relatively small ($r = 0.50$). As shown in Diao et al. (2022), P_{65}^* varies in concert with the near-periodic occurrence of WSPs in HR-PI. In HR-TN, on the other hand, the contributions from both P_{40}^* and P_{65}^* are equally important (especially after about year 2000), and the RMPD index thus not mainly determined by P_{65}^* . The more notable difference between HR-PI and HR-TN occurs in their respective trends: HR-PI does not show a trend in either P_{65}^* or P_{40}^* , while HR-TN has a decreasing SLP trend at high latitudes (Figure 4.10b shows $-P_{65}^*$) and an increasing SLP trend at mid-latitudes (P_{40}^*). Their combined effect makes the RMDP index ($\text{RMDP} = P_{40}^* - P_{65}^*$) increase faster – a trend that is similar to the recently observed SAM index trend (Gordon et al., 2007; Campbell et al., 2019). The simulated changes in SLP are also consistent with the expectation that the subtropics are widening, and that the mid-latitude westerlies are shifting poleward with an increase in atmospheric CO₂ levels (e.g., Toggweiler & Russell, 2008).

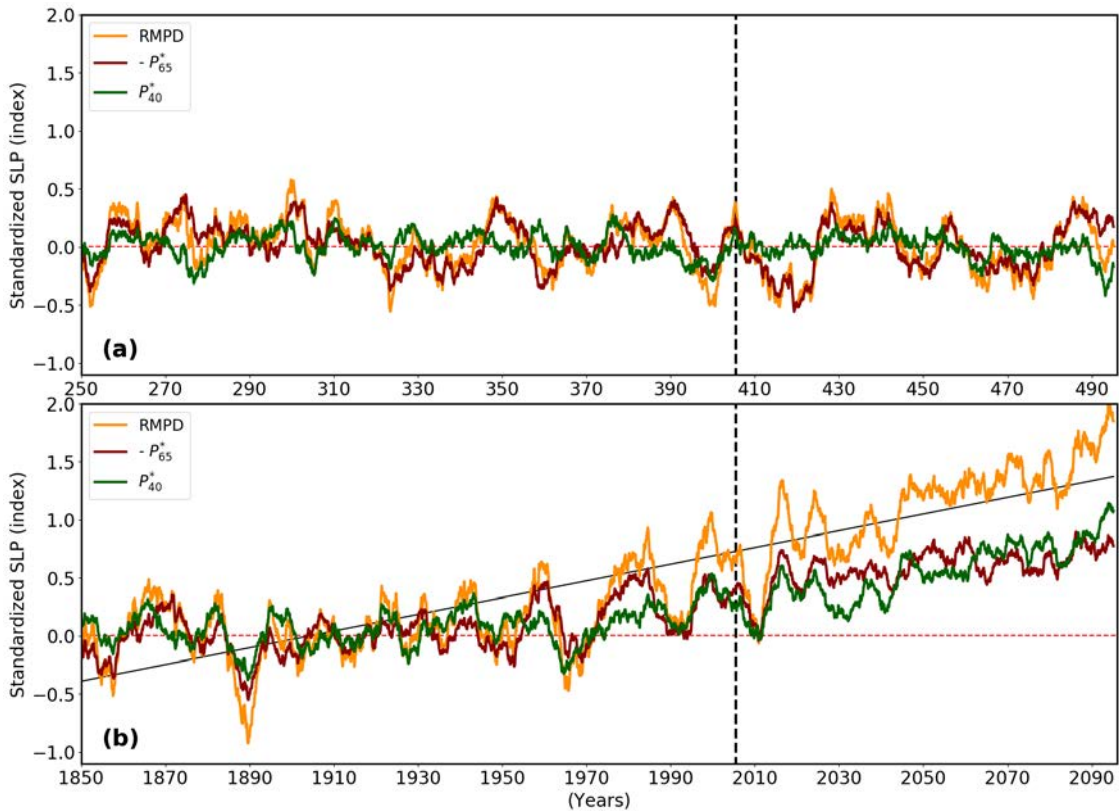


Figure 4.10. (a) Simulated RMPD index from (a) HR-PI and (b) HR-TN. Orange lines repeat the RMPD index shown in Figure. 4.8b. Red and green lines show the standardized sea-level pressure at 65°S (times minus one) and 40°S, respectively. Red dash line (=0) is mean value in (a), while the black solid line is the linear trend of RMPD in (b), the slope is 0.0072. Otherwise as Figure 4.8.

Because the LR simulations do not produce any open-ocean polynyas, possible feedbacks from WSPs, as proposed by Diao et al. (2022), cannot exist. We nevertheless check the timeseries of P_{40}^* and $-P_{65}^*$ from LR-PI and LR-TN for comparison. In LR-PI, the contributions from both P_{65}^* ($r = 0.96$) and P_{40}^* ($r = 0.93$) are both important for the variability of the RMPD index (Figure 4.11). Furthermore, $-P_{65}^*$ and P_{40}^* oscillate in phase ($r = 0.79$), which suggests that the RMPD variability of the LR-PI simulation is governed by large-scale SLP variability that affects the mid- and high latitudes

simultaneously. In LR-TN, the anthropogenic effects induce a decreasing SLP trend at high latitudes, and an increasing SLP trend at mid-latitudes, similar to the HR-TN.

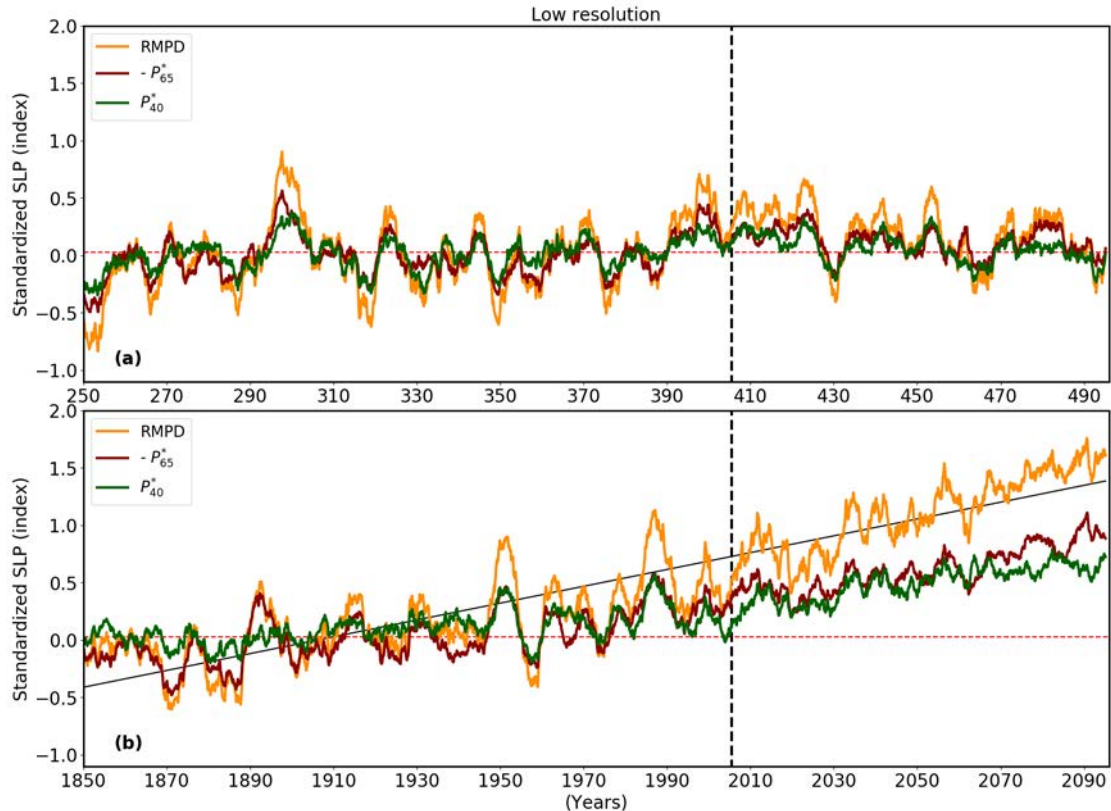


Figure 4.11. Simulated RMPD index (orange) from (a) LR-PI and (b) LR-TN. Red and green lines are the standardized sea-level pressure at 65°S (with a minus sign) and 40°S, respectively. Red dash line ($=0$) is mean value in (a), while the black dash line is the linear trend of RMPD in (b), the slope is 0.0073.

The increasing trend of the RMPD index in HR-TN and the associated decreasing SLP trend at high latitudes and increasing SLP trend at mid-latitudes are consistent with the zonal-mean westerly wind belt moving poleward and the westerly winds becoming stronger. The time evolutions of the latitudinal position and the strength of the maximum westerly wind-stress (after taking zonal mean over the RMDP index

range) are shown in Figure 4.12. They reveal that both wind properties follow the observed trends up until year 2006 (about -0.5 degree and +0.005 Pa from year 1980 to year 2006) and the expected trends for the RCP8.5 scenario up until year 2100 (e.g., Swart & Fyfe, 2012; their Figure 4). In HR-TN, the wind stress maximum increases by about 10% by the end of this century (Figure 4.12b), while the core of the westerlies shifts a remarkable 2° - 3° southward (Figure 4.12a), consistent with Figure 4 of Swart & Fyfe (2012).

In LR-TN, the zonal wind stress maximum moves more poleward, and its core becomes stronger after about year 2000, consistent with HR-TN (Figure 4.13). However, one noticeable difference is that the zonal wind stress maximum in LR-TN is considerably larger (about 0.275 Pa) than that of HR-TN (about 0.205 Pa) (Figure 4.12b and Figure 4.13b).

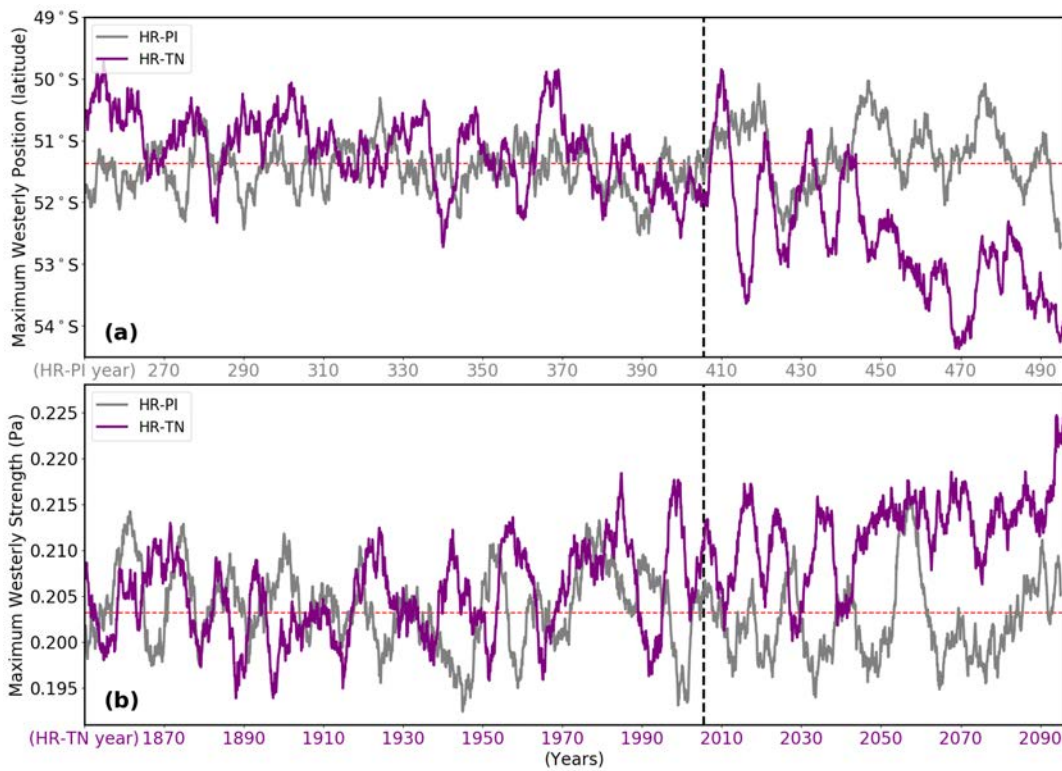


Figure 4.12. (a) The latitudinal position of the maximum zonal-mean westerly wind stress. **(b)** The magnitude of the maximum zonal-mean wind stress. Purple and grey lines represent HR-TN and HR-PI, respectively. Zonal mean is over the same longitudinal extent as the RMDP index. The vertical black line is year 2006 (same as in Figure. 4.1), while the lateral red line is the mean value of the HR-PI time series (grey line).

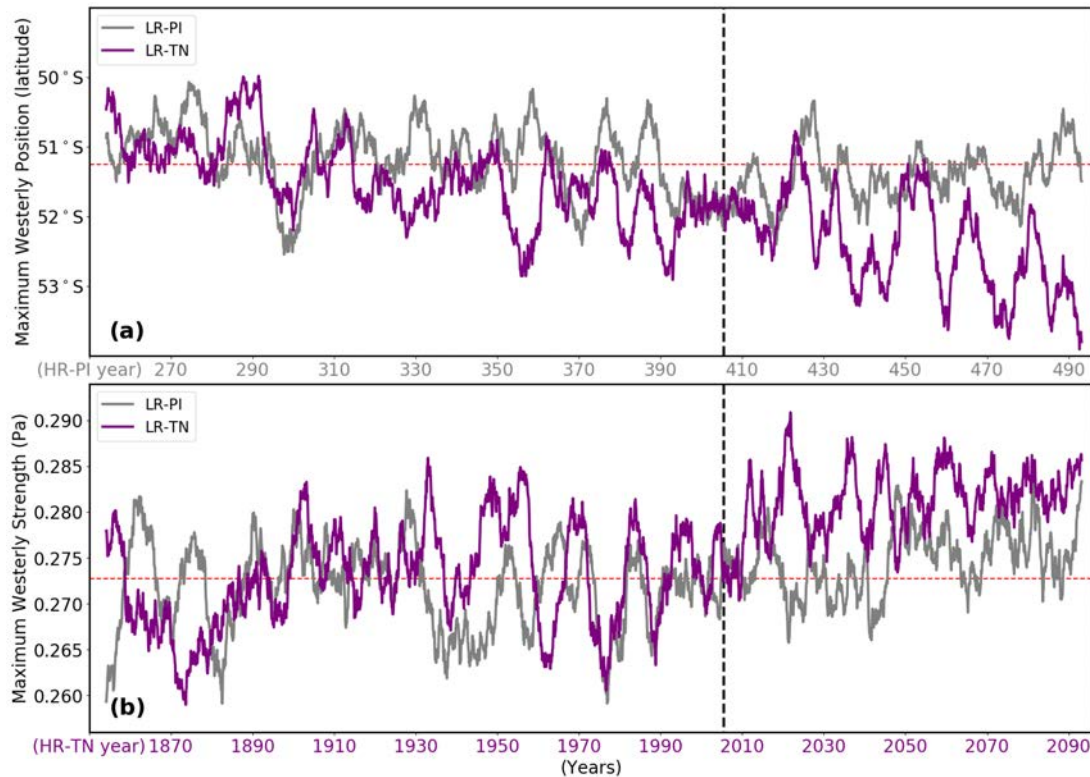


Figure 4.13. The latitudinal position of the maximum zonal-mean westerly wind stress. (b) The magnitude of the maximum zonal-mean wind stress. Purple and grey lines represent LR-TN and LR-PI, respectively. Zonal mean is over the same longitudinal extent as the RMDP index. The vertical black line is year 2006 (same as in Figure 4.12), while the lateral red line is the mean value of the LR-PI time series (grey line).

4.6 Trends of ice concentration, air temperature, and precipitation

Besides changing the wind-stress curl, the poleward shift of the westerly winds is also expected to bring more precipitation to the WSP formation region (Montade et al., 2019). Figure 4.14a shows timeseries of the annual-mean total precipitation and of the 5-year running mean of September sea-ice concentration from HR-TN (averaged over the region 63°S - 68°S , 40°W - 20°E). There is a pronounced increasing trend of precipitation, especially after year 2006 (Figure 4.14a). Figure 4.15 shows the spatial

distribution of the total precipitation difference between the last decade (2090-2100) and the first decade (1850-1860) of HR-TN. In the last decade of HR-TN, there is clearly more precipitation (red) over the polar Southern Ocean near Antarctica, and less precipitation (blue) further north. This indicates that the long-term precipitation increase is governed by the anthropogenically forced poleward shift of the precipitation-rich westerly wind belt, while the short-term fluctuations of precipitation (Figure 4.14a) are most likely forced by the periodic occurrence of WSPs (see also Diao et al., 2022).

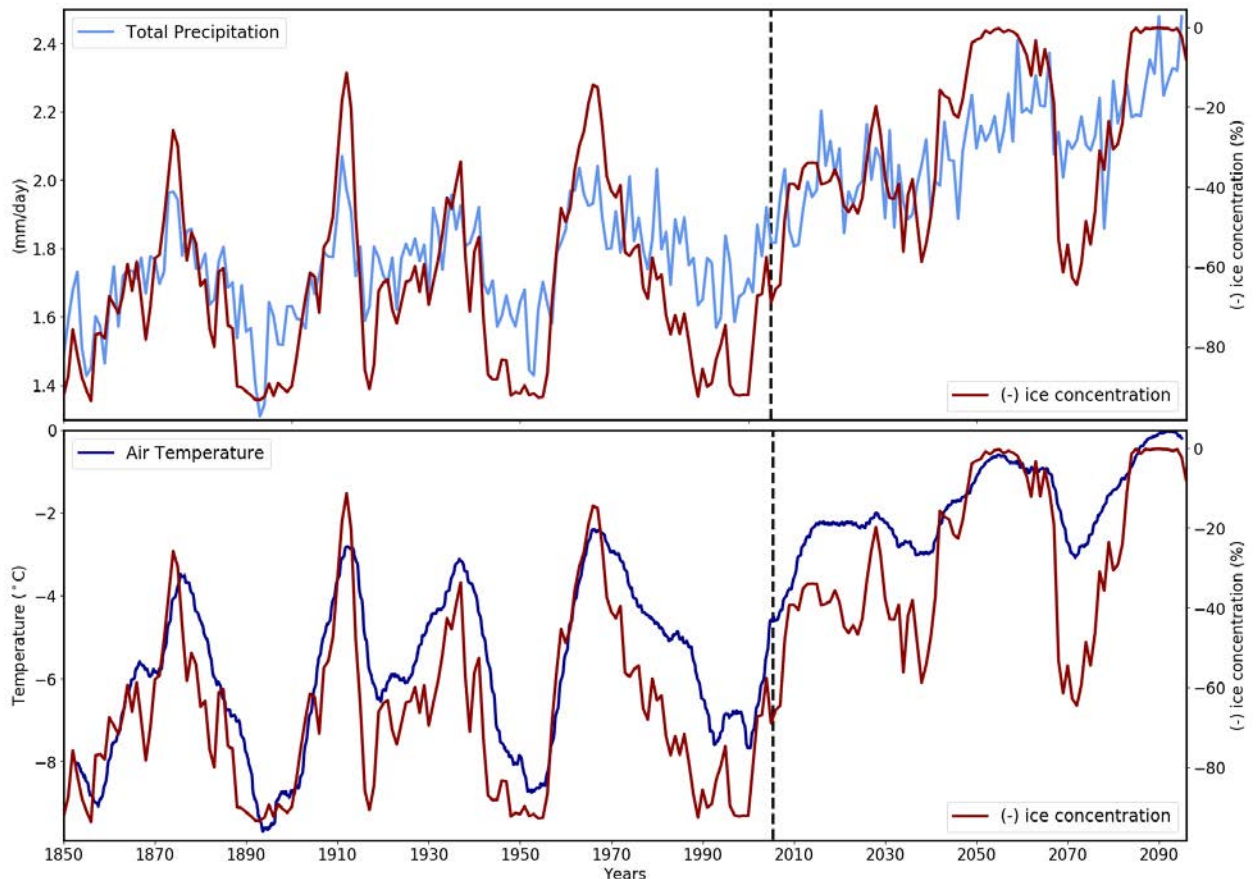


Figure 4.14. (a) Timeseries of annual-mean total precipitation (light blue line). **(b)** Timeseries of 5-year running mean of monthly near-surface air temperature (dark blue line). The maroon lines in both (a) and (b) show the timeseries of September (inverted) ice concentration. All timeseries are from HR-TN and averaged over 63°S - 68°S, 40°W-20°E. The vertical black line is year 2006 (same as in Figure 4.1)

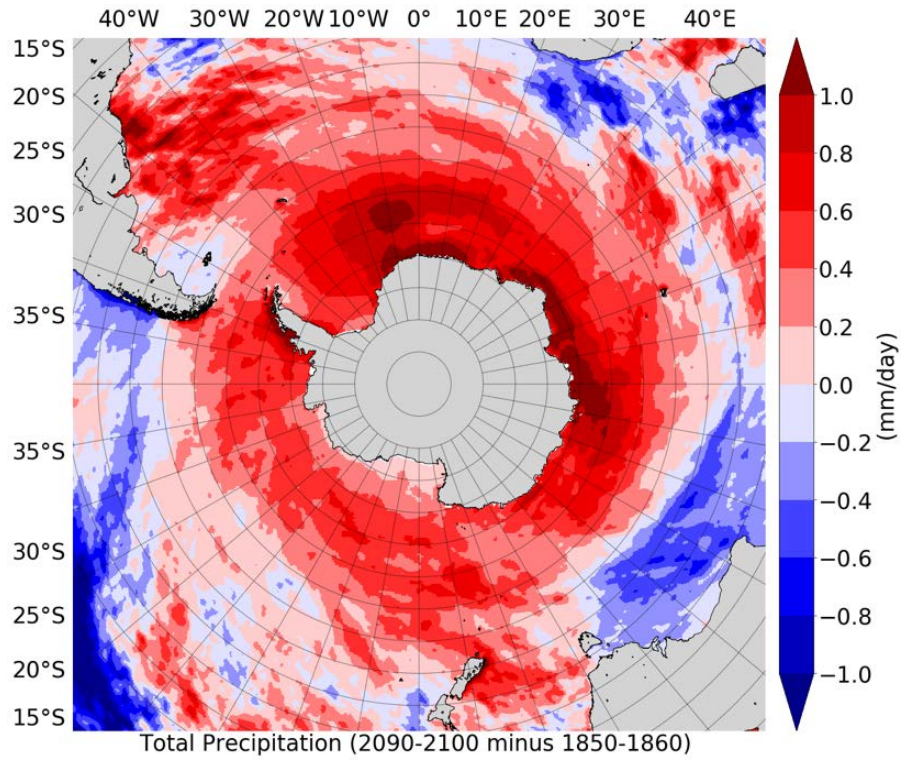


Figure 4.15. Spatial distribution of the total precipitation difference between the last decade (2090-2100) and the first decade (1850-1860) of HR-TN.

Upon formation of a WSP, a large amount of heat from the WDW layer will be released to the atmosphere, which will increase the near-surface air temperature (Figure 4.14b). Even though the air temperature is undergoing substantial interannual and interdecadal variations in concert with WSP occurrence, there is evidently a long-term positive trend, especially after the switch to the RCP8.5 forcing (Figure 4.14b). This increasing trend may be attributed to two factors. Firstly, when the CO₂ concentration increases, the associated greenhouse effect will directly increase the near-surface air temperature. Secondly, the poleward movement of the westerly wind belt exposes the maritime southern high latitudes to warmer air masses. When the air temperature is

increasing, the associated sea ice retreat leads to accelerated warming (positive feedback) and more precipitation. The combination of more precipitation and warmer air temperatures will lead to a fresher, warmer, and thus lighter mixed layer (Figure 4.7). This, in turn, will lead to a more stratified Weddell Sea, and a suppression of the return of WSPs. When the air temperature is high enough, the winter ice area shrinks to a point where WSPs can even theoretically not form because there is simply not enough ice to surround an ice-free patch (Figure 4.14b and Figure 4.1).

Another noticeable phenomenon is that the long-term reduction of sea ice is asymmetric around Antarctica in HR-TN: although sea ice in the Weddell Sea experiences a substantial reduction after year 2040, this is not the case for the winter ice pack in the Ross Sea (Figure 4.16). The asymmetric poleward movement of the westerly winds under anthropogenic forcing (shown in Figure 4.9) may, to some extent, explain this. The poleward shift is most pronounced in the Atlantic Ocean sector (WSP region), while in the western Pacific Ocean sector, especially between 150°E and 180°E, there is essentially no change in position. This is likely a main reason for why the winter ice pack in the Ross Sea is not changing much after year 2040. In contrast to HR-TN, LR-TN yields an overall reduction of winter ice extent (Figure 4.17), but not to the point that the Weddell Sea becomes ice-free in winter as in HR-TN. Besides the asymmetry of the poleward shift of the westerlies, it appears that the more detailed bathymetry of the Maud Rise seamount in the HR simulations is another reason for the asymmetry of sea-ice reduction under anthropogenic forcing.

Satellite observations reveal that the Antarctic sea-ice extent has undergone a positive trend since the late 1970s until 2016, and most of this increase has occurred in the region of the Ross Sea (Zwally et al., 2002; Parkinson & Cavalieri, 2012; Turner et al., 2009). Although the changes in sea-ice extent in the Antarctic since the late 1970s are well documented, their causes are still under debate (Parkinson & Cavalieri, 2012), in particular the cause of the unexpected dramatic reduction in 2016 and 2017 (Eayrs et al., 2021). Baines & Fraedrich (1989), based on rotating tank experiments, proposed that the wind fields are strongly controlled by topography around the Antarctic, thus featuring a pronounced wave-number-3 pattern. Especially the northward extension of the orography near 150°E, and the presence of the Ross Sea embayment, turned out to be ideal conditions for the formation of a semi-persistent atmospheric low-pressure system over the Amundsen Sea (the Amundsen Sea Low or ASL). The ASL represents a key component of the non-zonal climatological circulation with significant influence in the Pacific sector of the high southern latitudes (Raphael et al., 2016; Eayrs et al., 2021, their Figure 2). Although our simulations do not capture the increasing sea-ice extent trend (possibly because of insufficient glacial ice melt), HR-TN preserves the winter sea ice cover in the Ross Sea up to year 2100, quite in contrast to the Weddell Sea (Figure 14). This may be due to the fact that HR-TN captures the northward extension of the westerlies at 150°E and 290°E (70°W) very well (Figure 4.9).

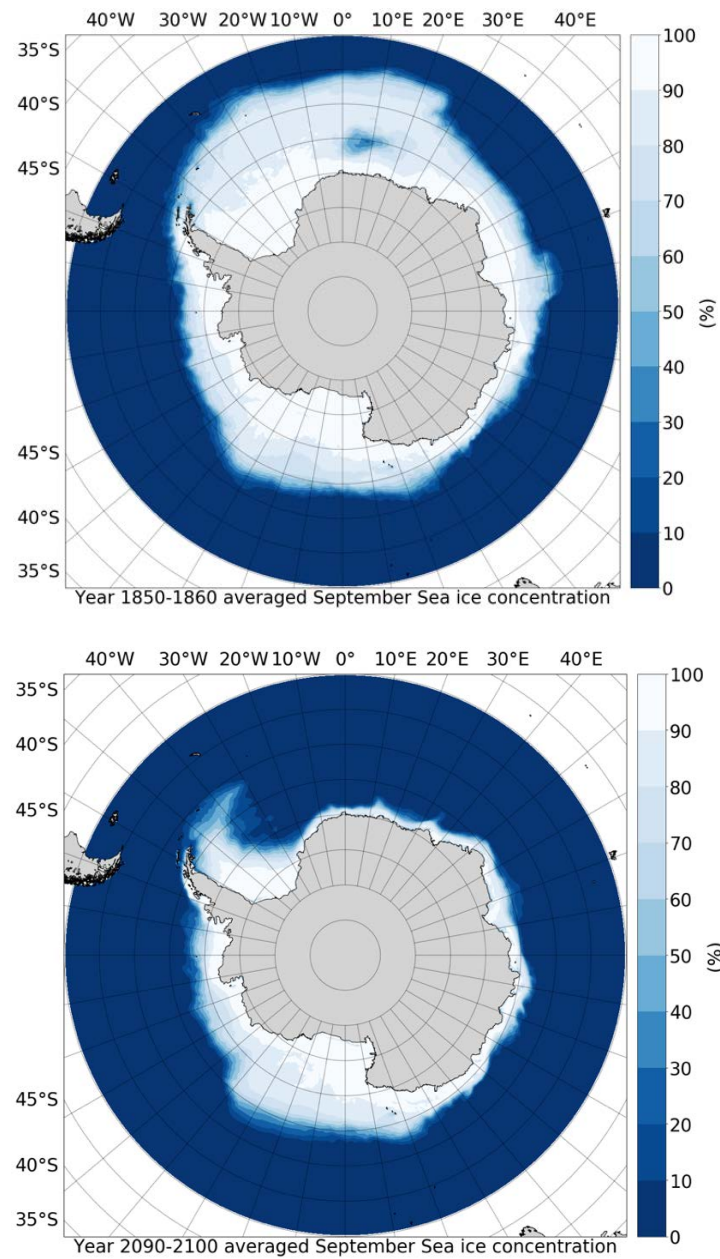


Figure 4.16. September sea ice concentration around Antarctica averaged over the first 10 years and the last 10 years of HR-TN.

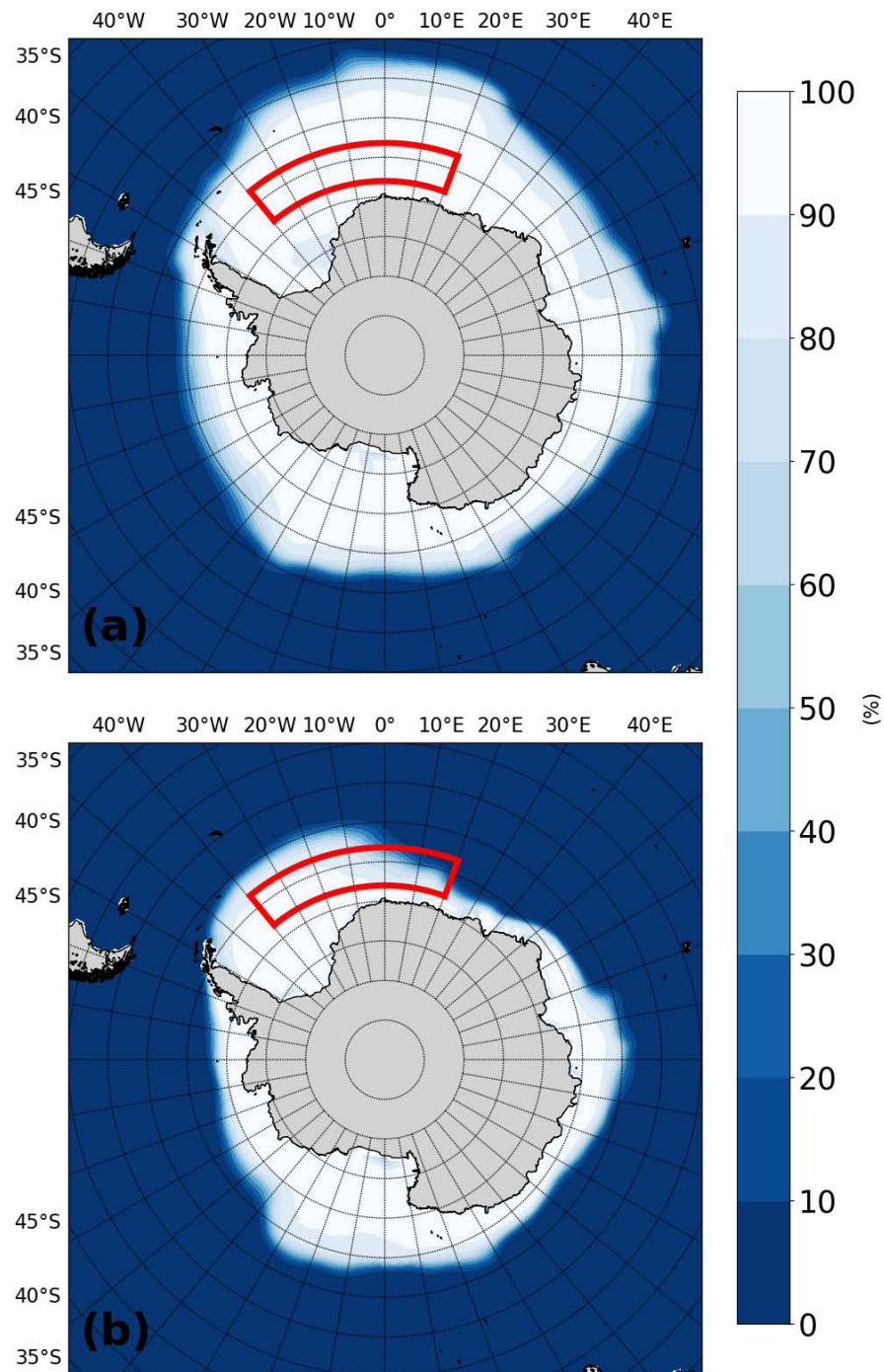


Figure 4.17. September sea ice concentration around Antarctica averaged over (a) for the first 10 years and (b) for the last 10 years of LR-TN. Red box (between 63°S - 68°S and 40°W - 20°E) used for analysis of specific variables.

4.7 Summary and conclusions

Two 250-year-long HR CESM simulations are compared to distinguish the natural climate variability signals of polynya formation (HR-PI) from those affected by anthropogenic climate change (HR-TN). We show that interdecadal periodic deep convection in the Weddell Sea was apparently more active in the past and is weakening with anthropogenic forcing. Our study leads to the following conclusions:

- (1) In both HR simulations, the RMPD index is mainly determined by the SLP variability over the central Weddell Sea (P_{65}^*), while the contribution from mid-latitudes (P_{40}^*) is relatively small. As elaborated upon by Diao et al. (2022), P_{65}^* co-oscillates strongly with the occurrence of WSPs in HR-PI.
- (2) In HR-PI, the RMPD (and the SAM) indices oscillate with no discernable trends over the entire simulation period. These oscillations indicate that the long-term variability in this region is governed by an internal self-sustained atmosphere-ocean coupled mechanism (Chang et al., 2020; Gnanadesikan et al., 2020; Diao et al., 2022). In addition, the relatively stable RMPD index oscillation provides a key environment for the intermittency of WSP formation in HR-PI, with possible reinvigorating feedback from WSPs onto the RMPD index.
- (3) In contrast, while HR-TN also produces pronounced interdecadal oscillations of the RMPD index in the first 150 years, the anthropogenic forcing (external) drives the RMPD index toward a more positive phase until 2100. The marked SLP increase in mid-latitudes and the simultaneous SLP decrease in the higher latitudes is consistent with the westerly winds becoming stronger and moving poleward.

(4) The poleward movement of the westerly winds brings more precipitation to the Weddell Sea, as well as more heat. The combined effects lead to a fresher, warmer, and thus lighter mixed layer. The resulting stronger stratification eventually suppresses the return of WSPs, or rather makes them obsolete when there is not enough sea ice in winter to enclose an ice-free area in the open ocean.

(5) While winter convection ceases in the WSP region toward the end of the HR-TN simulation, convection continues to occur intermittently over and around the Maud Rise seamount (even though this region turns ice-free in winter). This is to some extent in line with the observed occurrence of a distinct MRP in 2016 and 2017 that did not develop into a WSP.

(6) The corresponding LR simulations do not produce any open-ocean polynyas, so WSP feedbacks do not exist. In contrast to HR-PI and HR-TN, the contributions from P_{40}^* and P_{65}^* are nearly equally important for the RMPD index change in LR-PI and LR-TN. Furthermore, the SLP at 65°S and 40°S co-oscillates at the same phase, which indicates that large-scale atmospheric internal variability affects the mid- and high latitudes simultaneously.

(7) While the last century of HR-TN reveals a substantial reduction of winter ice cover over the Weddell Sea, the Ross Sea is much less affected in that regard. In LR-TN, on the other hand, anthropogenic forcing leads to an overall reduction of ice extent, but not to quasi-ice-free winters in the Weddell Sea as in HR-TN.

Several uncertainties remain in projecting the future influence of anthropogenic forcing on WSP formation. Despite the unprecedented simulation length of 500 years for

HR-PI (from which HR-TN has been branched off), we cannot rule out unrealistic behavior due to the influence of model drift in the deep ocean (Figure 4.3 and Figure 4.4). Even though considered high-resolution for a global Earth system model, several key processes, like deep convection in the ocean, which is governed by plume convection on the scale of order 0.5 km in nature (e.g., Marshall & Schott, 1999; Sohail et al., 2020; Vreugdenhil & Gayen, 2021), are still crudely parameterized in both HR simulations. Moreover, there is no ice shelf model in CESM1.3; thus, a warmer ocean adjacent to Antarctica will not trigger more ice shelf melt. This potentially may lead to additional adverse consequences for the robustness of our climate change simulations (e.g., Lockwood et al., 2021; Huot et al., 2021).

CHAPTER V

ANTHROPOGENIC IMPACT ON ANTARCTIC SLOPE CURRENT AND DENSE SHELF WATER OVERFLOW

5.1 Background information

Antarctic continental shelves and slopes occupy relatively small areas but the physical processes happening in these areas have a large impact on the global ocean circulation and the stability of the Antarctic ice sheet (Orsi et al., 1999; Whitworth et al., 1998; Pritchard et al., 2012). Coastal polynyas are a frequent phenomenon adjacent to the Antarctic continent (Tamura et al., 2008; Tamura et al., 2016), and are mostly associated with offshore blowing katabatic winds (e.g., Morales Maqueda, 2004; Stössel et al., 2011; Zhang et al., 2015). In the “dense shelf” regime (see Chapter 1), the shelf water salinity is relatively high due to continuous sea-ice formation in coastal polynyas; as a result, shelf water gets dense enough to fill the bottom layers of the continental shelves. Upon reaching the sill depths, the accumulated Dense Shelf Water (DSW) cascades down the continental slope, thereby mixing with the warmer ambient water (mostly CDW), to finally form the Antarctic Bottom Water (AABW) that characterizes the abyssal layers of the global ocean circulation (Orsi et al., 1999; Orsi et al., 2002). Under the climate conditions of the past four decades, AABW has almost entirely formed via shelf-slope convection involving DSW overflow (Gordon., 2014).

A question we want to address in this chapter is how well the processes described above are represented in state-of-the-art Earth System Models (ESMs). In low-resolution (LR) ocean models (horizontal resolution $> 0.5^\circ$), the complex shelf dynamics leading to DSW overflow are not well resolved (Danabasoglu et al., 2010). Thus, the rate of

AABW formation and the AABW properties are generally poorly matched with the observations (Russell et al., 2018). These biases limit the applicability of LR ESMs as a tool to enhance our understanding of the dynamics on the Antarctic shelf and their impact on the global circulation (via AABW formation), and to predict their change under anthropogenic climate change forcing. There are two common ways to improve the representation of the (sub-grid scale) overflow process in ocean models: either by increasing the ocean model horizontal resolution (e.g., to 0.1°), or by using a LR model with overflow parameterization (Danabasoglu et al., 2010; Price and Yang., 1998). The Community Earth System Model (CESM) tends to exhibit excessive convective entrainment in the DSW overflow process, which results in the “end-point” mixed overflow water product being too light and too shallow (Danabasoglu et al., 2010). The basic idea of the overflow parameterization is that, by using an empirical end-point entrainment model (Price and Yang., 1998), the convective entrainment can be calculated in a more realistic way. In this process, the overflow water plume will not encounter excessive mixing while descending down the continental slope such that the end-point product water ends up spreading at a more realistic depth (Price and Yang., 1998; Danabasoglu et al., 2010).

I will show in this Chapter that the HR CESM1.3 simulations (with 0.1° ocean model and without overflow parameterization) described earlier in my dissertation capture the main features of the continental shelf dynamics (though not fully because the resolution is still too coarse for a detailed representation of the overflow dynamics; Danabasoglu et al., 2010; Thompson et al., 2018), while the LR CESM1.3 simulations

(with 1° ocean model) also capture the overflow dynamics to some extent due to the overflow parameterization.

5.2 Bottom topography and potential vorticity conservation

Potential Vorticity (PV) conservation ($\frac{d}{dt} \left(\frac{f + \xi}{H} \right) = 0$, where ξ is relative vorticity, f is the Coriolis parameter, and H is the total water depth) constrains the ASC to position itself above the Antarctic shelf break (e.g., Brink 2016; Paloczy et al., 2020). In the high-latitude Southern Ocean, the magnitude of f is relatively large, but does not change greatly around the Antarctic margin. In $\xi = \frac{\partial v}{\partial x} - \frac{\partial u}{\partial y}$ the second term dominates in the mostly zonal flow of the ASC and describes the lateral shear associates with the ASC flowing along the coast or continental slope as a boundary current. Thus, the total water depth H ($H = \eta + h$, where η is the dynamic sea-surface height (also SSH), and h is the mean water depth) is the most important factor that balances $\frac{\partial u}{\partial y}$. Fig.5.1a shows the bathymetry of the HR ocean model. It represents the steep topography of the continental slope (around Antarctica from about 1000 m to 3000 m) very well. In the LR version, however, the slope is much gentler (Fig.5.1b versus Fig.5.1a). Thus, the ASC shear value ($\frac{\partial u}{\partial y}$) is higher in HR than in LR, and the ASC thus more confined along the Antarctic shelf break in HR. In this study, we choose the 1000 m isobath as the boundary of the Antarctic shelf region, as defined in previous studies (Dufour et al., 2017; Goddard et al., 2017; Lockwood et al., 2021).

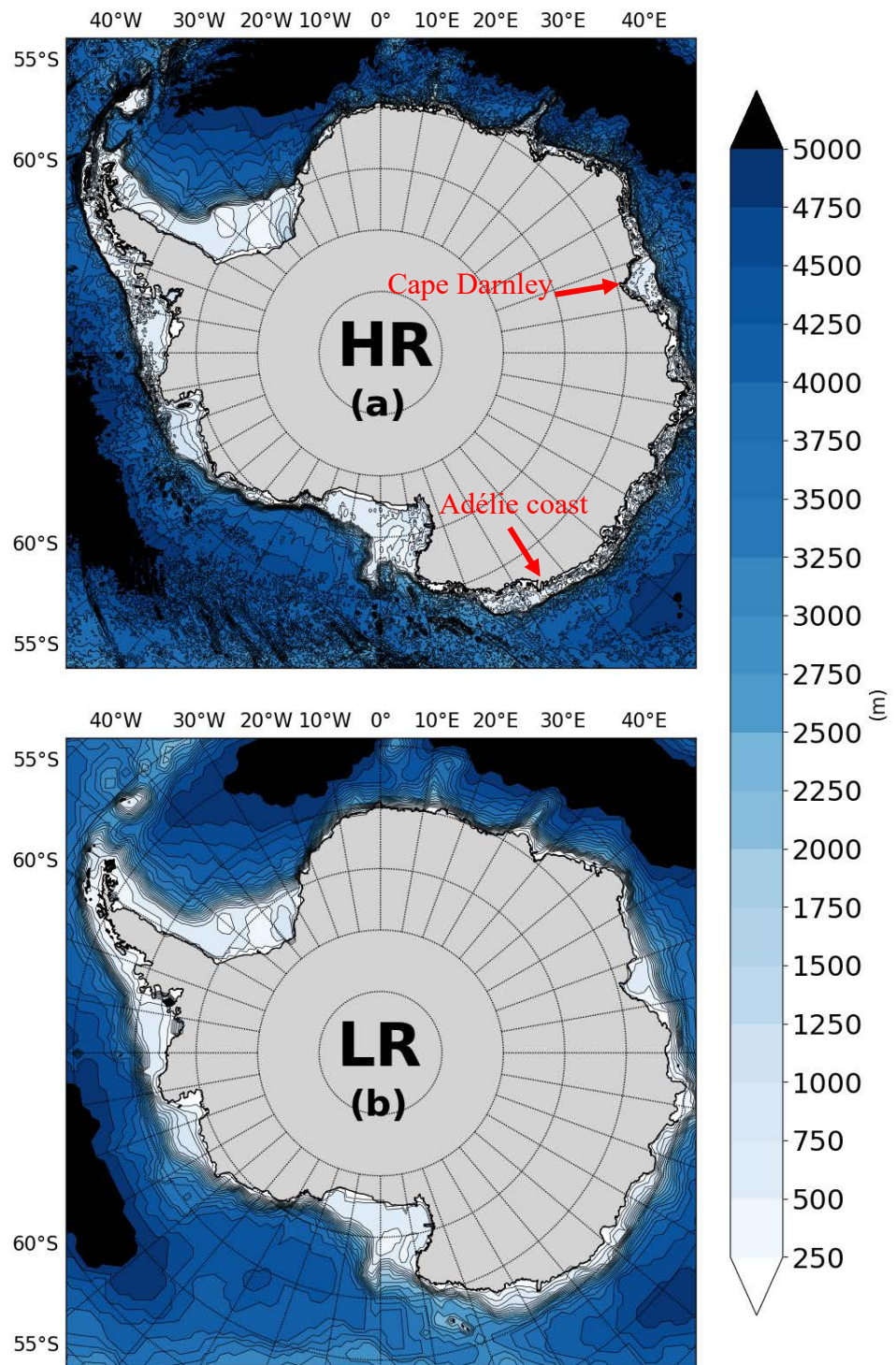


Figure 5.1. Model bathymetry around Antarctica, (a) high-resolution (HR), (b) low-resolution (LR).

5.3 Anthropogenic forcing influence on DSW overflow in HR and LR

Since the DSW formation and overflow process is strongest in winter, I restricted my analysis to September-mean model output and compared the last 50 years of the respective PI simulations (namely years 450-500) with those of the respective TN simulations (years 2050-2100). The September mixed-layer depth of the last 50 years of HR-PI and LR-PI (Fig.5.2, left panels) shows that DSW formation happens in four main regions (on shelf within purple boxes in Fig.5.2), matching well with where DSW formation has been observed: the western Ross Sea (Whitworth & Orsi, 2006; Gordon et al., 2009), the Weddell Sea (Gordon et al., 1993; Nicholls et al., 2009), the Adélie coast (Williams et al., 2010), and Cape Darnley (Ohshima et al., 2013). These four regions also coincide with locations where coastal polynyas typically emerge (Fig.5.3; see also Tamura et al., 2016). In coastal polynyas, sea ice remains very thin as newly formed ice is swiftly advected northward by offshore winds such that new ice is continuously being produced (Fig.5.3 and Fig.5.4; see also Stössel et al., 2011). Fig.5.5 shows that the highest thermodynamic ice growth is closely linked to the coastal polynyas and the offshore wind patterns. In these “ice factories” (Tamura et al., 2016) a lot of salt is added to the water over the continental shelf due to brine release. Both the relatively high salinity and the relatively low temperature (due to the direct contact with the frigid atmosphere combined with strong winds) render the surface water in the coastal polynyas dense enough to sink, which is reflected by mixed-layer depths exceeding 200 m (Fig.5.2). The sea ice formation and export are strongest in the southwestern Ross Sea (Jacobs et al., 2002), which matches with our simulation result as this is where the

offshore wind is strongest (Fig.5.4), the thermodynamic ice growth is largest (Fig.5.5), the coastal sea ice is thinnest (Fig.5.3), and the mixed layer is deepest (Fig.5.2). Regions of substantial sea ice formation and export are also located in the southwestern Weddell Sea, and Cape Darnley (Fig.5.3 and Fig.5.4). Comparing the left with the right panels of Fig.5.2, we can readily see that the anthropogenic forcing (right panels) will apparently shrink the area of shelf convection in these regions.

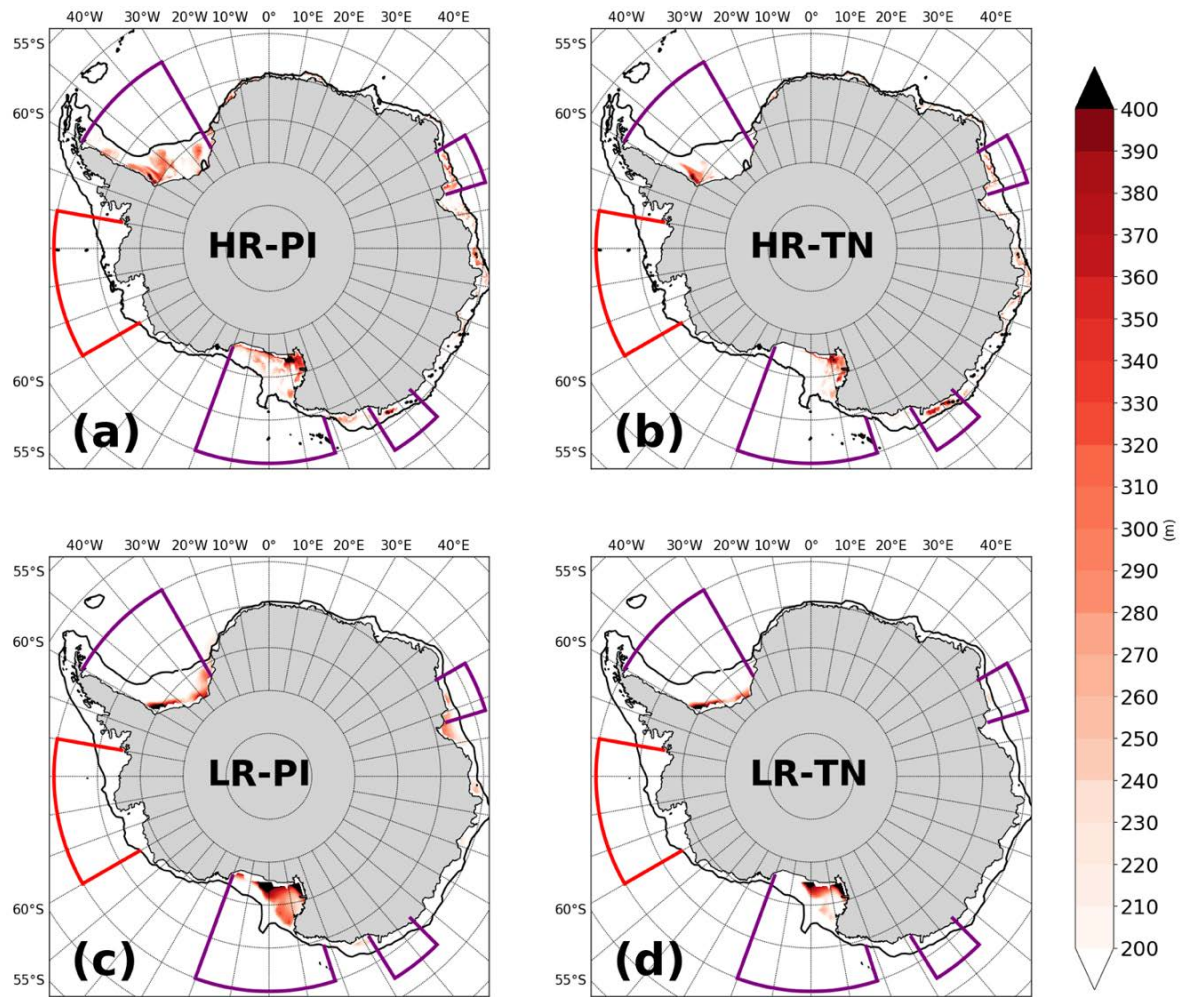


Figure 5.2. September mixed-layer depth over the Antarctic continental shelf. (a) Year 450-500 of HR-PI, (b) year 2050-2100 of HR-TN. (c) Year 450-500 of LR-PI, (d) year 2050-2100 of LR-TN. The characteristic Dense Shelf regime is normally found across the shelf break within the purple boxes, while that of the Warm Shelf regime within the red box. The shelf regions outside the boxes are mostly Fresh Shelf regimes.

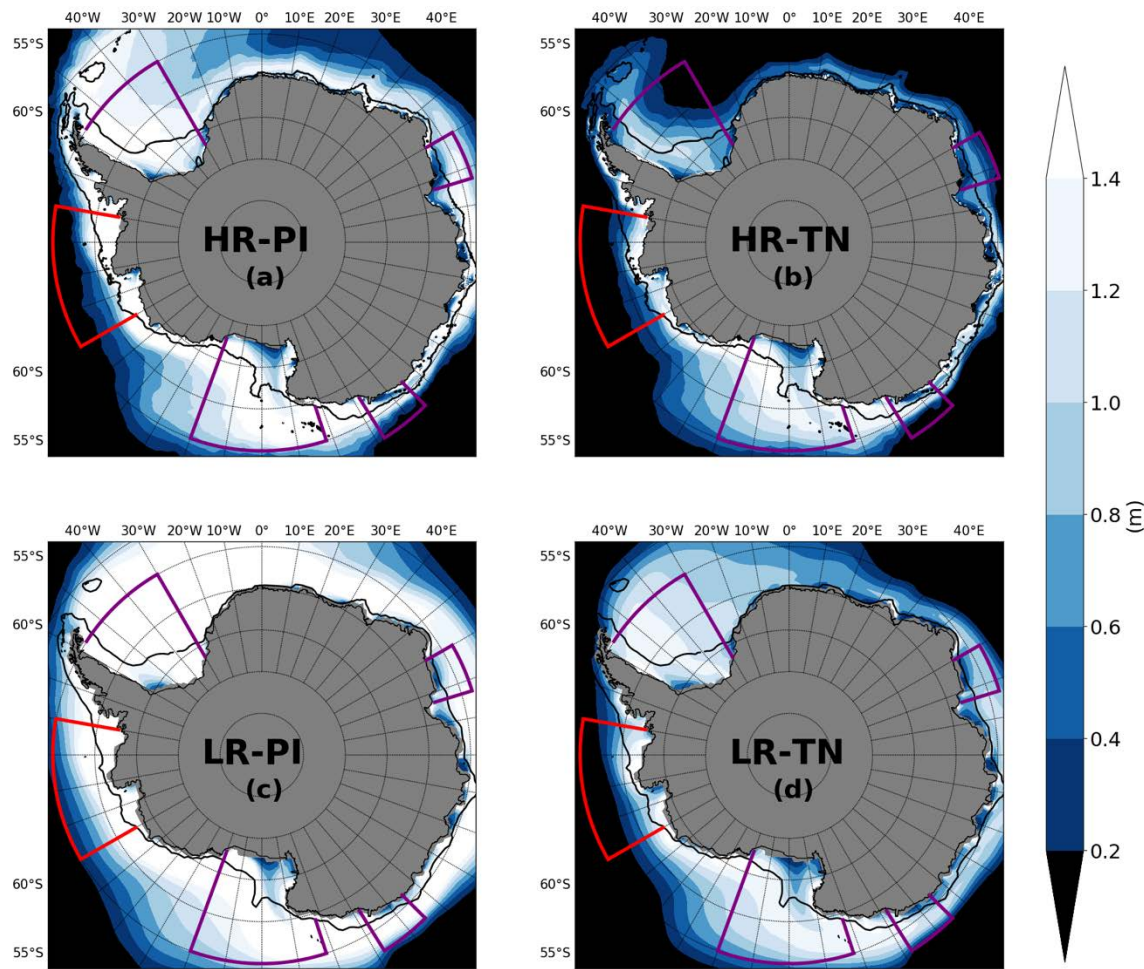


Figure 5.3. September sea ice thickness (with thin ice along the coast indicating coastal polynyas). Otherwise as Fig.5.2.

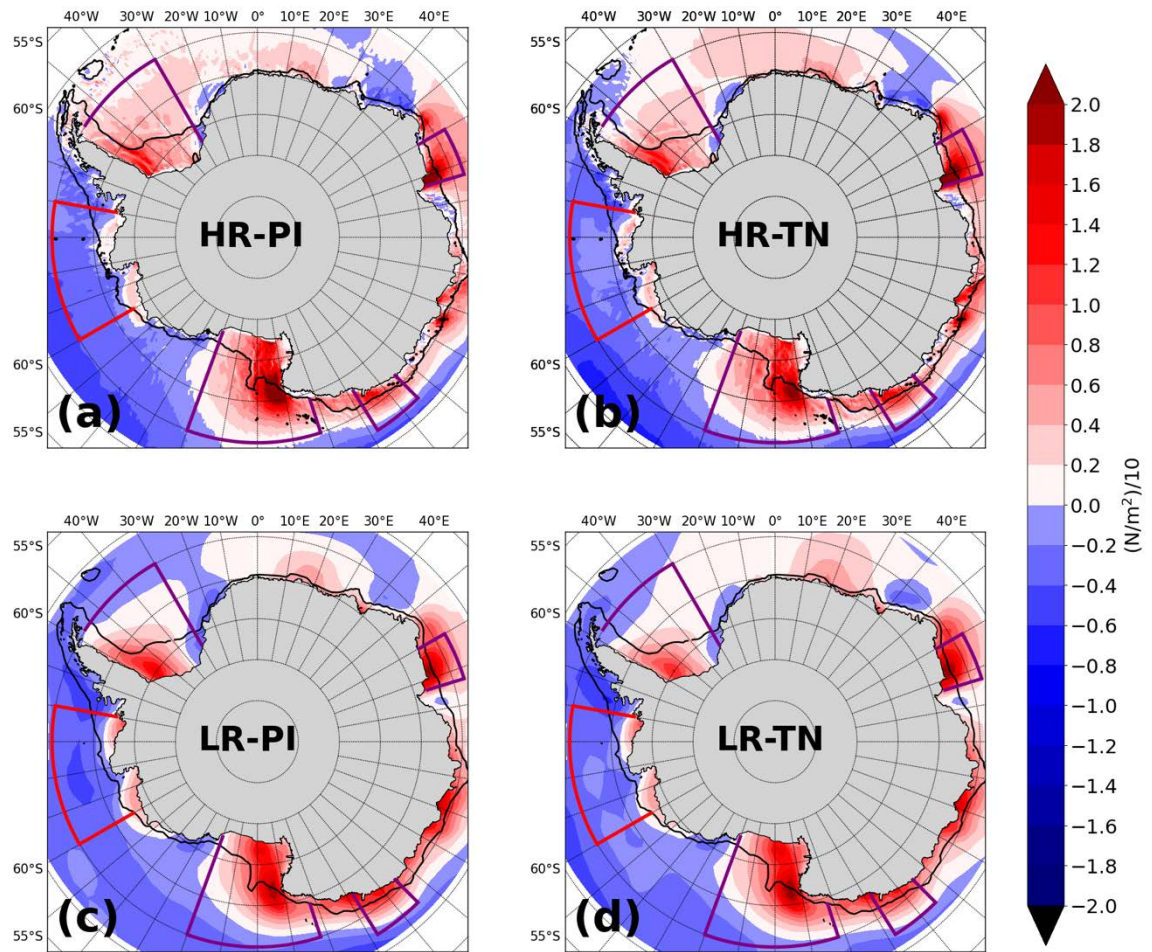


Figure 5.4. The September meridional components of wind stress, positive northward. Otherwise as Fig.5.2.

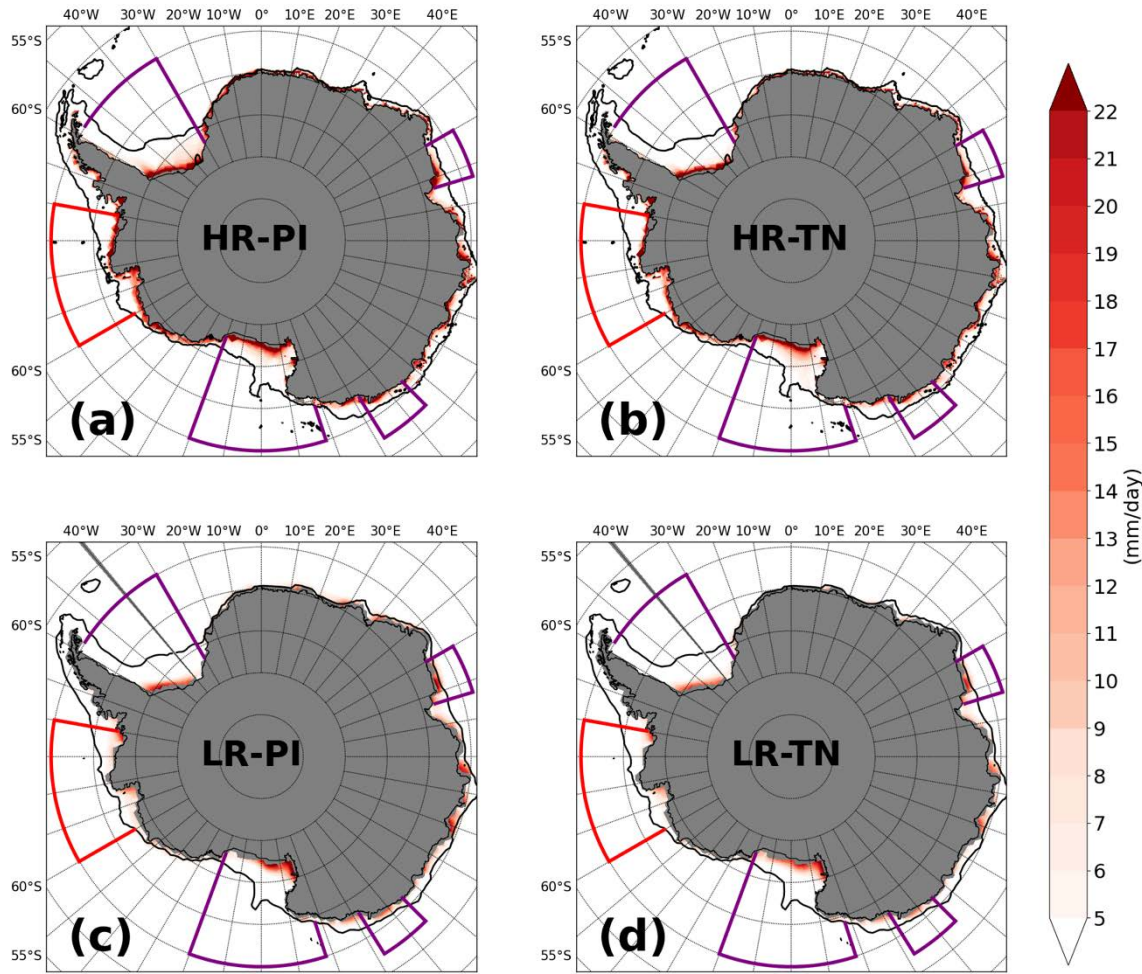


Figure 5.5. Annual thermodynamic ice growth (only showing values > 5 mm/day). Otherwise as Fig.5.2.

Fig.5.6a shows that HR-PI produces salinity in excess of 34.9 psu on the western Ross Sea shelf, which matches well with the observations of Orsi & Wiederwohl (2009) and Whitworth et al. (1998). The high salinity here is the result of both local and remote salt input to the ocean (Jendersie et al., 2018): local input comes from sea ice formation in the Terra Nova Bay polynya, and the remote input includes sea ice formation in the Ross Ice Shelf polynyas and on the broader continental shelf (Silvano et al., 2020; also Fig. 5.2a and Fig.5.5a). While LR-PI also produces high salinity water on the western

Ross Sea shelf, the value is much smaller than in both HR-PI and observations (about 34.82 psu; Fig.5.6c). In the other “dense shelf” regions (Weddell Sea, Adélie coast, and Cape Darnley) HR-PI can also produce relatively high salinity shelf waters (Fig.5.6a), with values of about 34.7 psu (consistent with Legg et al., 2009 and their Fig.11b in Whitworth et al., 1998). Comparing the right with the left panels of Fig.5.6, we can see that the anthropogenic forcing in HR-TN and LR-TN renders the water in all “dense shelf” regimes fresher, especially on the Ross Sea shelf. This tendency matches with the observation that the salinity over the bottom of the southwestern Ross Sea shelf decreased over the past four decades (Jacobs et al., 2002; Jacobs & Giulivi, 2010).

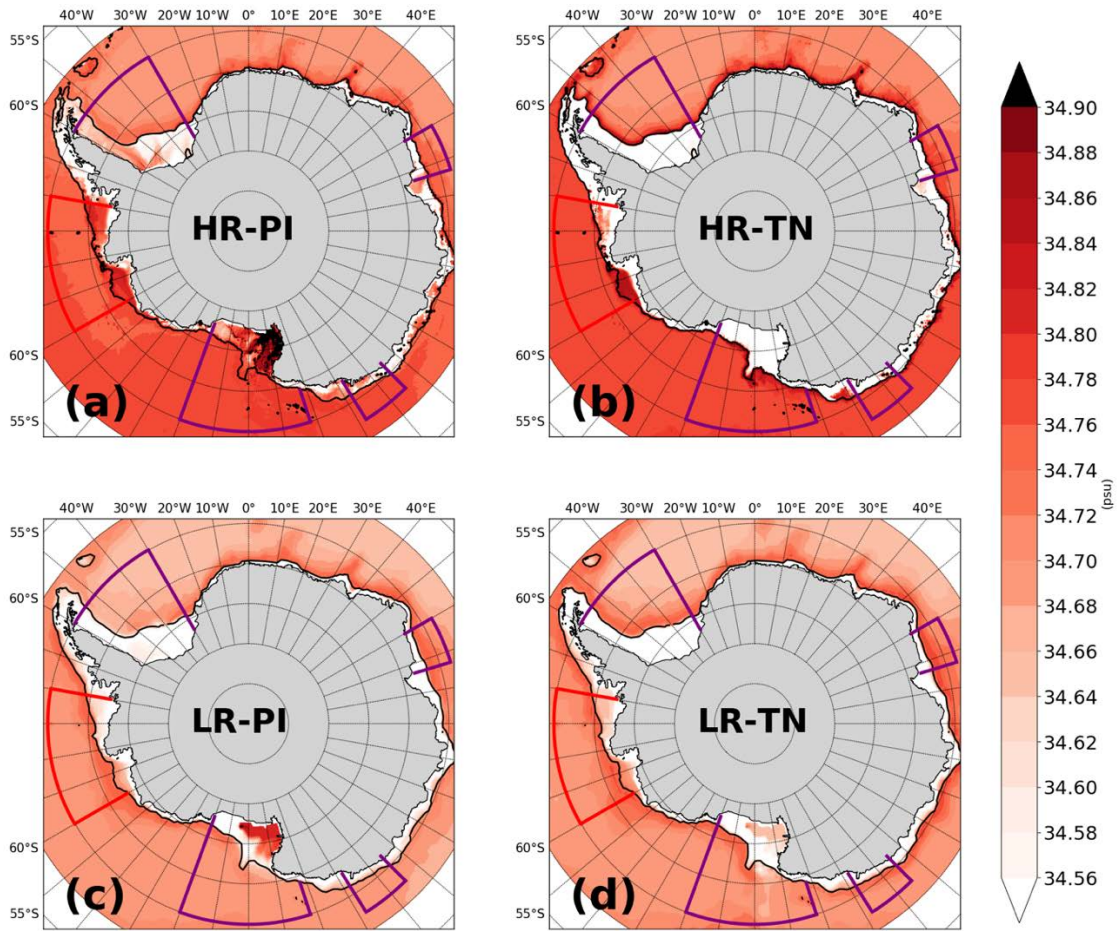


Figure 5.6. September-mean salinity of the bottom ocean model layer. Otherwise as Fig.5.2.

The bottom temperature of HR-PI and LR-PI (Fig.5.7, left panels) both capture the observed low temperature ($< -1.7^{\circ}\text{C}$; see Fig.11a of Whitworth et al., 1998) on the Ross Sea and Weddell Sea shelf reasonably well. However, HR-PI seems to simulate a substantially higher temperature than observed at the bottom of the off-shelf, deep Ross Sea (according to Legg et al., 2009 and Gordon et al., 2009 observed -1°C versus simulated $> 0^{\circ}\text{C}$; Fig.5.7a). One possible reason for this could be the excessive convective entrainment (Danabasoglu et al., 2010) described earlier in this chapter.

While the deep ocean bottom temperature of LR-PI is in the same range as HR-PI (-0.2~0°C), and thus also warmer than observed, it is slightly more realistic than in HR-PI. This is seemingly due to the colder temperature on the Ross Sea shelf in LR-PI. In the Weddell Sea, however, the HR-PI shelf bottom temperature matches with the observation result very well (< -0.6°C; Orsi et al., 1990), possibly due to the intermittent occurrence of open-ocean deep convection (and thus open-ocean polynyas) in HR-PI. In LR-PI, where open-ocean deep convection does not occur, the deep bottom temperature of the Weddell Sea is accordingly higher (-0.4°C to ~ -0.2°C).

Similar to the bottom salinity, the bottom temperature on the shelf also undergoes substantial changes under anthropogenic forcing. Due to the mixed layer becoming shallower (Fig.5.2, right panels), all four “dense shelf” regions become warmer (Fig.5.7). What’s more, the shelf bottom water in the Warm Shelf regime (red box region) is also getting warmer (> 1.6°C), which would accelerate the melting of the adjacent ice shelf from the bottom in this region in the real world (Moffat and Meredith, 2018; Gramling, 2021) and in the simulation if the underlying model (CESM1.3) had an ice shelf included. The deep ocean bottom temperature also gets warmer in both the Ross Sea and the Weddell Sea, possibly due to weaker DSW overflow (Ross Sea) and weaker open-ocean deep convection (Weddell Sea).

Another interesting feature is that, in HR, the shelf bottom water is relatively cold along the coast and surrounded by a ring of warmer water further offshore. This is possibly due to a better representation of the ASC on the shelf in HR. In the LR

simulations, this feature is absent, presumably due to the resolution being too low to resolve the ASC dynamics on the shelf.

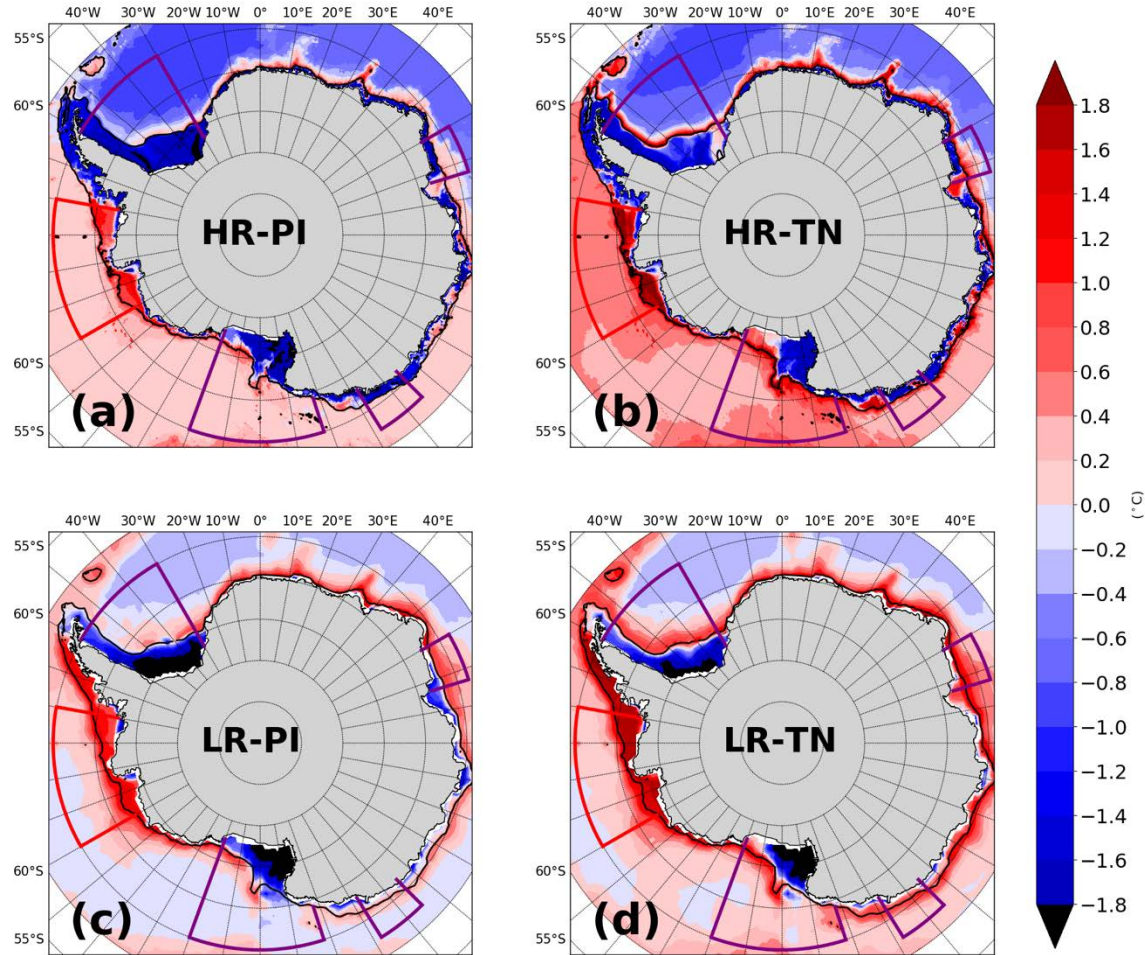


Figure 5.7. September potential temperature of deepest ocean model layer. Otherwise as Fig.5.2.

Both the freshening and warming of the bottom “dense shelf” water will decrease its density (Fig.5.8). In HR-PI, the high-density water is located on the shelves of the Ross Sea, the Weddell Sea, and partly along the Adélie Coast (Fig.5.8a), with the highest density in the western Ross Sea ($> 27.9 \text{ kg/m}^3$; matched with Legg et al., 2009). Note that the densities there are even higher than in the deep ocean beyond the continental

shelves; these are thus sites where we would expect DSW overflow to occur. In HR-PI, the DSW overflow process of the Ross Sea shelf region, with the pathway of high-density shelf water cascading down to the abyssal ocean, and then being transported eastward to the central Ross Sea, is clearly seen. In the Weddell Sea, on the other hand, the DSW pathway is not that clear (due to the potential density on the shelf and in the deep ocean being quite similar here). Based on the observation result of Gordon et al. (2004; 2009) and Gordon et al. (2020), two horizontal-vertical sections (the two yellow lines in Fig.5.8) were selected to investigate the DSW overflow in more detail later in Section 5.4. Finally, the anthropogenic forcing renders the Antarctic shelf water less dense in both HR-TN and LR-TN (mostly due to salinity decrease). When the shelf water potential density becomes smaller than that of the deep ocean, the DSW overflow comes to a halt (right panels in Fig.5.8).

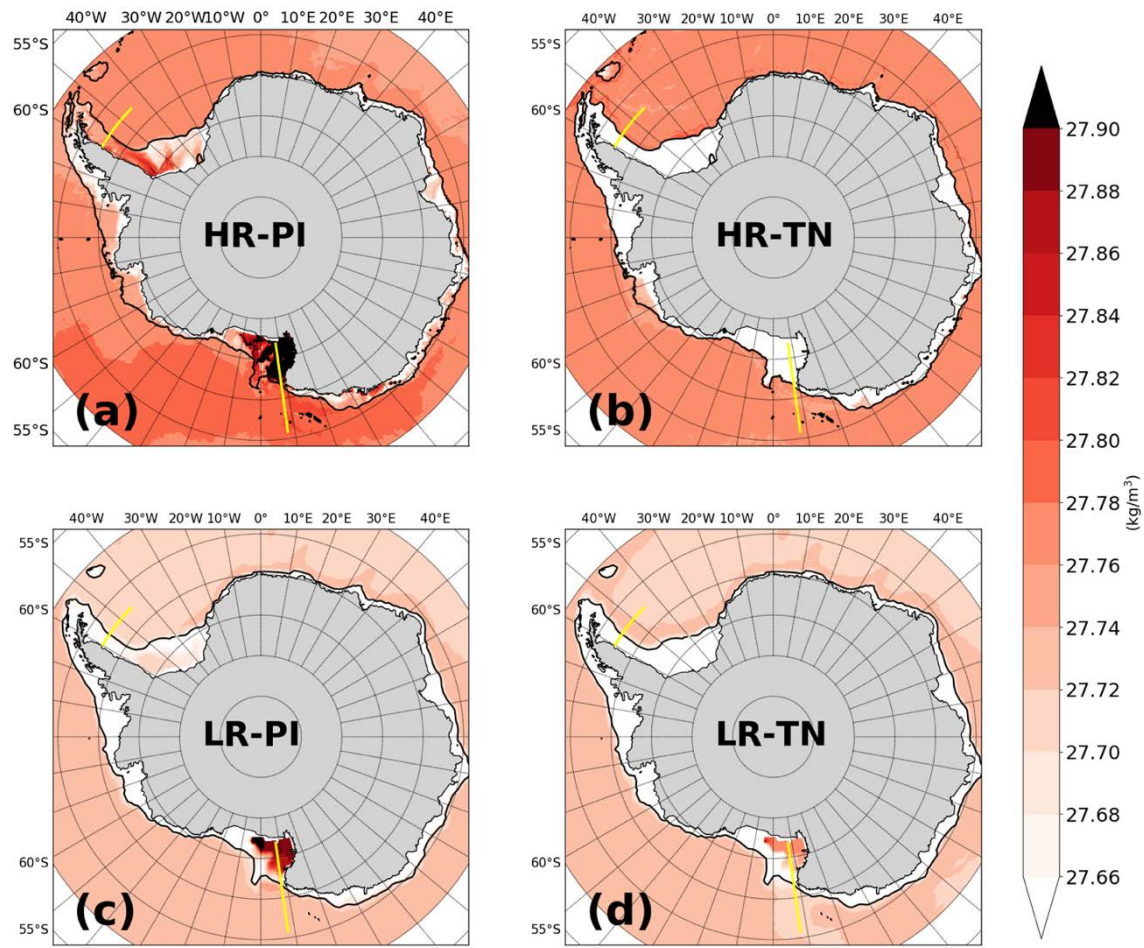


Figure 5.8. September potential density of deepest ocean model layer (calculated from potential temperature and salinity). Otherwise as Fig.5.2. The two yellow lines mark the sections being shown in Fig 5.11 and Fig.5.12.

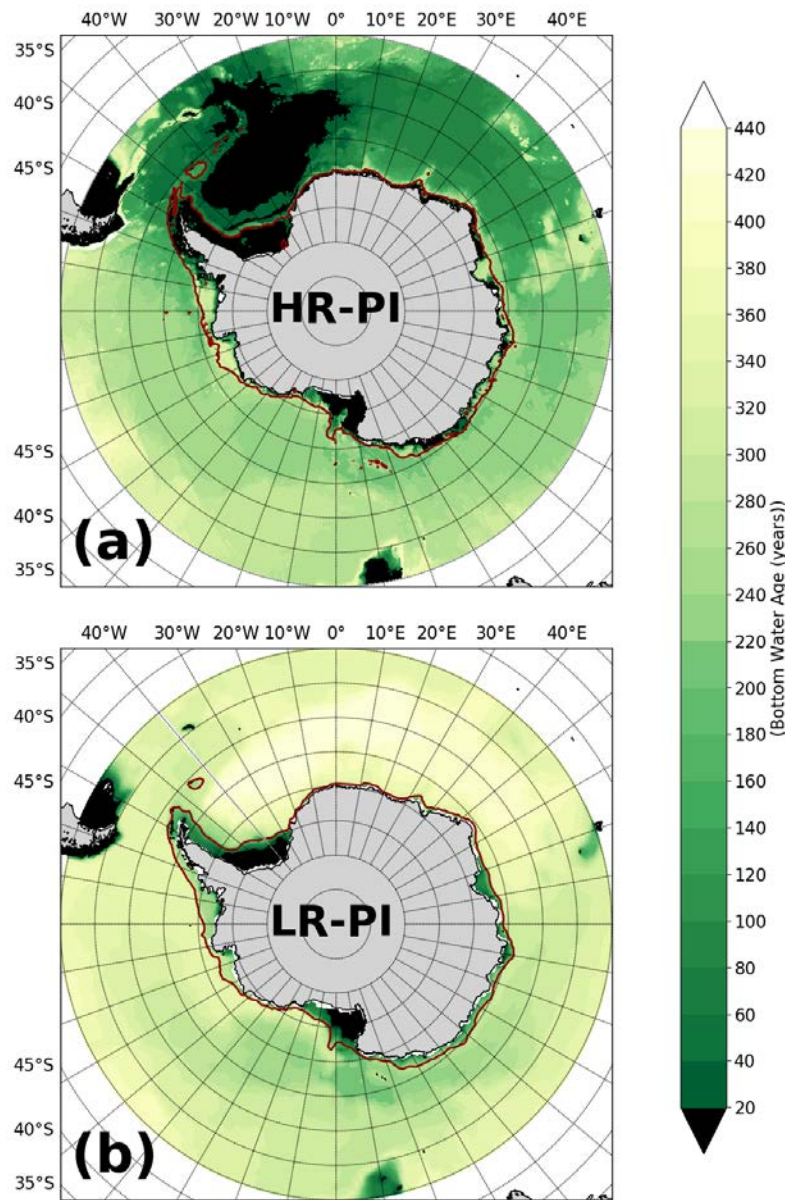


Figure 5.9. September water age of deepest ocean model layer. (a) Year 450-500 of HR-PI, (b) year 450-500 of LR-PI.

Fig.5.9 shows the water age tracer at the bottom ocean layer of HR-PI and LR-PI.

The water age tracer is defined to be set to zero when in the ocean surface cells, while it increases with time in the ocean internal cells. Thus, recently ventilated ocean bottom water will have a relatively young water age. In HR-PI (Fig.5.9a), both open ocean deep

convection (in the central Weddell Sea) and shelf convection contribute to making the bottom water age in the central Weddell Sea relatively young (less than 20 years old). Also, the continuous DSW formation process in coastal polynyas makes the shelf waters young (also less than 20 years old). Due to no OOPs occurring in LR-PI, its bottom water in the central Weddell Sea is very old (> 380 years, Fig.5.9b). In the central Ross Sea, the bottom water is relatively young in both HR-PI and LR-PI due to pronounced DSW overflow from the Ross Sea shelf (Fig. 5.9 a, b).

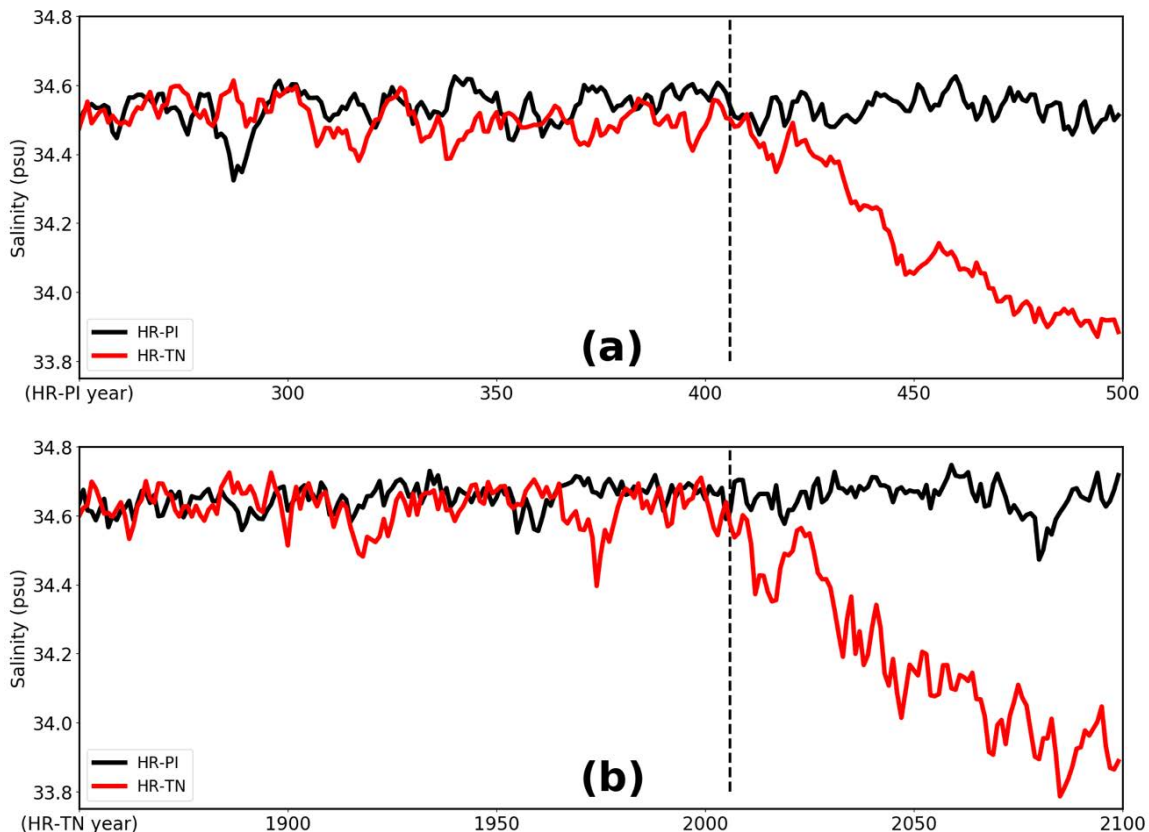


Figure 5.10. Timeseries of September water-column mean salinity of HR-PI (black) and HR-TN (red), averaged over (a) the Weddell Sea shelf region, (b) the Ross Sea shelf region. The dashed line is year 2006 (same as in Fig.4.1)

Observations show that the entire water column salinity in the Ross Sea shelf region has shifted toward lower values since the 1960s (Jacobs et al., 2002; their Fig.2). To follow up on this in the HR ESM simulations, I examined timeseries of the whole water column salinity on both the Weddell Sea shelf and Ross Sea shelf (Fig.5.10).

First, as expected, the Ross Sea shelf salinity is higher than that of the Weddell Sea and does not show a noticeable long-term trend in HR-PI. In HR-TN, on the other hand, the salinity values start decreasing under the climate change forcing, slowly under the history climate forcing while rapidly after the onset of the RCP8.5 climate forcing in year 2006 (black dashed line). Averaging over the period from 1960 to 2000, or from 1970 to 2010 of HR-TN, the trend is similar to the observed one (about -0.03 psu/decade; Jacobs et al., 2002; Jacobs & Giulivi, 2010; Schmidtko et al., 2014). After the onset of the RCP8.5 forcing in year 2006 (dashed line in Fig.5.10), the rate of decrease is much faster (-0.07 psu/decade in the Weddell Sea and -0.09 psu/decade in the Ross Sea). This suggests that the full RCP8.5 climate scenario effect on the Antarctic shelves had not yet been encountered over the time span over which the referenced observations have been made. The Weddell Sea shelf shows a similar rapidly freshening trend under the RCP8.5 climate forcing (Fig.5.10a) as the Ross Sea shelf (Fig.5.10b).

5.4 Change of characteristic property regimes

Following Thompson et al. (2018), Gordon et al., (2009), Gordon et al., (2020), and Orsi & Whitworth (2005), I selected three regimes with distinct characteristic water properties: the “Dense Shelf” regime, the “Fresh Shelf” regime, and the “Warm Shelf”

regime (see Chapter 1), to investigate how the anthropogenic forcing will influence the cross-slope dynamics of the ASC in each regime.

5.4.1. Dense Shelf regime

Fig. 5.11 shows the DSW overflow process in the Ross Sea shelf section (172°E, near the Drygalski Trough; see also Fig.1 of Gordon et al., 2009). The relatively cold (< 0 °C) and fresh (about 34.76 psu) DSW overflow bottom current plume that descends along the continental slope to the deep ocean is well captured in HR-PI (Fig.5.11a and Fig.5.11e). The results also match with the observation results of Gordon et al. (2009), their Fig.6. Furthermore, in HR-PI, we can clearly see that the DSW overflow is a salinity-controlled phenomenon (Fig.5.11e). The High Salinity Shelf Water (HSSW) produced in the coastal polynya accumulates on the shelf, which increases the water density. The DSW (also HSSW) accumulates on the Ross Sea shelf (with potential density in excess of 27.9 kg/m^3 and salinity in excess of 34.82 psu). After the DSW fills the marginal sea, the DSW starts overflowing. The overflow forms a density-driven bottom current that descends along the continental shelf break and slope to the deep ocean (Fig.5.11 a,e). While the DSW cascades down the slope, it mixes with the adjacent water mass (CDW) which lowers the density of the resulting product water, i.e., AABW (about 27.79 kg/m^3 ; observed 27.85 kg/m^3 according to Legg et al., 2009). In LR-PI, the DSW also accumulates on the Ross Sea shelf, but its density is lower than in HR-PI, commensurate with its lower salinity in LR-PI (about 34.76 psu in Fig.5.11g). Nevertheless, DSW overflow also occurs in LR-PI, presumably due to the overflow parameterization (Fig.5.11 c, g). However, the temperature and salinity gradients across

the ASF are much smaller and spread over a wider region in LR-PI than in HR-PI (as one would expect with a lower resolution).

Comparing the simulated bottom density (Fig.5.8 and Fig.5.11 a, c) with corresponding observed density values (e.g., Legg et al., 2009), we can see that even the HR simulations do not fully resolve the DSW overflow process (Dufour et al., 2017), and that too strong convective entrainment deteriorates the overflow process (Danabasoglu et al., 2010; Price and Yang., 1998). Adding the overflow parameterization in HR CESM1.3 may thus be crucial for a more realistic simulation of the overflow process. Another important effect of the overflow parameterization is that it will increase the stratification of the water column (Yeager and Danabasoglu, 2012; Dufour et al., 2017). Thus, we hypothesize that when adding an overflow parameterization to HR CESM1.3, the overproduction of open ocean polynyas in HR-PI may be reduced due to this stronger stratification effect.

In both HR-TN and LR-TN, the shelf water becomes much fresher, which eventually leads to the cessation of DSW production and thus DSW overflow (Fig.5.11f and Fig.5.11h). Furthermore, the cessation of the DSW overflow seems to originate at the surface (coastal polynyas), with the density (and salinity) of the surface water being reduced to the point that it cannot sink to the bottom of the shelf. With the lack of high-density “source” water production in both HR-TN and LR-TN, the DSW overflow ceases (the right panels in Fig.5.11). The lack of DSW overflow also leads to a deep heat and salt reservoir build up along the continental slope (right panels of Figs. 5.11). In

summary, all these changes will make the Ross Sea Dense Shelf section become more like a Fresh Shelf section under the anthropogenic forcing.

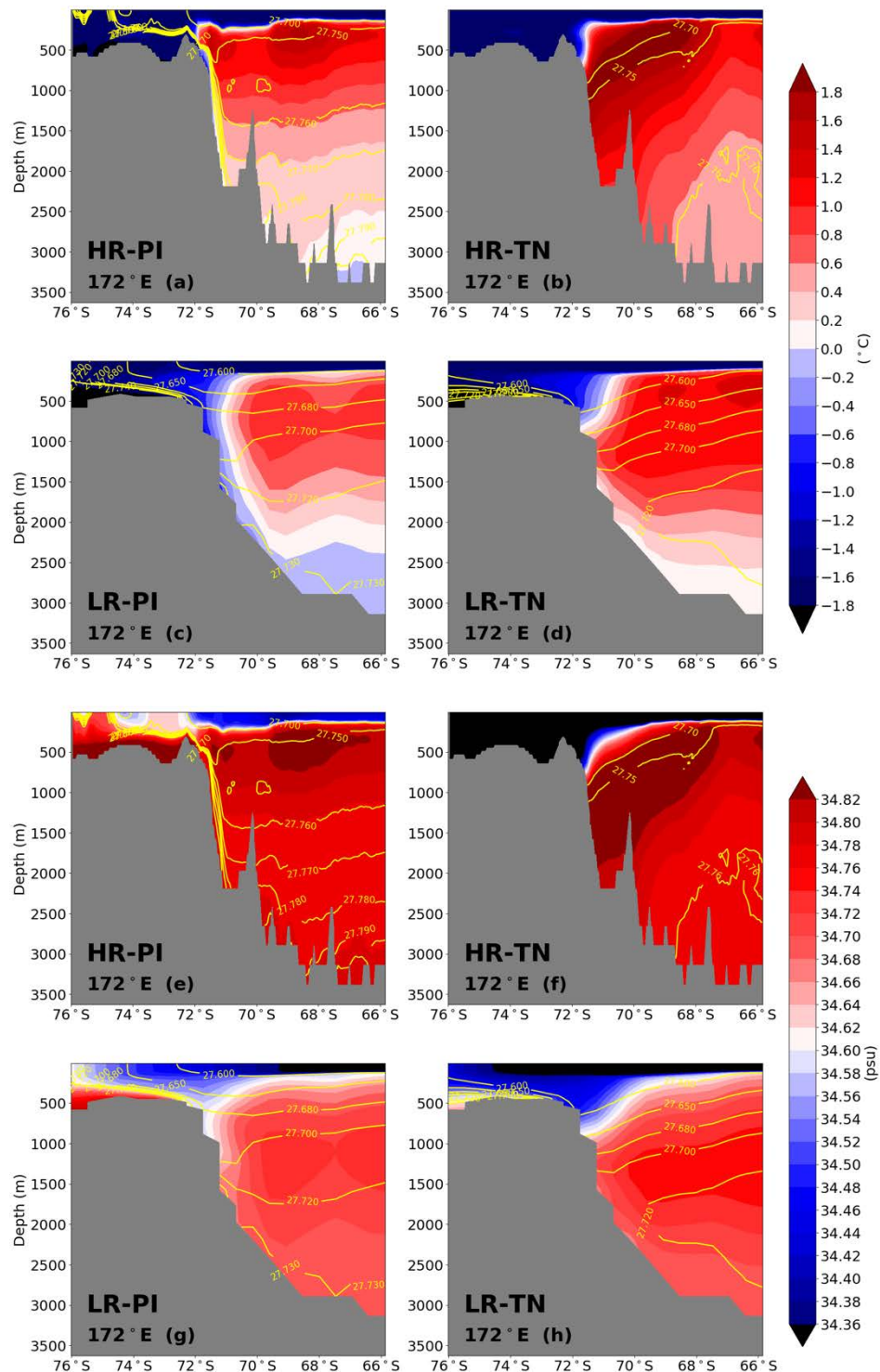


Figure 5.11. September potential temperature (upper panels), salinity (lower panels), and potential density (yellow contour lines) in the Ross Sea Dense Shelf section (172°E). Otherwise as Fig.5.2.

Fig.5.12 shows the DSW overflow process in the selected Dense Shelf section of the Weddell Sea (67.5°S ; matched with the observation section in Fig.1 of Gordon et al., 2020). The “V” shaped isopycnals are captured very well in HR-PI (Fig.5.12 a, e; see also Chapter 1.3), which indicates that DSW overflow also occurs in the Weddell Sea shelf region. In LR-PI, the “V” shaped isopycnals are practically absent, but DSW overflow seems to occur nevertheless, as indicated by the shape of the isopycnals (Fig.5.12 c, g). The temperature pattern in HR-PI matches well with the observation result of Gordon et al. (2020), their Fig.3, in that the low temperature water (less than -1°C) penetrates beyond 1000 m depth (Fig.5.12a). In LR-PI, on the other hand, although DSW overflow occurs, the pattern does not match very well with the same observation result, especially for the temperature gradient (Fig. 5.12c). The HR-PI salinity also matches well with the results of Gordon et al. (2020), with salinity larger than 34.64 psu on the Weddell Sea shelf. Furthermore, the “V” shape salinity lines are also in agreement with Whitworth et al. (1998) and Gordon et al. (2020) (Fig.5.12e). Although DSW overflow also happens in LR-PI, its simulated salinity does not capture the observed features very well (Fig.5.12f). In both HR-TN and LR-TN, the shelf water becomes much fresher, which eventually leads to the cessation of DSW overflow (the right panels in Fig.5.12). The anthropogenic forcing will gradually turn the Weddell Sea Dense Shelf section into a Fresh Shelf section, similarly to the simulated changes in the Ross Sea shelf section.

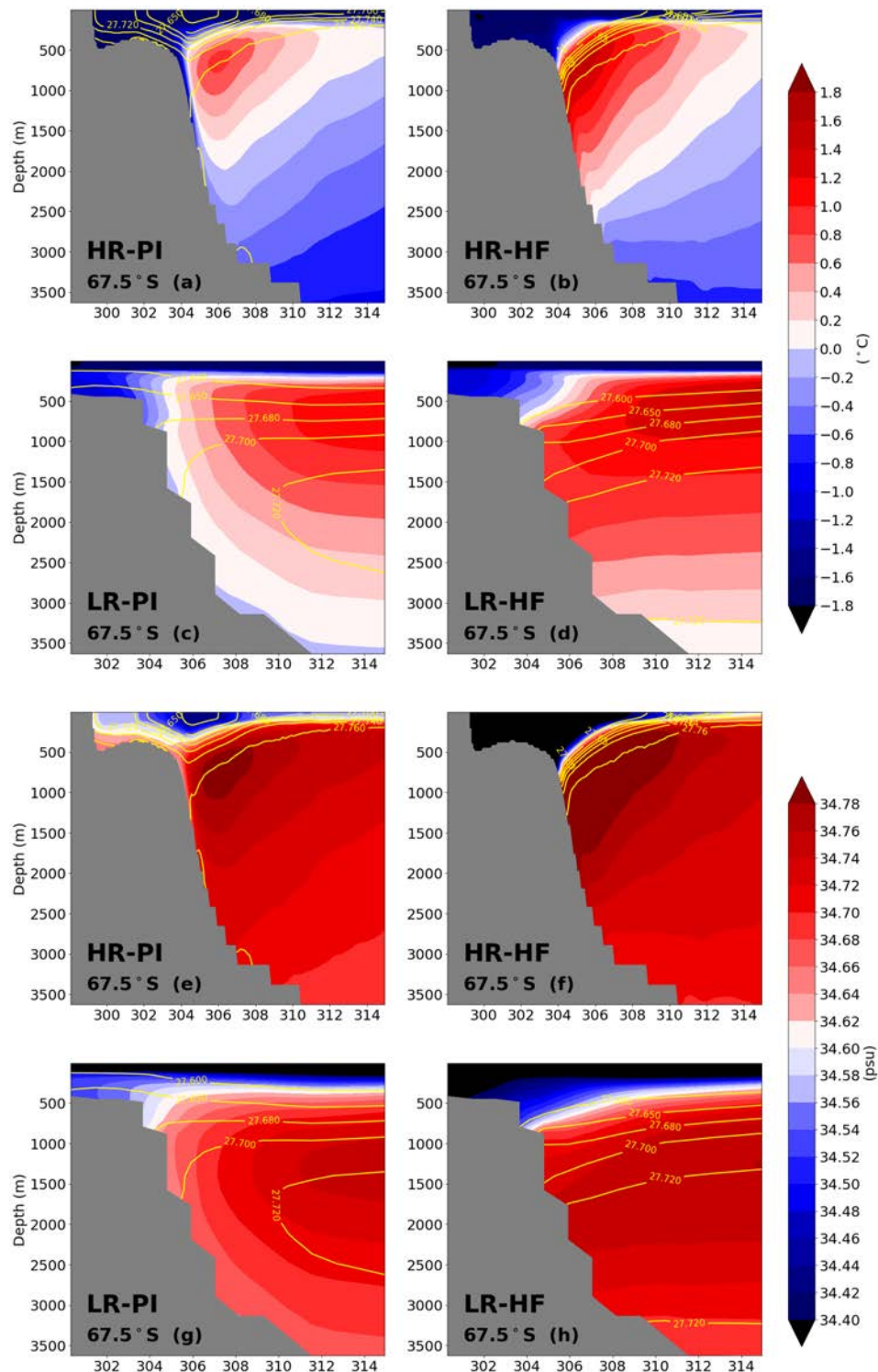


Figure 5.12. Weddell Sea Dense Shelf section (67.5°S). Otherwise as Fig.5.11.

5.4.2. Fresh Shelf regime

For the Fresh Shelf section (Fig.5.13), the temperature and salinity surfaces that tilt down from the surface toward the Antarctic continental slope are well captured in HR-PI (Fig.5.13a and Fig.5.13e; Orsi & Whitworth, 2005; Chavanne et al., 2010; Thompson et al., 2018). The strong ASC and the associated ASF here form an effective barrier for the cross-slope water exchange (Dong et al., 2016), by separating the cold and fresh shelf water from the warm and salty CDW offshore (Orsi & Whitworth, 2005). In LR-PI, the simulated isothermal (and isohaline) slopes of the Fresh Shelf section are much gentler (Fig.5.13c and Fig.5.13g), which is presumably due to the poor representation of the ASC in LR-PI.

The basic pattern does not change noticeably between PI and TN (Fig.5.13 left versus right panels). However, the salinity and temperature gradients across ASF are both increasing, which induces a much stronger stratification within the ASF. This reduces the lateral water mass exchange between the Antarctic shelf and the open ocean, and further isolates the shelf water south of the ASC; at the same time, due to the lack of CDW intrusion, the temperature and salinity reservoir of the CDW layer starts building up in both HR-TN and LR-TN (Fig.5.13b and Fig.5.13f).

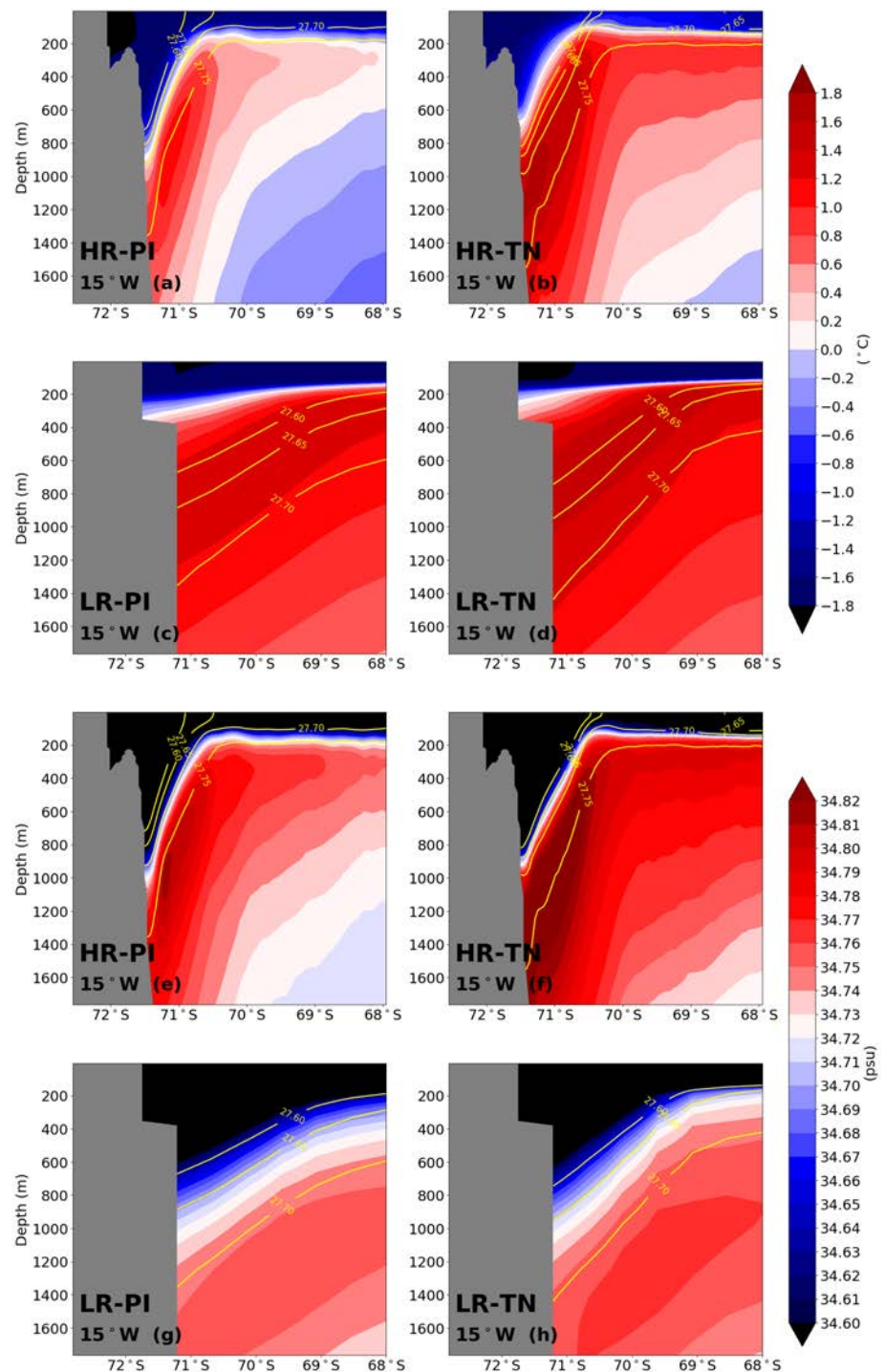


Figure 5.13. Fresh Shelf section (15°W). Otherwise as Fig. 5.11.

5.4.3. Warm Shelf regime

In the Warm Shelf section (Fig.5.14), the simulated CDW potential temperature of about 1°C and salinity about 34.70 psu of HR-PI reaches onto the Antarctic shelf, which matches with the observational results of Orsi & Whitworth (2005). Furthermore, the upward sloping pattern of CDW also correspond well with the observational findings (Schmidtko et al., 2014; Orsi & Whitworth, 2005). However, the simulated salinity of CDW in HR-PI is higher than reported on from observations by Orsi & Whitworth (2005) (the largest observed value in this region is 34.73 psu while it exceeds 34.82 psu in HR-PI). In LR-PI, the slopes of the isotherms and isohalines are much gentler compared to HR-PI and the observation results (Orsi & Whitworth., 2005; Fig.5.14c and Fig.5.14g), indicating the importance of high model resolution in this region.

HR-TN predicts a considerable freshening of the shelf water and a slight warming, thus rendering the shelf water more buoyant (Fig.5.14 b, f). LR-TN does not predict the same kind of change; on the contrary, the shelf water salinity is rather increasing (Fig.5.14h). At the same time, warmer water (CDW) penetrates onto the shelf (Fig. 5.14b, $> 1.4^{\circ}\text{C}$ for HR-TN; Fig. 5.14f, $> 1.6^{\circ}\text{C}$ for LR-TN). Overall, the Warm Shelf section will become warmer under the anthropogenic forcing in both HR-TN and LR-TN; at the same time, HR-TN is changing toward becoming a Fresh Shelf (matching with the conclusions of Moorman et al., 2020), while LR-TN does not seem to capture this freshening feature.

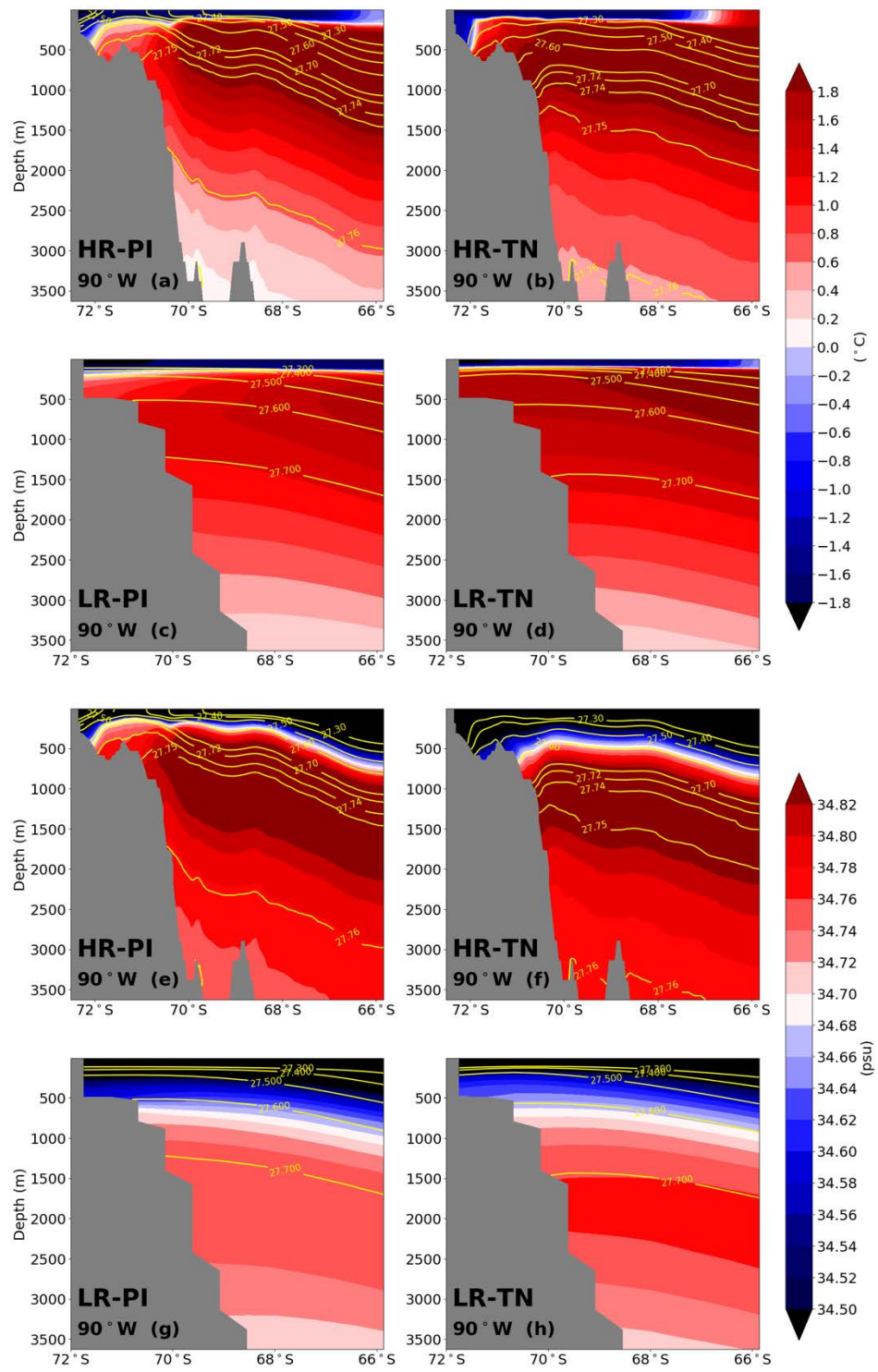


Figure 5.14. Warm Shelf section (88°W). Otherwise as Fig.5.11.

With the Antarctic shelf water becoming fresher in HR-TN (Fig.5.6, Fig. 5.11-5.14), the SSH over the Antarctic shelf region is increasing (Fig.5.15b versus Fig.5.15a). Lockwood et al. (2021) pointed out that the ASC restricts the lateral spreading of Antarctic shelf water. Thus, the net freshwater input is largely confined to the Antarctic shelf. At the same time, the DSW overflow-induced bottom current diminishes (Fig.5.8, Fig.5.11-5.12), which weakens the export of DSW from the Antarctic shelf; these effects all contribute to the increase of the SSH on the shelf. Due to the poleward shift of the Southern Hemisphere westerlies (as described in Chapter 4), the Weddell Gyre and the Ross Gyre both become stronger, which leads to a decrease of the SSH in the central Weddell Sea and Ross Sea (Fig.5.15b versus Fig.5.15a). The higher SSH on the Antarctic shelf and the lower SSH in the open ocean increases the meridional SSH gradient (Fig.5.15b versus Fig.5.15a). This, in turn, increases the ASC speed based on the thermal wind relationship in baroclinic geostrophic flow (Fig.5.16b). This increase of the ASC is also seen in the meridional-vertical sections displayed in Fig.5.17. The increased ASC will further confine the fresher water to the Antarctic shelf, and this positive feedback will make the Antarctic shelf waters become increasingly isolated from the open ocean in HR-TN. This also matches with the finding that the Fresh Shelf characteristic will gradually dominant.

In LR-TN, although the SSH in the central Weddell Sea and Ross Sea decreases as in HR-TN, the SSH on the Antarctic shelf does not increase; on the contrary, in LR-TN, the latter actually decreases (Fig.5.15d versus Fig.5.15c). The narrow ASC structure is poorly represented in the LR simulations, but the ASC apparently strengthens and

widens in LR-TN (Fig.5.16d versus Fig.5.16c). The different response of the HR and the LR simulations to the same anthropogenic forcing highlights the importance of HR for capturing shelf processes around Antarctica in ESM simulations; it also highlights that sub-grid-scale parameterizations targeted at improving shelf-slope processes in LR simulations may not provide an adequate substitution for HR simulations (Danabasoglu et al., 2010; Dufour et al. 2017).

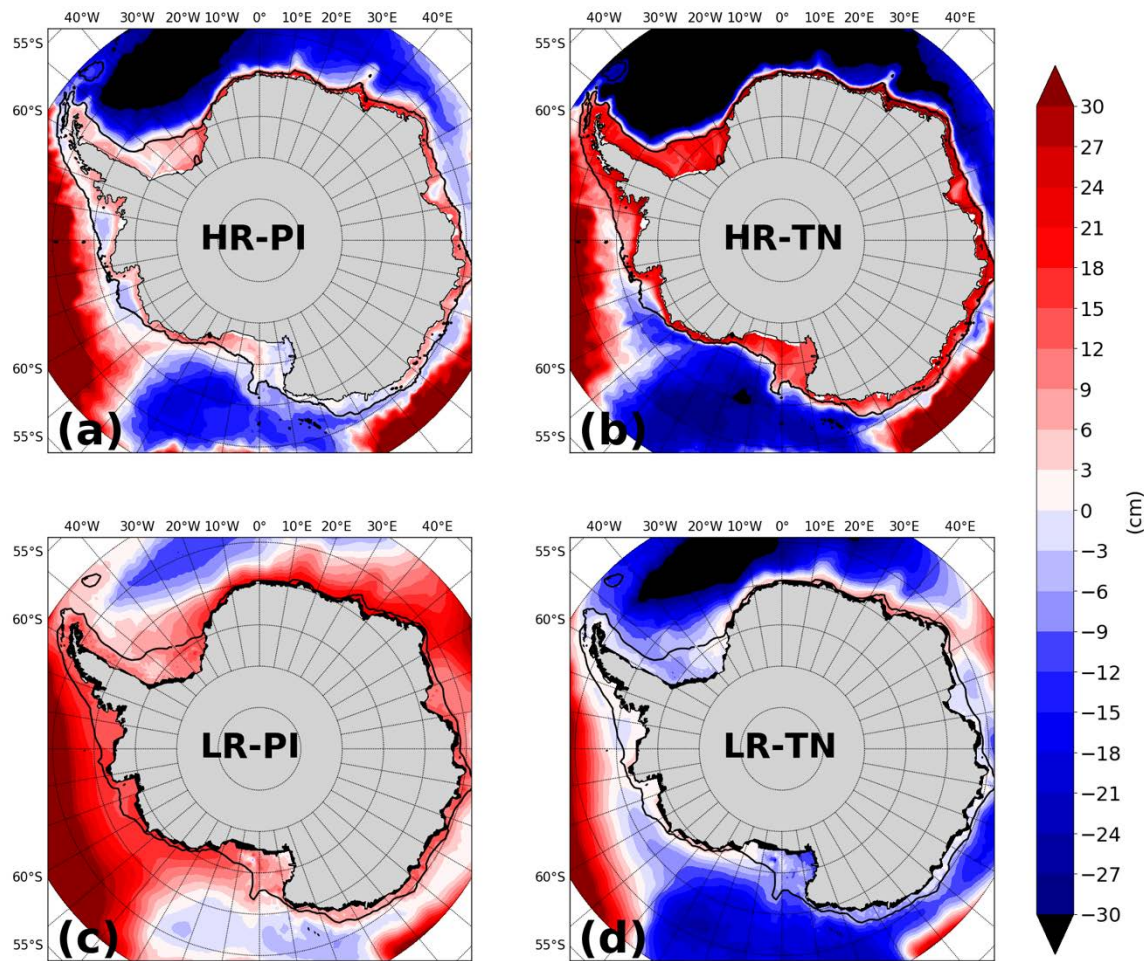


Figure 5.15. September sea-surface height (SSH). Otherwise as Fig.5.2.

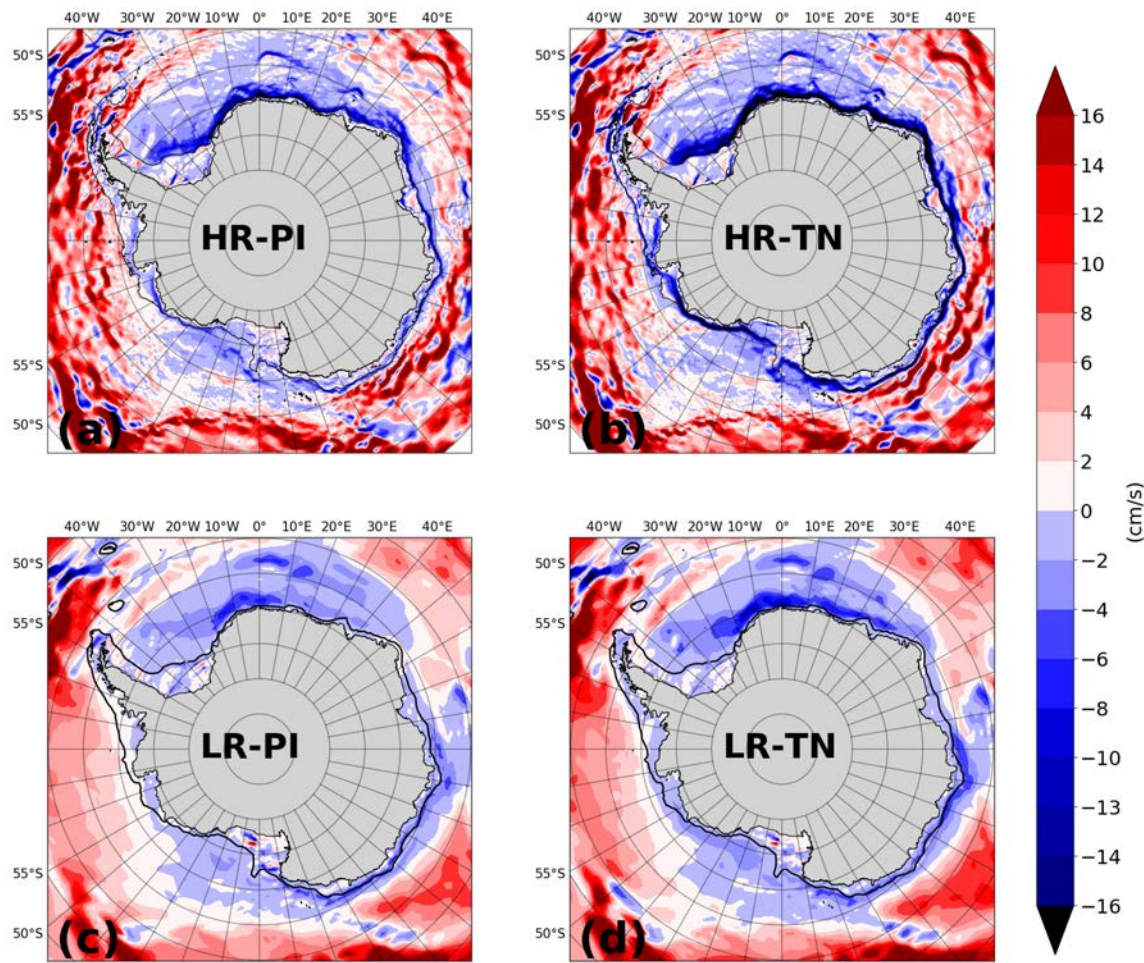


Figure 5.16. September zonal speed of Antarctic Slope Current. Otherwise as Fig.5.2.

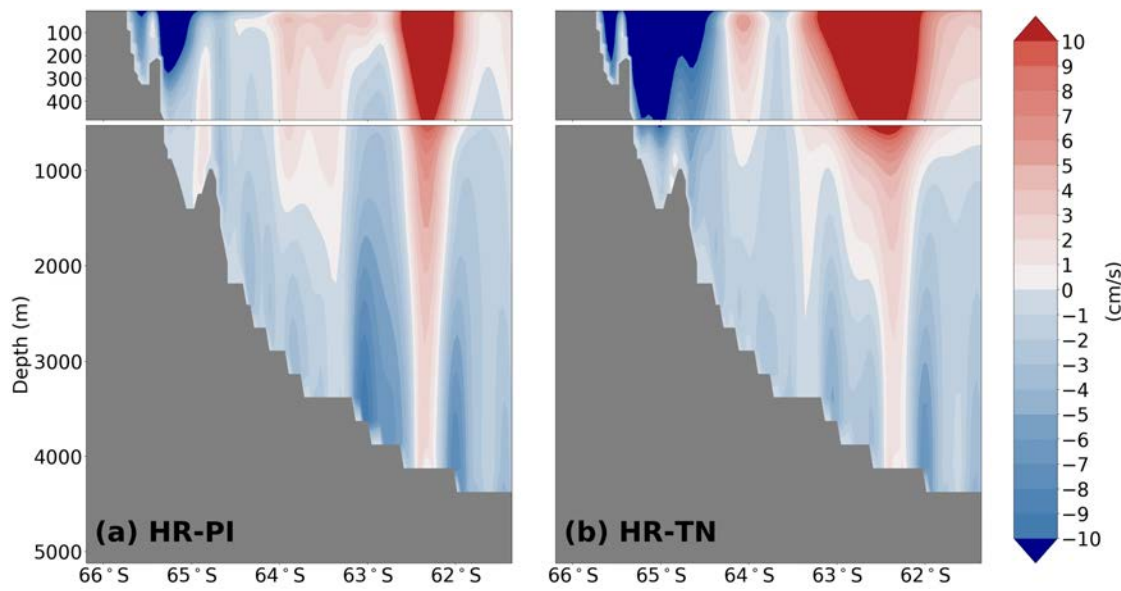


Figure 5.17. September zonal velocity vertical section along 113.3°E. (a) Year 450-500 of HR-PI, (b) year 2050-2100 of HR-TN.

5.5 Reasons for the salinity decrease on the Antarctic shelves

Both observations and simulations show that the shelf water freshening can be attributed to a combination of factors, including (1) reduced sea ice production, (2) increased precipitation, and (3) increased melting of the Antarctic Ice Sheet (e.g., Rignot et al., 2018; Jacobs et al., 2002; Jacobs & Giulivi, 2010; Lockwood et al., 2021). Concerning factor (3), CESM1.3 does not include an ice sheet or ice shelf model. Any contribution from “glacial meltwater” is instead crudely represented as an instantaneous freshwater runoff from the Antarctic continent.

Similar to the upper ocean salinity change analysis in association with the periodic occurrence of WSPs in HR-PI discussed in Chapter 3, we first analyze the salinity change induced by a change of sea ice production along the Antarctic coast, i.e., mainly in association with the occurrence of coastal polynyas. If the thermodynamic sea

ice production diminishes, so will the associated brine rejection, which in turn will decrease the shelf water salinity. Fig. 5.18 shows the annual thermodynamic sea ice production difference between TN and PI for both HR (Fig. 5.18a) and LR (Fig. 5.18b). Overall, there is less net thermodynamic sea ice production along the coast in TN than in PI, thus leading to less brine rejection and thus contributing to the fresher water on the Antarctic shelf regions. We also find that the net thermodynamic sea ice production is very sensitive to the wind forcing (especially in the Ross Sea shelf region; Fig. 5.18); this may be the reason for some small areas with positive anomalies along the coast (Fig. 5.18c and Fig. 5.18d).

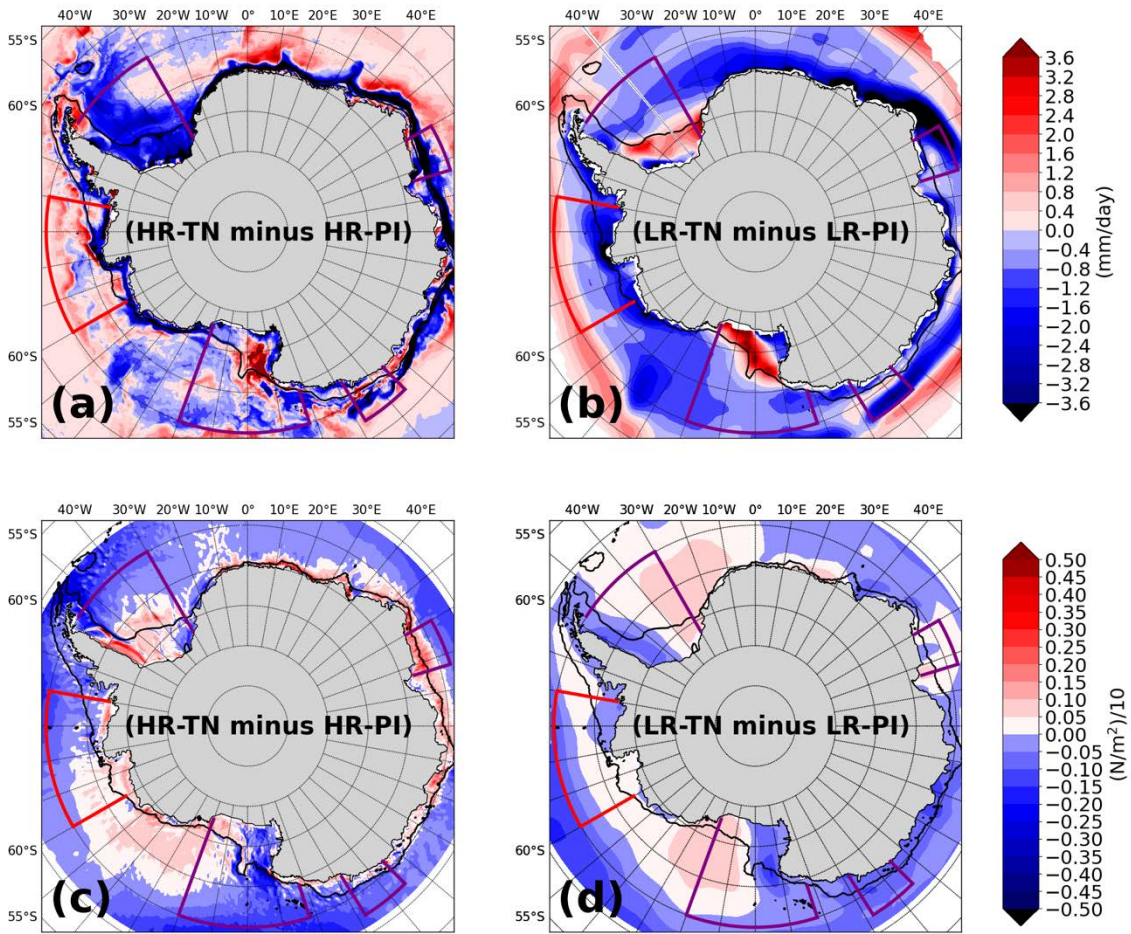


Figure 5.18. Annual thermodynamic ice production difference between (a) HR-TN and HR-PI, (b) between LR-TN and LR-PI. (Fig. 5.5 right panel minus left panel). Annual mean meridional wind stress difference between (c) HR-TN and HR-PI, (d) between LR-TN and LR-PI. (Fig. 5.4 right panel minus left panel).

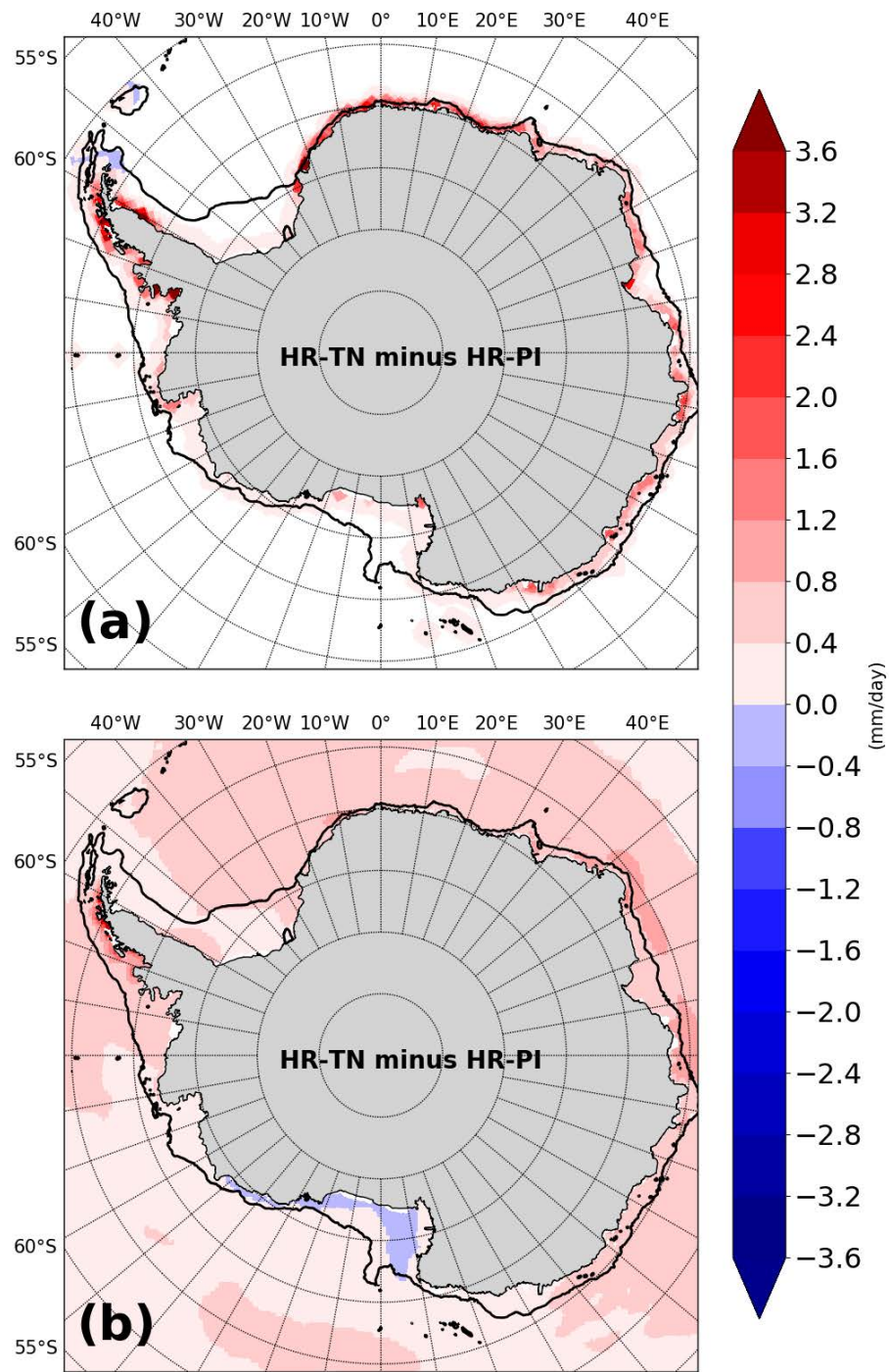


Figure 5.19. (a) Annual Antarctic freshwater runoff difference between HR-TN and HR-PI. (b) Annual precipitation difference between HR-TN and HR-PI.

Fig.5.19a shows the difference of spatial distribution of freshwater runoff from the Antarctic continent between HR-TN and HR-PI. The runoff increases mostly in the lower latitude regions of the Antarctic continent, which is seemingly due to the poleward movement of the precipitation-rich Southern Hemisphere westerlies under the RCP8.5 climate forcing (see Chapter 4), while there is very little runoff increase in both Weddell Sea and Ross Sea shelf region. As illustrated in Fig.5.19b, in HR-TN, the precipitation increases almost everywhere in the Southern Ocean region. However, there are also distinct regional anomalies to this trend with smaller and even negative values on the Ross Sea shelf region. Overall, the decrease of sea-ice production (equivalent to about 3.6 mm less ice production per day) in the Ross Sea and Weddell Sea shelf regions seems to be the most important contributor to the freshening of the shelf water in HR-TN, while both the increase of runoff from the Antarctic continent (about 1.2 mm per day), and the increase of total precipitation (about 0.8 mm per day) in the Southern Ocean seems less important in this simulation, especially in the Ross Sea shelf region (Fig.5.19a and Fig.5.19b).

5.6 Summary and conclusion

In this chapter, I investigated the possible anthropogenic impact on the ASC and on the DSW overflow in both HR and in both LR CESM1.3 simulations, respectively. The main conclusion of this study is that the DSW overflow induced by shelf-slope convection will cease in the future if the anthropogenic climate change forcing follows

the RCP8.5 scenario. My study also leads to the following summary and more detailed conclusions:

- (1) In both HR-PI and LR-PI, the generation of AABW from DSW overflow are partly captured. HR-PI captures the DSW overflow process better than LR-PI, even though the latter includes an overflow parameterization. The reason is possibly due to HR-PI simulating the formation of HSSW more realistically (especially in the Ross Sea region), while the salinity of the HSSW produced in LR-PI is too low compared to the observed values.
- (2) The “end of point” product water potential density in the Ross Sea is lower in both HR-PI and LR-PI than derived from observations (Legg et al., 2009); in HR-PI, this is possibly due to the too strong convective entrainment (Danabasoglu et al., 2010). In the Weddell Sea, the potential density of the product water of HR-PI matches well with the observations (about 27.75; Legg et al., 2009), however, due to shelf-slope and open-ocean convection happening simultaneously in the Weddell Sea, the contribution of each is hard to distinguish. LR-PI has a lower-than-observed bottom potential density in the Weddell Sea due to the lack of open-ocean convection. This indicates that the more realistic product water density in HR-PI is solely due to the contribution from open-ocean convection, and not due to a better representation of shelf-slope convection.

- (3) In both HR-TN and LR-TN, the generation of AABW from DSW overflow ceases under the anthropogenic forcing as the shelf water becomes more buoyant.
- (4) The more buoyant shelf water in HR-TN and LR-TN is mostly attributed to a reduction of sea ice formation, and to a lesser extent to an overall increase of freshwater runoff from the Antarctic continent and increased precipitation over the Southern Ocean.
- (5) Most freshwater input being confined to the Antarctic shelf region results in an increase of the sea surface height (SSH) along most of the coast of Antarctica. At the same time, due to the poleward shift of the Southern Hemisphere westerlies, the (cyclonic) gyre circulations of the Weddell and Ross Sea increase, leading to lower SSH in the central Weddell Sea and Ross Sea. The resulting steeper meridional SSH gradient increases the ASC, which further confines the freshened water to the shelf. This positive feedback will make the Antarctic shelf waters become increasingly isolated from the open ocean under anthropogenic forcing.
- (6) Finally, the accelerating westward ASC and the increased near-surface stratification will turn the “Dense Shelf” and the “Warm Shelf” regimes gradually into a “Fresh Shelf” regime under anthropogenic forcing.

Overall, an accurate representation of the Antarctic shelf dynamics and the DSW overflow process is key to achieving a reasonable simulation of the global

(thermohaline) overturning circulation and of the water properties of the deep ocean, as they determine the AABW production rate and properties. In this chapter, I showed that both the HR CESM1.3 simulations without the overflow parameterization and the LR CESM1.3 simulations with overflow parameterization can partly capture the DSW overflow process. HR-PI simulates the HSSW properties reasonably well, thus capturing the DSW overflow process much better than in LR-PI. Due to the excessive convective entrainment without overflow parameterization (Danabasoglu et al., 2010), the product water potential density of HR-PI is still lower than observed (especially in the Ross Sea). For future studies, I propose to investigate the hypothesis that employing the overflow parameterization in HR CESM1.3 simulations will improve the representation of the DSW overflow process. The advantages may include: (1) a reduction of the deep ocean model drift due to a more realistic AABW production rate and AABW properties; (2) a reduction of the overproduction of open-ocean polynyas due to the stratification of the water column getting enhanced; (3) a better representation of the on- and offshore water transport, which in turn will improve the interaction of the ocean with ice shelves in future CESM versions where such are included.

CHAPTER VI CONCLUSIONS AND FUTURE WORKS

In this dissertation, based on a pair of 500 year-long high-resolution preindustrial (HR-PI) and 250 year-long historical and future transient (HR-TN) Community Earth System Model (CESM1.3) simulations, and a pair of corresponding low-resolution CESM1.3 simulations that include eddy and overflow parameterizations (LR-PI and LR-TN), I studied: (1) the intermittent occurrence of OOPs in HR-PI; (2) the anthropogenic impact on the occurrence of OOPs and the associated open-ocean deep convection in HR-TN; and (3) the anthropogenic impact on the ASC and the DSW overflow in both HR and LR. Overall, I found that the anthropogenic impact will suppress both the open-ocean deep convection and the DSW overflow process, which is partly consistent with the recently observed trends (De Lavergne et al., 2014; Jacobs & Giulivi., 2010; Menezes et al., 2017). These two ocean convection processes are the main source of AABW production (Gordon., 2014), which also regulates the heat uptake, the water-mass transformation, the CO₂ exchange, and the nutrient transport (Vreugdenhil & Gayen., 2021). Thus, a shutdown of AABW formation under the RCP8.5 anthropogenic forcing would have crucial implications for both global ocean dynamics and climate change.

6.1 Conclusions

First, in HR-PI, the (regional) SAM index does not have a clear trend, oscillating only around its mean value; this provides a suitable environment for studying the

intermittent occurrence of OOPs. In the associated chapter, I proposed a new possible ocean-atmosphere coupling mechanism to explain both the near-periodic occurrence of OOPs and at the same time, the near-periodic change of the regional SAM index. The regional SAM index regulates the meridional movement of the precipitation-rich westerly winds, which then determine the upper-ocean stratification. The OOPs tend to more likely occur when the upper-ocean stratification is low, while OOPs are more likely to close when the stratification is high. At the same time, when an OOP (especially a WSP) opens, it will reduce the sea level pressure above it, which can also feedback to, and change, the regional SAM index. This closes the coupled atmosphere-ice-ocean mechanism loop.

Second, in HR-TN, the anthropogenic forcing will make the (regional) SAM index become more positive. The associated poleward movement of the precipitation-rich Southern Hemisphere westerlies will bring more freshwater and heat to the central Weddell Sea region. At the same time, less sea ice forms due to the higher air temperature. Both processes will increase the stratification in the central Weddell Sea, which suppresses open ocean deep convection and the return of WSPs. However, shallow convection continues to occur intermittently over and around the Maud Rise seamount, even though this region turns ice-free in winter. These patterns are consistent with the observation results that WSPs did not form since the last observed one in 1976 while MRPs still emerged intermittently since then (Vreugdenhil & Gayen, 2021). Another striking feature is that the zonal asymmetry of the poleward movement of the

westerlies will strongly influence the winter sea-ice extent in the Weddell Sea, while that of the Ross Sea is less affected.

Third, I investigated the anthropogenic impact on ASC and DSW overflow in both HR and LR. In HR-PI and LR-PI, the generation of AABW from DSW overflow both are partly captured. HR-PI captures the DSW overflow process better than LR-PI, even though the latter includes an overflow parameterization. The reason is possibly due to HR-PI simulating the formation of HSSW more realistically (especially in the Ross Sea region), while the salinity of the HSSW produced in LR-PI is too low compared to observations. In HR-TN and LR-TN, the generation of AABW from DSW overflow ceases under the RCP8.5 anthropogenic forcing as the shelf water becomes more buoyant. The latter is mostly attributed to a reduction of sea ice formation along the coast. The resulting freshening of DSW results in an increase of the sea surface height (SSH) over the Antarctic shelf, which leads to an increased meridional SSH gradient and a strengthening of the ASC. This positive feedback further isolates the fresher shelf waters, and eventually turns the three characteristic shelf water regimes into “Fresh Shelf” regimes.

6.2 Future works

While my research for this dissertation led to important results and new insights, it reveals that even the HR CESM1.3 simulations cannot represent processes such as the Antarctic shelf dynamics and DSW overflow very well. At the same time, the HR simulations seem to suffer from an overproduction of OOPs in the Weddell Sea region

(especially MRPs) compared to the observational records. These two effects will both lead to large biases in the simulated deep ocean water properties, the simulated sea ice area, and the simulated Antarctic ice sheet melt (if CESM1.3 had an ice sheet). In the future, with anticipated larger computing power, or more efficient numerical methods, the following improvements can hopefully be made:

- (1) A straightforward and efficient way is to include the overflow parameterization in the HR simulations. A more accurate representation of the DSW overflow process will enhance the credibility of future ESM simulations where a realistic representation of the global MOC becomes important.
- (2) Due to the Antarctic shelf region requiring exceptionally high resolution compared to other regions, the numerical method approach toward “mesh refinable global grids” may be another viable choice (e.g., the newly developed Models for Prediction Across Scales (MPAS) in E3SM model; Ringler et al., 2013).
- (3) Continue to increase the ESM resolution, e.g., by increasing the ocean resolution to 0.01° . This requires a huge amount of computing resources (still not available today), but it will deliver some fundamental improvements and new insights: such as the possibility of 1) resolving convective plumes by the governing model equations, instead of relying on convection parameterization schemes (which lead to crude estimates of the mixing process and mixing depth; Sohail et al., 2020); 2) including tides which exert an important effect on the Antarctic shelf circulation (e.g., Padman et al., 2018), and thus the DSW overflow process (Thompson et al., 2018); and

3) to fully resolve the DSW overflow process instead of parameterizing it (Danabasoglu et al., 2010; Legg et al., 2009; Dufour et al., 2017).

(4) Another caveat in these CESM1.3 simulations is that they do not include an ice sheet/shelf model (Lipscomb et al., 2019). Accounting for interactive ice sheet/shelf melt will affect the freshwater flux due to glacial ice melt and thus influence the processes I described in Chapters 3,4, and 5. Furthermore, it is still a scientific challenge to arrive at an accurate prediction of the Antarctic ice sheet development and its contribution to the global mean sea level rise (Edwards et al., 2021). The projected Antarctic contribution to sea level rise does not show a clear response to the RCP8.5 emission scenario, mainly owing to the uncertainties in the competing process of increasing ice loss in West-Antarctica and increasing snowfall and thus ice accumulation in East-Antarctica in a warming climate (Edwards et al., 2021). Interestingly, our HR and LR simulations also show zonally asymmetric response patterns of the sea ice extent around Antarctica, which indicates that the Antarctic region is very sensitive to the ocean model resolution (van Western & Dykstra, 2021). Thus, in future works, a higher resolution CESM model that includes an ice sheet component is likely to deliver much more accurate projections on the anthropogenic impact on such important quantities as the global sea-level rise and the global MOC that both depend on a detailed representation of the complex physical processes along Antarctica addressed in this study.

REFERENCES

- Adusumilli, S., Fricker, H. A., Medley, B., Padman, L., & Siegfried, M. R. (2020). Interannual variations in meltwater input to the Southern Ocean from Antarctic ice shelves. *Nature geoscience*, 13(9), 616-620.
- Akitomo, K. (2006). Thermobaric deep convection, baroclinic instability, and their roles in vertical heat transport around Maud Rise in the Weddell Sea. *Journal of Geophysical Research: Oceans*, 111(C9).
- Baines, P. G., & Fraedrich, K. (1989). Topographic effects on the mean tropospheric flow patterns around Antarctica. *Journal of Atmospheric Sciences*, 46(22), 3401-3415.
- Banerjee, A., Fyfe, J. C., Polvani, L. M., Waugh, D., & Chang, K. L. (2020). A pause in Southern Hemisphere circulation trends due to the Montreal Protocol. *Nature*, 579(7800), 544-548.
- Bromwich, D. H., Nicolas, J. P., & Monaghan, A. J. (2011). An assessment of precipitation changes over Antarctica and the Southern Ocean since 1989 in contemporary global reanalyses. *Journal of Climate*, 24(16), 4189-4209.
- Campbell, E. C., Wilson, E. A., Moore, G. K., Riser, S. C., Brayton, C. E., Mazloff, M. R., & Talley, L. D. (2019). Antarctic offshore polynyas linked to Southern Hemisphere climate anomalies. *Nature*, 570(7761), 319-325.
- Carsey, F. D. (1980). Microwave observation of the Weddell Polynya. *Monthly Weather Review*, 108(12), 2032-2044.
- Chang, P., Zhang, S., Danabasoglu, G., Yeager, S. G., Fu, H., Wang, H., ... & Wu, L. (2020). An unprecedented set of high-resolution earth system simulations for understanding multiscale interactions in climate variability and change. *Journal of Advances in Modeling Earth Systems*, 12(12), e2020MS002298.
- Chavanne, C. P., Heywood, K. J., Nicholls, K. W., & Fer, I. (2010). Observations of the Antarctic slope undercurrent in the southeastern Weddell Sea. *Geophysical Research Letters*, 37(13).
- Cheon, W. G., & Gordon, A. L. (2019). Open-ocean polynyas and deep convection in the Southern Ocean. *Scientific reports*, 9(1), 1-9.
- Cheon, W. G., Cho, C. B., Gordon, A. L., Kim, Y. H., & Park, Y. G. (2018). The role of oscillating Southern Hemisphere westerly winds: Southern Ocean coastal and open-ocean polynyas. *Journal of Climate*, 31(3), 1053-1073.

- Cheon, W. G., Lee, S. K., Gordon, A. L., Liu, Y., Cho, C. B., & Park, J. J. (2015). Replicating the 1970s' Weddell polynya using a coupled ocean-sea ice model with reanalysis surface flux fields. *Geophysical Research Letters*, 42(13), 5411-5418.
- Cheon, W. G., Park, Y. G., Toggweiler, J. R., & Lee, S. K. (2014). The relationship of Weddell Polynya and open-ocean deep convection to the Southern Hemisphere westerlies. *Journal of physical oceanography*, 44(2), 694-713.
- Comiso, J. C., & Gordon, A. L. (1987). Recurring polynyas over the Cosmonaut Sea and the Maud Rise. *Journal of Geophysical Research: Oceans*, 92(C3), 2819-2833.
- Danabasoglu, G., Bates, S. C., Briegleb, B. P., Jayne, S. R., Jochum, M., Large, W. G., ... & Yeager, S. G. (2012). The CCSM4 ocean component. *Journal of Climate*, 25(5), 1361-1389.
- Danabasoglu, G., Large, W. G., & Briegleb, B. P. (2010). Climate impacts of parameterized Nordic Sea overflows. *Journal of Geophysical Research: Oceans*, 115(C11).
- De Lavergne, C., Palter, J. B., Galbraith, E. D., Bernardello, R., & Marinov, I. (2014). Cessation of deep convection in the open Southern Ocean under anthropogenic climate change. *Nature Climate Change*, 4(4), 278-282.
- De Veaux, R. D., Gordon, A. L., Comiso, J. C., & Bacherer, N. E. (1993). Modeling of topographic effects on Antarctic sea-ice using multivariate adaptive regression splines. *Journal of Geophysical Research: Oceans*, 98(C11), 20307-20319.
- Dennis, J. M., Edwards, J., Evans, K. J., Guba, O., Lauritzen, P. H., Mirin, A. A., ... & Worley, P. H. (2012). CAM-SE: A scalable spectral element dynamical core for the Community Atmosphere Model. *The International Journal of High-Performance Computing Applications*, 26(1), 74-89.
- Diao, X., Stössel, A., Chang, P., Danabasoglu, G., Yeager, S. G., Gopal, A., ... & Zhang, S. (2022). On the Intermittent Occurrence of Open-Ocean Polynyas in a Multi-Century High-Resolution Preindustrial Earth System Model Simulation. *Journal of Geophysical Research: Oceans*, e2021JC017672.
- Dong, J., Speer, K., & Jullion, L. (2016). The Antarctic Slope Current near 30° E. *Journal of Geophysical Research: Oceans*, 121(2), 1051-1062.
- Dufour, C. O., Morrison, A. K., Griffies, S. M., Frenger, I., Zanowski, H., & Winton, M. (2017). Preconditioning of the Weddell Sea polynya by the ocean mesoscale and dense water overflows. *Journal of Climate*, 30(19), 7719-7737.

Eayrs, C., Li, X., Raphael, M. N., & Holland, D. M. (2021). Rapid decline in Antarctic sea ice in recent years hints at future change. *Nature Geoscience*, 14(7), 460-464.

Edwards, T. L., Nowicki, S., Marzeion, B., Hock, R., Goelzer, H., Seroussi, H., ... & Zwinger, T. (2021). Projected land ice contributions to twenty-first-century sea level rise. *Nature*, 593(7857), 74-82.

Fox-Kemper, B., Hewitt, H. T., Xiao, C., Aðalgeirsdóttir, G., Drijfhout, S. S., Edwards, T. L., ... & Yu, Y. (2021). Ocean, cryosphere and sea level change. *Climate change 2021: The physical science basis. Contribution of Working Group I to the sixth assessment report of the intergovernmental panel on climate change*.

Francis, D., Mattingly, K. S., Temimi, M., Massom, R., & Heil, P. (2020). On the crucial role of atmospheric rivers in the two major Weddell Polynya events in 1973 and 2017 in Antarctica. *Science advances*, 6(46), eabc2695.

Gent, P. R., & Mcwilliams, J. C. (1990). Isopycnal mixing in ocean circulation models. *Journal of Physical Oceanography*, 20(1), 150-155.

Genthon, C., Krinner, G., & Sacchettini, M. (2003). Interannual Antarctic tropospheric circulation and precipitation variability. *Climate Dynamics*, 21(3), 289-307.

Gillett, N. P., Fyfe, J. C., & Parker, D. E. (2013). Attribution of observed sea level pressure trends to greenhouse gas, aerosol, and ozone changes. *Geophysical Research Letters*, 40(10), 2302-2306.

Gnanadesikan, A., Speller, C. M., Ringlein, G., San Soucie, J., Thomas, J., & Pradal, M. A. (2020). Feedbacks driving interdecadal variability in southern ocean convection in climate models: a coupled oscillator mechanism. *Journal of Physical Oceanography*, 50(8), 2227-2249.

Goodwin, I. D., Van Ommen, T. D., Curran, M. A. J., & Mayewski, P. A. (2004). Mid latitude winter climate variability in the South Indian and southwest Pacific regions since 1300 AD. *Climate Dynamics*, 22(8), 783-794.

Goddard, P. B., Dufour, C. O., Yin, J., Griffies, S. M., & Winton, M. (2017). CO₂-induced Ocean warming of the Antarctic continental shelf in an eddying global climate model. *Journal of Geophysical Research: Oceans*, 122(10), 8079-8101.

Gordon, A. L., & Huber, B. A. (1990). Southern Ocean winter mixed layer. *Journal of Geophysical Research: Oceans*, 95(C7), 11655-11672.

Gordon, A. L., Visbeck, M., & Comiso, J. C. (2007). A possible link between the Weddell Polynya and the Southern Annular Mode. *Journal of Climate*, 20(11), 2558-2571.

Gordon, A. L. (2012). Circumpolar view of the Southern Ocean from 1962 to 1992. *Oceanography*, 25(3), 18-23.

Gordon, A. L. (2014). Southern Ocean polynya. *Nature Climate Change*, 4(4), 249-250.

Granger, C. W. (1969). Investigating causal relations by econometric models and cross-spectral methods. *Econometrica: journal of the Econometric Society*, 424-438.

Gutjahr, O., Putrasahan, D., Lohmann, K., Jungclaus, J. H., von Storch, J. S., Brüggemann, N., ... & Stössel, A. (2019). Max planck institute earth system model (MPI-ESM1. 2) for the high-resolution model intercomparison project (HighResMIP). *Geoscientific Model Development*, 12(7), 3241-3281.

Hallberg, R. (2013). Using a resolution function to regulate parameterizations of oceanic mesoscale eddy effects. *Ocean Modelling*, 72, 92-103.

Hasselmann, K. (1988). PIPs and POPs: The reduction of complex dynamical systems using principal interaction and oscillation patterns. *Journal of Geophysical Research: Atmospheres*, 93(D9), 11015-11021.

Haumann, F. A., Gruber, N., Münnich, M., Frenger, I., & Kern, S. (2016). Sea-ice transport driving Southern Ocean salinity and its recent trends. *Nature*, 537(7618), 89-92. Hunke, E. C., Lipscomb, W. H., Turner, A. K., Jeffery, N., & Elliott, S. (2010). CICE: the los alamos sea ice model documentation and software user's manual version 4.1 la-cc-06-012. T-3 Fluid Dynamics Group, Los Alamos National Laboratory, 675, 500.

Hirabara, M., Tsujino, H., Nakano, H., & Yamanaka, G. (2012). Formation mechanism of the Weddell Sea Polynya and the impact on the global abyssal ocean. *Journal of oceanography*, 68(5), 771-796.

Hunke, E. C., Lipscomb, W. H., Turner, A. K., Jeffery, N., & Elliott, S. (2008). CICE: The Los Alamos Sea ice model, documentation and software user's manual. T-3 Fluid Dynamics Group, Los Alamos National Laboratory, Los Alamos, NM, 87545.

Huot, P. V., Fichefet, T., Jourdain, N. C., Mathiot, P., Rousset, C., Kittel, C., & Fettweis, X. (2021). Influence of ocean tides and ice shelves on ocean–ice interactions and dense shelf water formation in the D'Urville Sea, Antarctica. *Ocean Modelling*, 162, 101794.

Jacobs, S. S. (1991). On the nature and significance of the Antarctic Slope Front. *Marine Chemistry*, 35(1-4), 9-24.

Jacobs, S. S., & Giulivi, C. F. (2010). Large multidecadal salinity trends near the Pacific–Antarctic continental margin. *Journal of Climate*, 23(17), 4508-4524.

Jacobs, S. S., Giulivi, C. F., & Mele, P. A. (2002). Freshening of the Ross Sea during the late 20th century. *science*, 297(5580), 386-389.

Jenkins, A., & Jacobs, S. (2008). Circulation and melting beneath George VI ice shelf, Antarctica. *Journal of Geophysical Research: Oceans*, 113(C4).

Jena, B., Ravichandran, M., & Turner, J. (2019). Recent reoccurrence of large open-ocean polynya on the Maud Rise seamount. *Geophysical Research Letters*, 46(8), 4320-4329.

Jones, J. M., Gille, S. T., Goosse, H., Abram, N. J., Canziani, P. O., Charman, D. J., ... & Vance, T. R. (2016). Assessing recent trends in high-latitude Southern Hemisphere surface climate. *Nature Climate Change*, 6(10), 917-926.

Jüling, A., Viebahn, J. P., Drijfhout, S. S., & Dijkstra, H. A. (2018). Energetics of the southern ocean mode. *Journal of Geophysical Research: Oceans*, 123(12), 9283-9304.

Kaufman, Z. S., Feldl, N., Weijer, W., & Veneziani, M. (2020). Causal interactions between Southern Ocean polynyas and high-latitude atmosphere–ocean variability. *Journal of Climate*, 33(11), 4891-4905.

Kjellsson, J., Holland, P. R., Marshall, G. J., Mathiot, P., Aksenov, Y., Coward, A. C., ... & Ridley, J. (2015). Model sensitivity of the Weddell and Ross seas, Antarctica, to vertical mixing and freshwater forcing. *Ocean Modelling*, 94, 141-152.

Kurtakoti, P., Veneziani, M., Stössel, A., & Weijer, W. (2018). Preconditioning and formation of Maud Rise polynyas in a high-resolution Earth system model. *Journal of Climate*, 31(23), 9659-9678.

Kurtakoti, P., Veneziani, M., Stössel, A., Weijer, W., & Maltrud, M. (2021). On the Generation of Weddell Sea Polynyas in a High-Resolution Earth System Model. *Journal of Climate*, 34(7), 2491-2510.

Lamarque, J. F., Bond, T. C., Eyring, V., Granier, C., Heil, A., Klimont, Z., ... & Van Vuuren, D. P. (2010). Historical (1850–2000) gridded anthropogenic and biomass burning emissions of reactive gases and aerosols: methodology and application. *Atmospheric Chemistry and Physics*, 10(15), 7017-7039.

Large, W. G., Danabasoglu, G., Doney, S. C., & McWilliams, J. C. (1997). Sensitivity to surface forcing and boundary layer mixing in a global ocean model: Annual-mean climatology. *Journal of Physical Oceanography*, 27(11), 2418-2447.

Latif, M., Martin, T., Reintges, A., & Park, W. (2017). Southern Ocean decadal variability and predictability. *Current Climate Change Reports*, 3(3), 163-173.

Lawrence, D. M., Oleson, K. W., Flanner, M. G., Thornton, P. E., Swenson, S. C., Lawrence, P. J., ... & Slater, A. G. (2011). Parameterization improvements and functional and structural advances in version 4 of the Community Land Model. *Journal of Advances in Modeling Earth Systems*, 3(1).

Lindsay, R. W., Holland, D. M., & Woodgate, R. A. (2004). Halo of low ice concentration observed over the Maud Rise seamount. *Geophysical research letters*, 31(13).

Lockwood, J. W., Dufour, C. O., Griffies, S. M., & Winton, M. (2021). On the role of the Antarctic Slope Front on the occurrence of the Weddell Sea polynya under climate change. *Journal of Climate*, 34(7), 2529-2548.

Maraun, D., & Kurths, J. (2004). Cross wavelet analysis: significance testing and pitfalls. *Nonlinear Processes in Geophysics*, 11(4), 505-514.

Maier-Reimer, E., Mikolajewicz, U., & Hasselmann, K. (1993). Mean circulation of the Hamburg LSG OGCM and its sensitivity to the thermohaline surface forcing. *Journal of Physical Oceanography*, 23(4), 731-757.

Marsh, D. R., Mills, M. J., Kinnison, D. E., Lamarque, J. F., Calvo, N., & Polvani, L. M. (2013). Climate change from 1850 to 2005 simulated in CESM1 (WACCM). *Journal of climate*, 26(19), 7372-7391.

Marshall, G. J. (2003). Trends in the Southern Annular Mode from observations and reanalyses. *Journal of climate*, 16(24), 4134-4143.

Marshall, J., & Schott, F. (1999). Open-ocean convection: Observations, theory, and models. *Reviews of geophysics*, 37(1), 1-64.

Martin, T., Park, W., & Latif, M. (2015). Southern Ocean forcing of the North Atlantic at multi-centennial time scales in the Kiel Climate Model. *Deep Sea Research Part II: Topical Studies in Oceanography*, 114, 39-48.

Martin, T., Park, W., & Latif, M. (2013). Multi-centennial variability controlled by Southern Ocean convection in the Kiel Climate Model. *Climate dynamics*, 40(7), 2005-2022.

Martinson, D. G., Killworth, P. D., & Gordon, A. L. (1981). A convective model for the Weddell Polynya. *Journal of Physical Oceanography*, 11(4), 466-488.

Meehl, G. A., Yang, D., Arblaster, J. M., Bates, S. C., Rosenbloom, N., Neale, R., ... & Danabasoglu, G. (2019). Effects of model resolution, physics, and coupling on Southern Hemisphere storm tracks in CESM1. 3. *Geophysical Research Letters*, 46(21), 12408-12416.

Meinshausen, M., Smith, S. J., Calvin, K., Daniel, J. S., Kainuma, M. L., Lamarque, J. F., ... & Van Vuuren, D. P. P. (2011). The RCP greenhouse gas concentrations and their extensions from 1765 to 2300. *Climatic change*, 109(1), 213-241.

Menezes, V. V., Macdonald, A. M., & Schatzman, C. (2017). Accelerated freshening of Antarctic Bottom Water over the last decade in the Southern Indian Ocean. *Science advances*, 3(1), e1601426.

Montade, V., Peyron, O., Favier, C., Francois, J. P., & Haberle, S. G. (2019). A pollen-climate calibration from western Patagonia for palaeoclimatic reconstructions. *Journal of Quaternary Science*, 34(1), 76-86.

Moorman, R., Morrison, A. K., & McC. Hogg, A. (2020). Thermal responses to Antarctic ice shelf melt in an eddy-rich global ocean-sea ice model. *Journal of Climate*, 33(15), 6599-6620.

Morales Maqueda, M. A., Willmott, A. J., & Biggs, N. R. T. (2004). Polynya dynamics: A review of observations and modeling. *Reviews of Geophysics*, 42(1).

Neale, R. B., Chen, C. C., Gettelman, A., Lauritzen, P. H., Park, S., Williamson, D. L., ... & Taylor, M. A. (2010). Description of the NCAR community atmosphere model (CAM 5.0). NCAR Tech. Note NCAR/TN-486+ STR, 1(1), 1-12.

Nicholls, K. W., Østerhus, S., Makinson, K., Gammelsrød, T., & Fahrbach, E. (2009). Ice-ocean processes over the continental shelf of the southern Weddell Sea, Antarctica: A review. *Reviews of Geophysics*, 47(3).

Ohshima, K. I., Fukamachi, Y., Williams, G. D., Nihashi, S., Roquet, F., Kitade, Y., ... & Wakatsuchi, M. (2013). Antarctic Bottom Water production by intense sea-ice formation in the Cape Darnley polynya. *Nature Geoscience*, 6(3), 235-240.

Orsi, A. H. (1993). NOWLIN JR. WD; WHITWORTH III, T. On the circulation and stratification of the Weddell Gyre. *Deep-Sea Res. I*, 40, 169-203.

Orsi, A. H., & Whitworth, T. (2005). Hydrographic Atlas of the World Ocean Circulation Experiment (WOCE): Volume 1: Southern Ocean. Southampton, UK: WOCE International Project Office.

Orsi, A. H., Johnson, G. C., & Bullister, J. L. (1999). Circulation, mixing, and production of Antarctic Bottom Water. *Progress in Oceanography*, 43(1), 55-109.

Orsi, A. H., Smethie Jr, W. M., & Bullister, J. L. (2002). On the total input of Antarctic waters to the deep ocean: A preliminary estimate from chlorofluorocarbon measurements. *Journal of Geophysical Research: Oceans*, 107(C8), 31-1.

Parkinson, C. L., & Cavalieri, D. J. (2012). Antarctic sea ice variability and trends, 1979–2010. *The Cryosphere*, 6(4), 871-880.

Paolo, F. S., Padman, L., Fricker, H. A., Adusumilli, S., Howard, S., & Siegfried, M. R. (2018). Response of Pacific-sector Antarctic ice shelves to the El Niño/Southern oscillation. *Nature geoscience*, 11(2), 121-126.

Patara, L., & Böning, C. W. (2014). Abyssal ocean warming around Antarctica strengthens the Atlantic overturning circulation. *Geophysical Research Letters*, 41(11), 3972-3978.

Pettit, E. C., Wild, C., Alley, K., Muto, A., Truffer, M., Bevan, S. L., ... & Benn, D. (2021, December). Collapse of Thwaites Eastern Ice Shelf by intersecting fractures. In AGU Fall Meeting 2021. AGU.

Price, J. F., & Yang, J. (1998). Marginal sea overflows for climate simulations. In *Ocean Modeling and Parameterization* (pp. 155-170). Springer, Dordrecht.

Pritchard, H., Ligtenberg, S. R., Fricker, H. A., Vaughan, D. G., van den Broeke, M. R., & Padman, L. (2012). Antarctic ice-sheet loss driven by basal melting of ice shelves. *Nature*, 484(7395), 502-505.

Raphael, M. N., Marshall, G. J., Turner, J., Fogt, R. L., Schneider, D., Dixon, D. A., ... & Hobbs, W. R. (2016). The Amundsen Sea low: Variability, change, and impact on Antarctic climate. *Bulletin of the American Meteorological Society*, 97(1), 111-121.

Silvano, A., Foppert, A., Rintoul, S. R., Holland, P. R., Tamura, T., Kimura, N., ... & Macdonald, A. M. (2020). Recent recovery of Antarctic Bottom Water formation in the Ross Sea driven by climate anomalies. *Nature Geoscience*, 13(12), 780-786.

Silvano, A., Rintoul, S. R., Peña-Molino, B., Hobbs, W. R., van Wijk, E., Aoki, S., ... & Williams, G. D. (2018). Freshening by glacial meltwater enhances melting of ice shelves and reduces formation of Antarctic Bottom Water. *Science advances*, 4(4), eaap9467.

Small, R. J., Bacmeister, J., Bailey, D., Baker, A., Bishop, S., Bryan, F., ... & Vertenstein, M. (2014). A new synoptic scale resolving global climate simulation using the Community Earth System Model. *Journal of Advances in Modeling Earth Systems*, 6(4), 1065-1094.

Smith, R., Jones, P., Briegleb, B., Bryan, F., Danabasoglu, G., Dennis, J., ... & Yeager, S. (2010). The parallel ocean program (POP) reference manual ocean component of the

community climate system model (CCSM) and community earth system model (CESM). LAUR-01853, 141, 1-140.

Snow, K., Hogg, A. M., Sloyan, B. M., & Downes, S. M. (2016). Sensitivity of Antarctic Bottom Water to changes in surface buoyancy fluxes. *Journal of Climate*, 29(1), 313-330.

Sohail, T., Gayen, B., & Hogg, A. M. (2020). The dynamics of mixed layer deepening during open-ocean convection. *Journal of Physical Oceanography*, 50(6), 1625-1641.

Stössel, A., Notz, D., Haumann, F. A., Haak, H., Jungclaus, J., & Mikolajewicz, U. (2015). Controlling high-latitude Southern Ocean convection in climate models. *Ocean Modelling*, 86, 58-75.

Stössel, A., & Kim, S. J. (2001). Decadal deep-water variability in the subtropical Atlantic and convection in the Weddell Sea. *Journal of Geophysical Research: Oceans*, 106(C10), 22425-22440.

Spensberger, C., Reeder, M. J., Spengler, T., & Patterson, M. (2020). The connection between the southern annular mode and a feature-based perspective on Southern Hemisphere midlatitude winter variability. *Journal of Climate*, 33(1), 115-129.

Stewart, A. L., & Thompson, A. F. (2015). Eddy-mediated transport of warm Circumpolar Deep Water across the Antarctic shelf break. *Geophysical Research Letters*, 42(2), 432-440.

Swart, N. C., & Fyfe, J. C. (2012). Observed and simulated changes in the Southern Hemisphere surface westerly wind-stress. *Geophysical Research Letters*, 39(16).

Tamura, T., Ohshima, K. I., Fraser, A. D., & Williams, G. D. (2016). Sea ice production variability in Antarctic coastal polynyas. *Journal of Geophysical Research: Oceans*, 121(5), 2967-2979.

Thompson, D. W., & Solomon, S. (2002). Interpretation of recent Southern Hemisphere climate change. *Science*, 296(5569), 895-899.

Thompson, D. W., & Wallace, J. M. (2000). Annular modes in the extratropical circulation. Part I: Month-to-month variability. *Journal of climate*, 13(5), 1000-1016.

Thompson, A. F., Stewart, A. L., Spence, P., & Heywood, K. J. (2018). The Antarctic Slope Current in a changing climate. *Reviews of Geophysics*, 56(4), 741-770.

Toggweiler, J. R., & Russell, J. (2008). Ocean circulation in a warming climate. *Nature*, 451(7176), 286-288.

Torrence, C., & Compo, G. P. (1998). A practical guide to wavelet analysis. *Bulletin of the American Meteorological society*, 79(1), 61-78.

Turner, J., Comiso, J. C., Marshall, G. J., Lachlan-Cope, T. A., Bracegirdle, T., Maksym, T., ... & Orr, A. (2009). Non-annular atmospheric circulation change induced by stratospheric ozone depletion and its role in the recent increase of Antarctic sea-ice extent. *Geophysical research letters*, 36(8).

van Westen, R. M., & Dijkstra, H. A. (2020). Multidecadal preconditioning of the Maud Rise polynya region. *Ocean Science*, 16(6), 1443-1457.

van Westen, R. M., & Dijkstra, H. A. (2021). Ocean eddies strongly affect global mean sea-level projections. *Science advances*, 7(15), eabf1674.

Vreugdenhil, C. A., & Gayen, B. (2021). Ocean Convection. *Fluids*, 6(10), 360.

Weijer, W., Veneziani, M., Stössel, A., Hecht, M. W., Jeffery, N., Jonko, A., ... & Wang, H. (2017). Local atmospheric response to an open-ocean polynya in a high-resolution climate model. *Journal of Climate*, 30(5), 1629-1641.

Whitworth III, T., Orsi, A. H., Kim, S. J., Nowlin Jr, W. D., & Locarnini, R. A. (1985). Water masses and mixing near the Antarctic Slope Front. *Ocean, ice, and atmosphere: interactions at the Antarctic continental margin*, 75, 1-27.

Whitworth, T., & Orsi, A. H. (2006). Antarctic Bottom Water production and export by tides in the Ross Sea. *Geophysical Research Letters*, 33(12).

Williams, G. D., Aoki, S., Jacobs, S. S., Rintoul, S. R., Tamura, T., & Bindoff, N. L. (2010). Antarctic bottom water from the Adélie and George V Land coast, East Antarctica (140–149 E). *Journal of Geophysical Research: Oceans*, 115(C4).

Yuan, N., Ding, M., Ludescher, J., & Bunde, A. (2017). Increase of the Antarctic Sea Ice Extent is highly significant only in the Ross Sea. *Scientific reports*, 7(1), 1-8.

Zanowski, H., & Hallberg, R. (2017). Weddell Polynya transport mechanisms in the abyssal ocean. *Journal of Physical Oceanography*, 47(12), 2907-2925.

Zhang, L., Delworth, T. L., Cooke, W., Goosse, H., Bushuk, M., Morioka, Y., & Yang, X. (2021). The dependence of internal multidecadal variability in the Southern Ocean on the ocean background mean state. *Journal of Climate*, 34(3), 1061-1080.

Zwally, H. J. (1983). Antarctic sea ice, 1973-1976: Satellite passive-microwave observations (Vol. 459). Scientific and Technical Information Branch, National Aeronautics and Space Administration.

